

Award Number:

W81XWH-06-1-0149

TITLE:

Vatuximab<sup>TM</sup>: Optimizing Therapeutic Strategies for Prostate Cancer Based on Dynamic MR Tumor Oximetry

PRINCIPAL INVESTIGATOR:

Ralph P. Mason, Ph.D., CSci, CChem

CONTRACTING ORGANIZATION:

The University of Texas Southwestern Medical Center at Dallas

Dallas, TX 75390-9058

REPORT DATE:

January 2010

TYPE OF REPORT:

Final

PREPARED FOR: U.S. Army Medical Research and Materiel Command  
Fort Detrick, Maryland 21702-5012

DISTRIBUTION STATEMENT:

X Approved for public release; distribution unlimited

The views, opinions and/or findings contained in this report are those of the author(s) and should not be construed as an official Department of the Army position, policy or decision unless so designated by other documentation.

# REPORT DOCUMENTATION PAGE

Form Approved  
OMB No. 0704-0188

Public reporting burden for this collection of information is estimated to average 1 hour per response, including the time for reviewing instructions, searching existing data sources, gathering and maintaining the data needed, and completing and reviewing this collection of information. Send comments regarding this burden estimate or any other aspect of this collection of information, including suggestions for reducing this burden to Department of Defense, Washington Headquarters Services, Directorate for Information Operations and Reports (0704-0188), 1215 Jefferson Davis Highway, Suite 1204, Arlington, VA 22202-4302. Respondents should be aware that notwithstanding any other provision of law, no person shall be subject to any penalty for failing to comply with a collection of information if it does not display a currently valid OMB control number. **PLEASE DO NOT RETURN YOUR FORM TO THE ABOVE ADDRESS.**

<b>1. REPORT DATE (DD-MM-YYYY)</b> 01-01-2010		<b>2. REPORT TYPE</b> Final		<b>3. DATES COVERED (From - To)</b> 15 Nov 2005 - 31 Dec 2009	
<b>4. TITLE AND SUBTITLE</b> Vatuximab <sup>TM</sup> : Optimizing Therapeutic Strategies for Prostate Cancer Based on Dynamic MR Tumor Oximetry				<b>5a. CONTRACT NUMBER</b>	
				<b>5b. GRANT NUMBER</b> W81XWH-06-1-0149	
				<b>5c. PROGRAM ELEMENT NUMBER</b>	
<b>6. AUTHOR(S)</b> Ralph P. Mason, Ph.D., CSci, CChem				<b>5d. PROJECT NUMBER</b>	
				<b>5e. TASK NUMBER</b>	
				<b>5f. WORK UNIT NUMBER</b>	
<b>7. PERFORMING ORGANIZATION NAME(S) AND ADDRESS(ES)</b> The University of Texas Southwestern Medical Center at Dallas  Dallas, TX 75390-9058				<b>8. PERFORMING ORGANIZATION REPORT NUMBER</b>	
<b>9. SPONSORING / MONITORING AGENCY NAME(S) AND ADDRESS(ES)</b> U.S. Army Medical Research and Materiel Command Fort Detrick, MD 21702-5012				<b>10. SPONSOR/MONITOR'S ACRONYM(S)</b>	
				<b>11. SPONSOR/MONITOR'S REPORT NUMBER(S)</b>	
<b>12. DISTRIBUTION / AVAILABILITY STATEMENT</b>  Approved for public release; distribution unlimited					
<b>13. SUPPLEMENTARY NOTES</b>					
<b>14. ABSTRACT</b> We investigated a novel therapy for prostate cancer using bavituximab, which targets phosphatidylserine expressed on tumor vasculature. Normally, phosphatidylserine exclusively resides on the cytosolic leaflet of the plasma membrane, however, in tumors phosphatidylserine becomes externalized providing a target. It was reported that bavituximab not only targets various tumors, but also induces vascular damage and tumor regression with minimal accompanying toxicity. We found that bavituximab caused little acute pathophysiological response in prostate tumors. Its effect is more subtle than classic vascular disrupting agents. However, in combination with docetaxel there was significantly enhanced tumor growth delay, notably in an intra osseous model of metastatic prostate cancer. Bavituximab is being developed by Peregrine Pharmaceuticals for clinical trials.  Investigations of tumor hypoxia indicated that non-invasive oxygen sensitive <sup>1</sup> H MRI (BOLD and TOLD) reveal hypoxic versus well oxygenated or oxygenatable tumors. DOCENT (Dynamic Oxygen Challenge Evaluated by NMR T <sub>1</sub> and T <sub>2</sub> *) promises a new approach to characterizing tumors <i>in situ</i> . This could provide a practical approach for stratifying patients for hypoxia sensitive therapy. Since hypoxic tumors are reported to be more aggressive, an assessment of prostate cancer hypoxic may help stratify patients for watchful waiting versus aggressive therapy.					
<b>15. SUBJECT TERMS</b> Vascular targeting; MRI; bioluminescent imaging					
<b>16. SECURITY CLASSIFICATION OF:</b>			<b>17. LIMITATION OF ABSTRACT</b>  UU	<b>18. NUMBER OF PAGES</b>  61	<b>19a. NAME OF RESPONSIBLE PERSON</b> USAMRMC
<b>a. REPORT</b> U	<b>b. ABSTRACT</b> U	<b>c. THIS PAGE</b> U			<b>19b. TELEPHONE NUMBER (include area code)</b>

## Table of Contents

	<u>Page</u>
<b>Introduction.....</b>	<b>4</b>
<b>Body.....</b>	<b>5</b>
<b>Key Research Accomplishments.....</b>	<b>22</b>
<b>Reportable Outcomes.....</b>	<b>23</b>
<b>Conclusion.....</b>	<b>25</b>
<b>References.....</b>	<b>26</b>
<b>Appendices.....</b>	<b>28</b>

## Introduction

Targeting tumor vasculature promises new effective therapy for prostate cancer (1, 2). It avoids issues of drug delivery and is potentiated by massive downstream effects where one blood vessel may supply the nutrients for thousands of tumor cells. Thus, disrupting the vascular supply should generate magnified tumor cell kill. This research combines the expertise of three laboratories (Pharmacology, Urology, and Radiology) to investigate and optimize a novel therapeutic approach to prostate cancer. Thorpe *et al.* pioneered the concept of targeting tumor vasculature for therapeutic gain using antibodies (3). Recently, they generated a novel antibody 3G4, which targets phosphatidylserine (PS) expressed on tumor vasculature. 3G4 is a naked antibody, which recruits host defense cells to attack tumor vasculature (4-6). In collaboration with Peregrine Pharmaceuticals, this agent has been chimerized and is being tested in clinical trials as Bavituximab (it should be noted that until recently the name Vatumixab<sup>TM</sup> or Tarvacin had been proposed) (7). Normally, PS exclusively resides on the cytosolic leaflet of the plasma membrane. However, in tumors PS becomes externalized and provides a viable target. The agent not only targets various tumors, but also induces vascular damage and tumor regression with minimal accompanying toxicity. In developing any new therapy, critical issues include scheduling, optimal combination with other interventions to achieve synergy and early assessment of efficacy. Magnetic resonance imaging was used to follow the induction and development of tumor vascular damage *in vivo* providing new insight into spatial and temporal activity and facilitating effective combination with the hypoxic cell selective cytotoxin tirapazamine.

This research program examined the ability of Bavituximab to generate damage in tumor vasculature and induce prostate tumor growth delay. MRI was used to assess the onset and distribution of tumor vascular damage in a series of Dunning prostate rat tumors (R3327- AT1, MAT-Lu, HI, and H) (8-14). This provided an indication of the efficacy with respect to tumors exhibiting diverse histologies (anaplastic to well differentiated), a range of volume doubling times (1.5 to 20 days). Importantly, all these tumors are subclones of the original R3327-H tumor, and hence, together they represent a strong analogy for the clinical situation of advanced multi focal multi clonal prostate cancer. We assessed tumor response at different sizes and the value of repeated doses. Ultimately, we investigated the synergistic application of Bavituximab with additional drugs including the hypoxia selective cell cytotoxin, tirapazamine (15-17) and popular chemotherapeutic docetaxel (18-20). The experience in diverse subcutaneous models was translated to human tumor xenografts in intraosseous models of advanced metastatic prostate cancer (21). Here, PSA levels and/or bioluminescence provided primary indications of tumor growth.

We have achieved further evidence for the therapeutic efficacy of bavituximab in treating prostate cancer. Unlike many drugs there is no apparent toxicity, but long term efficacy was observed. It was particularly effective at treating human PC3 xenografts implanted in the femur of mice as a model of bone metastasis. We also observed some efficacy in larger rat tumors, particularly when combined with docetaxel. While bavituximab targets the vasculature pathophysiological response in terms of tumor perfusion, cellularity and oxygenation were quite subtle. The results lay further foundation justifying future clinical trials and indeed further research is funded by the CDMRP prostate cancer initiative. The research also provides new insight into development of non-invasive assessment of tumor pathophysiology which is also been pursued under independent funding. Ultimately, these approaches could lead not only to increased survival time with quality of life, but also cure of the prostate cancer patient.

## Body and Progress

**Phase 1 - Evaluate efficacy of Bavituximab to control diverse syngeneic rat prostate tumors: assess physiological parameters (e.g., pO<sub>2</sub>) as surrogate markers of prostate tumor control and mechanisms of response.**

### **Task 1: Months 1-3**

Implant tumors of the four Dunning prostate sublines R3327- MAT-Lu, AT1, HI, and H in Copenhagen rats.

Completed Year 1. Maintaining tumor lines and ensuring integrity of continuity of models is crucial to effective research.

### **Task 2: Months 2-15**

Measure baseline pO<sub>2</sub> (FREDOM), perfusion characteristics (DCE MRI), and ADC (Apparent diffusion coefficient) of tumors and changes with respect to Bavituximab infusion to assess acute response over two hours.

Completed: manuscripts in preparation. pO<sub>2</sub>, DCE and ADC generally showed little response to administration of bavituximab, though there were differences between the tumor sublines. In an effort to enhance the utility of physiological imaging we are exploring less invasive methods and have found potential surrogates for <sup>19</sup>F MRI of oxygen tension (see figures 12 and 13 versus 1 and 2, below). <sup>19</sup>F MRI provides maps of absolute pO<sub>2</sub> and reveals dynamic changes in oxygenation with both spatial and temporal resolution. However, it does require direct injection of the reporter molecule hexafluorobenzene. We have evaluated whether non-invasive methods can provide surrogate estimates of tumor oxygenation, specifically based on BOLD (blood oxygen level dependant) and TOLD (tissue oxygen level dependent) contrast MRI. BOLD is sensitive to changes in vascular oxygenation, since deoxyhemoglobin is paramagnetic causing T<sub>2</sub>\* sensitive signal loss, and thus, should reveal differential vascular oxygen delivery to a tumor (22-31). However, BOLD is also sensitive to vascular volume (dilation and constriction and flow). Meanwhile, TOLD is sensitive to oxygen (O<sub>2</sub>) itself, which is paramagnetic (32, 33). We are investigating the combined use of BOLD and TOLD in prostate tumors as a surrogate for FREDOM. Specifically, BOLD should occur first revealing delivery of oxygen in the capillary network followed by enhanced oxygen tension. We suggest the acronym DOCENT (Dynamic Oxygen Challenge Evaluated by NMR T<sub>1</sub> and T<sub>2</sub>\*). This DOD grant provided proof of principle by comparing separate cohorts of tumor-bearing rats for each test. We are now funded (NCI R01 CA139043-01A1: 2010-2014) to develop the method further in individual tumors in order to rigorously evaluate interpretation of BOLD, TOLD and DCE <sup>1</sup>H MRI as surrogates for absolute pO<sub>2</sub> measurements using <sup>19</sup>F MRI oximetry (FREDOM).

### **Tumor oximetry**

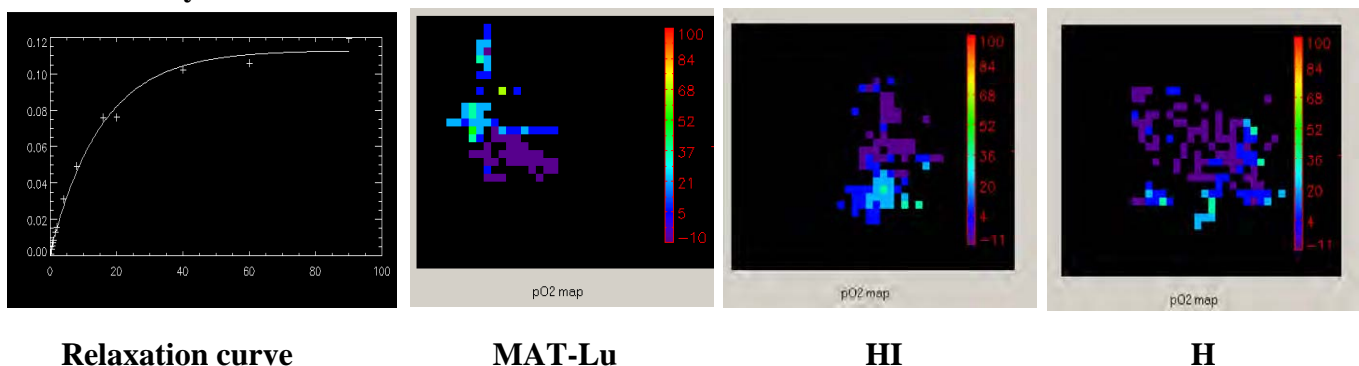


**Figure 1. Oximetry in Dunning prostate tumors.** Left A typical <sup>19</sup>F NMR T<sub>1</sub> relaxation curve for the signal intensity of the reporter molecule hexafluorobenzene from a single voxel within a tumor. The relaxation rate is directly proportional to pO<sub>2</sub>. Based on such curves, maps were generated for representative MAT-Lu, HI and H tumors growing on anesthetized rats breathing air with isoflurane anesthesia. Voxel dimension 1.25 mm in plane with 10 mm thickness.

FREDOM (Fluorocarbon Relaxometry using Echo Planar imaging for Dynamic Oxygen Mapping) (34) was successfully applied to measure tumor  $pO_2$  and dynamic response to interventions. Under baseline air breathing conditions all tumors showed quite similar oxygenation patterns typically ranging from regions of hypoxia to others with  $pO_2 \sim 40$  torr (Figure 1). Comparison of  $pO_2$  values using ANOVA (Analysis of Variance) with Fisher's post hoc test showed that the H tumors had significantly lower  $pO_2$  than the AT1 or HI tumors (Table 1). Following bavituximab administration MAT-Lu, AT1 and H tumors showed no particular change. However, several HI tumors showed hypoxiation over about 1 h. One week later both HI and H tumors showed elevated  $pO_2$  (Figure 2).

	Count	Mean $pO_2$ torr	Std. Dev.	Std. Err.		Mean Diff.	Crit. Diff	P-Value	
AT1	15	10.459	9.635	2.488	AT1, H	8.708	6.404	.0065	S
H	12	1.751	2.810	.753	AT1, HI	2.226	5.442	.4770	
HI	24	8.233	9.258	1.890	AT1, MAT-LU	5.176	5.761	.0764	
MAT-LU	18	5.283	8.079	1.904	H, HI	-6.482	5.846	.0303	S
					H, MAT-LU	-3.533	6.162	.2565	
					HI, MAT-LU	2.950	5.156	.2574	

**Table 1. Baseline oxygenation of four Dunning prostate R3327-tumor lines.**

ANOVA showed that H tumors had significantly lower  $pO_2$  than AT1 or HI. This is contrary to our previous observations and we are examining histology and repeating tests to further clarify the  $pO_2$  values observed in the H tumors.

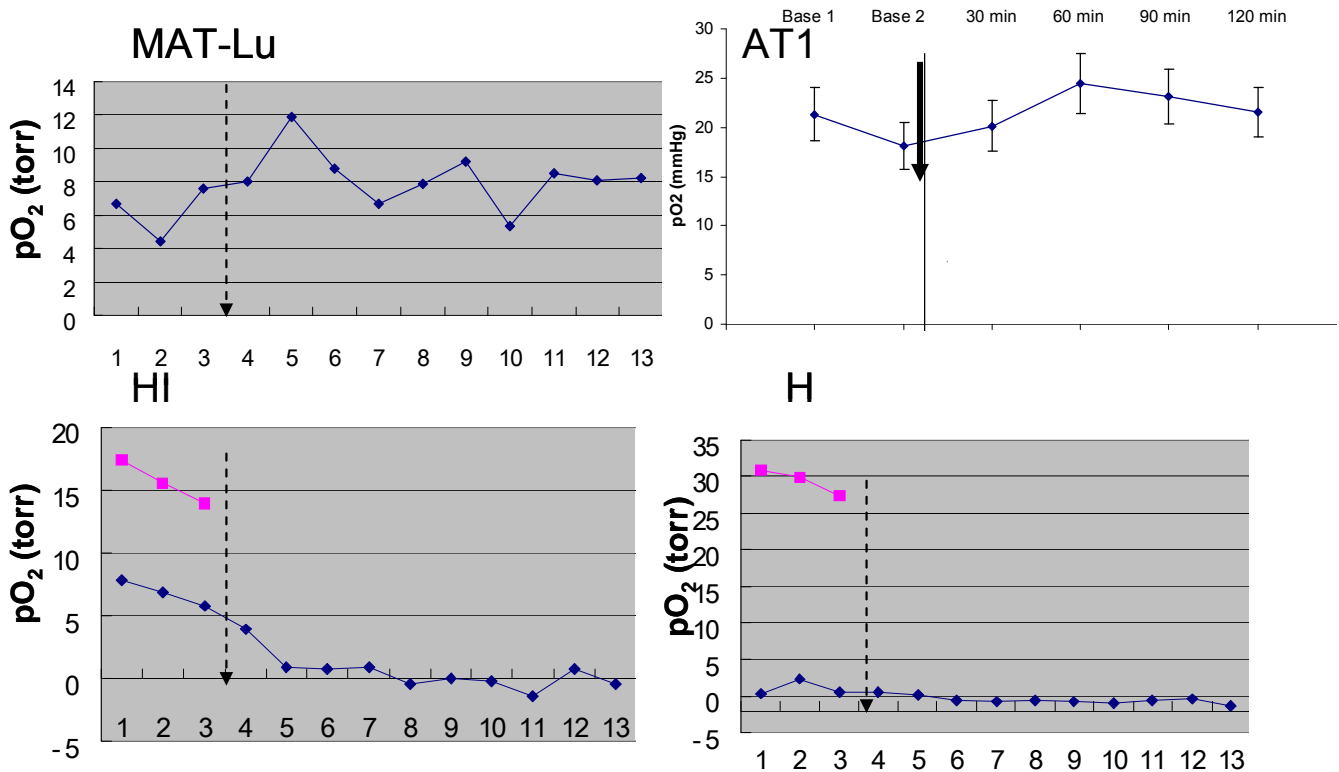


**Figure 2. Oxygen dynamic in Dunning prostate R3327 tumors with respect to bavituximab infusion.**

Two or three baseline  $pO_2$  maps were generated in individual tumors and then bavituximab was infused IP (arrow). Further  $pO_2$  maps were generated over the following 2 hours. Only HI tumors showed significant change (hypoxiation) following infusion. Pink lines show  $pO_2$  measurements seven days later. For HI tumors the decline in  $pO_2$  was significant within 30 mins.

**Dynamic contrast enhanced MRI**

DCE was performed using <sup>1</sup>H MRI at 4.7 T with the small paramagnetic contrast agent Omniscan (0.1 umol /kg (~250 ul) infused IV in tail using catheter vein by hand rapidly (~ 1 s). Data were examined in terms of ΔSI (max change in signal intensity). There was distinct heterogeneity between center and periphery of each tumor type as shown in Figures 3-8 and Tables 2 and 3. In some cases we have compared regional differences and undertaken measurements of the exchange function K<sub>ep</sub>.

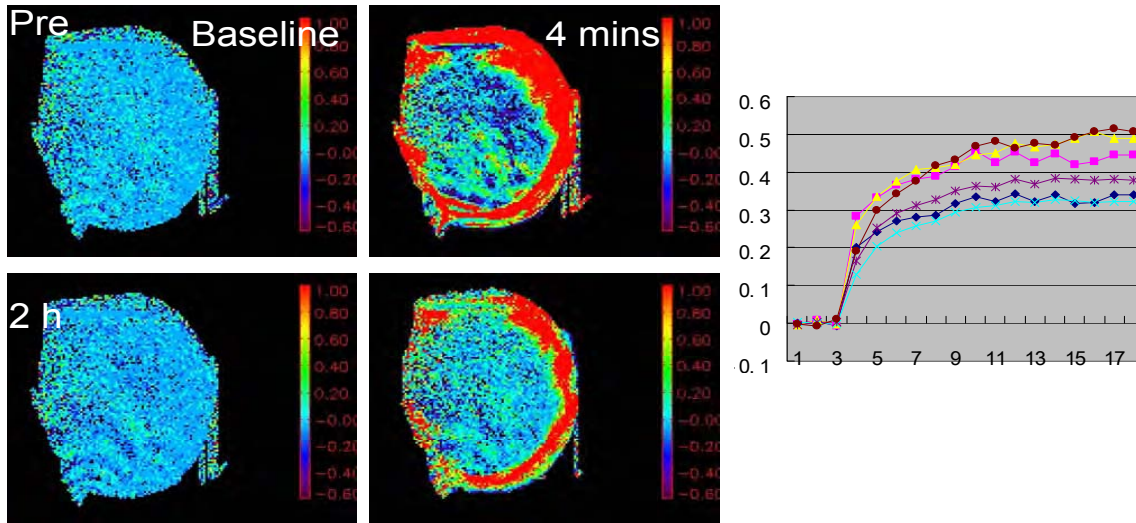
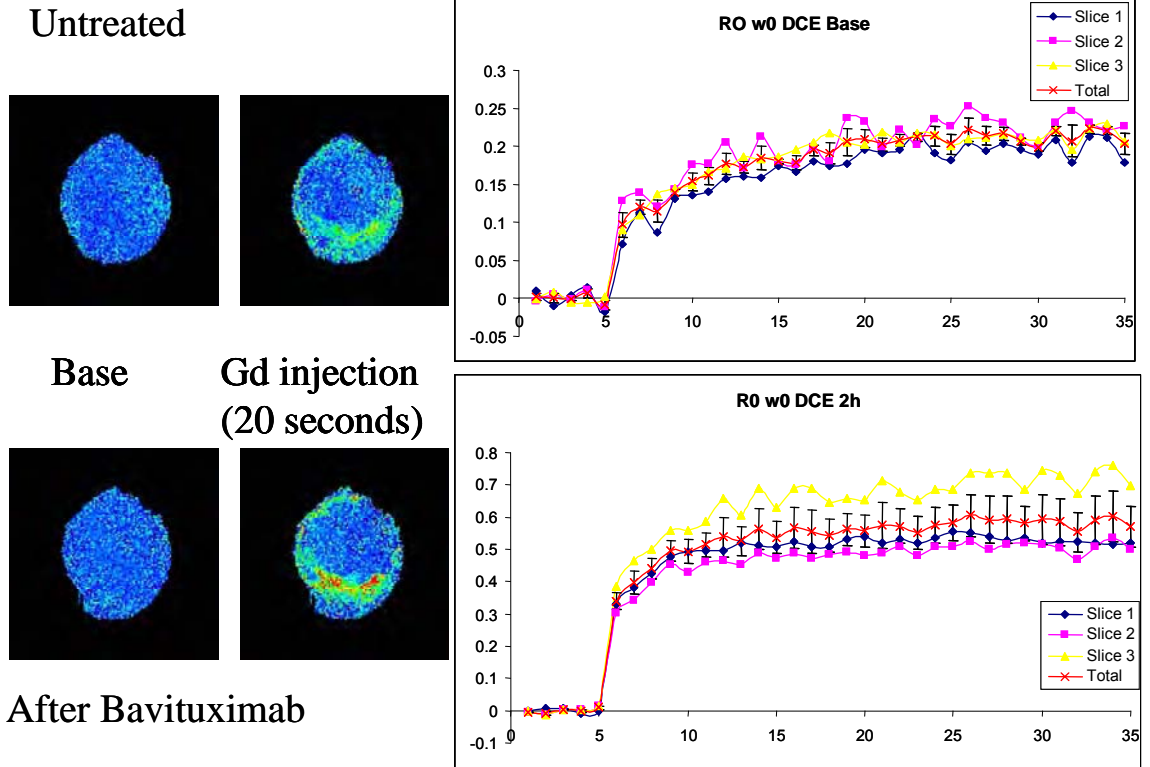


**Figure 3. DCE for MAT-Lu tumor.** Top left Relative signal intensity map for T<sub>1</sub>-weighted MRI pre therapy and before contrast agent. Top center: 4 mins after contrast showing strong peripheral enhancement; Bottom left baseline

MRI 2 h after administration of bavituximab; Bottom center 4 mins post contrast, 2 h after bavituximab. Right curves show mean signal enhancement for three representative image slices before and 2 h after bavituximab. There were no significant changes.

**Figure 4. DCE for AT1 tumor.**

Top left Relative signal intensity map for T<sub>1</sub>-weighted MRI pre therapy and before contrast agent. Top center: 20 s after contrast showing strong peripheral enhancement; Bottom left baseline MRI 2 h after administration of bavituximab; Bottom center 20 s post contrast, 2 h after bavituximab. Right curves show mean signal enhancement for three representative image slices before (top) and 2 h after (bottom) bavituximab.



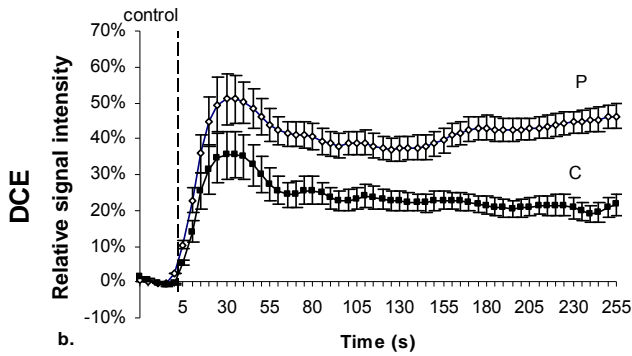


**Figure 5. Comparison of signal intensity during DCE experiments for a group of AT1 tumors.** A significant difference in signal response was observed between central and peripheral regions of tumor.

	Mean	36±1
( $\Delta SI$ ) DCE	Periphery	43±1*
%response	Center	24±1
$K_{ep}$ ( $\text{min}^{-1}$ )	Mean	3.05±0.37
	Periphery	3.11±0.44
	Center	2.59±0.51

**Table 2. Comparison of DCE parameters.** The group of AT1 tumors showed significant difference in signal response to infusion of contrast agent between central and peripheral regions of tumor (\*). No differences were observed for  $K_{ep}$

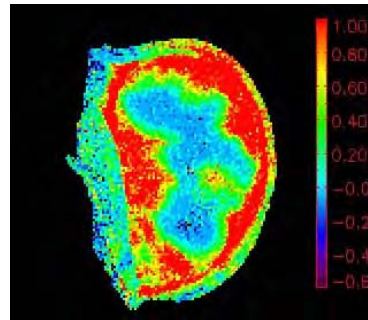
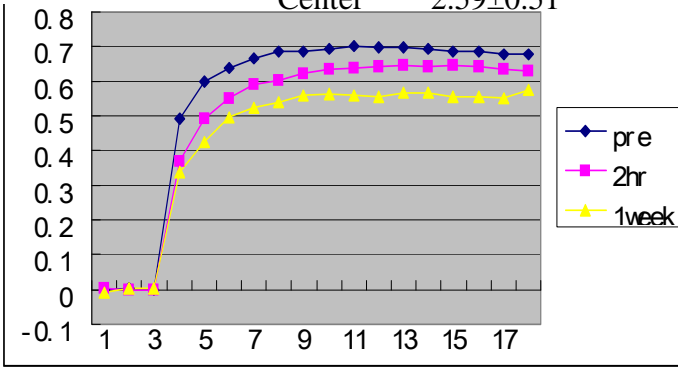


**Figure 6. DCE for HI tumor.** Left Mean signal intensity kinetics following infusion of contrast agent. Right: Relative signal intensity map for  $T_1$ -weighted MRI 2 h post therapy (4 mins after contrast agent) showing heterogeneous perfusion.

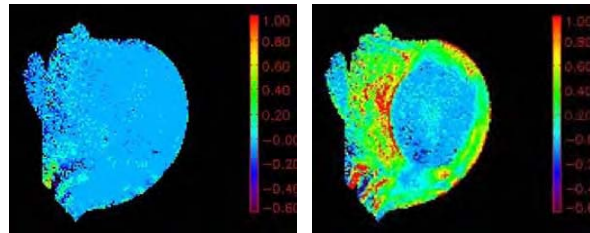
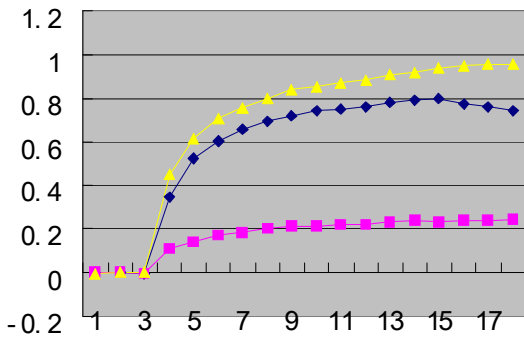


**Figure 7. DCE for H tumor.** Left Mean signal intensity kinetics following infusion of contrast agent. Pre (blue), 2 hrs post bavituximab (pink), 7 days post (yellow). On most occasions, DCE indicated considerably lower signal response in the H tumors 2 h after bavituximab. To verify this result we will both use histology following administration of Hoechst perfusion dye and ensure that future studies include normal tissue allowing assessment of arterial input function. This is crucial to verify that the contrast agent injections are all similarly successful. Right: Relative signal intensity map for  $T_1$ -weighted MRI pre and 4 minutes after contrast agent showing heterogeneous perfusion pre bavituximab.

$(\Delta SI)_{DCE^+}$ %response	Mean $55 \pm 2$	‡
	Periphery $31 \pm 1$	
	Center $124 \pm$	$6^{*‡}$
$K_{ep}$ ( $\text{min}^{-1}$ )	Mean $3.20 \pm$	0.39
	Periphery $3.34 \pm$	0.46
	Center $2.95 \pm$	0.54

**Table 3. Comparison of DCE parameters.** For a group of H tumors there was a significant difference in signal response between central and peripheral regions of tumor (‡). No differences were observed for  $K_{ep}$ .

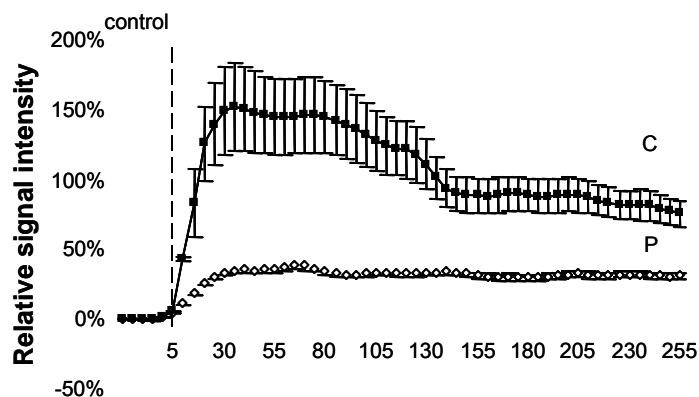


**Figure 8. Comparison of signal intensity during DCE experiments for a group of H tumors.** A significant difference in signal response was observed between central and peripheral regions of tumor, but here the center showed a larger change, whereas for AT1 tumors in Figure 9, the opposite was observed.

While comparison of tumor heterogeneity, *e.g.*, center versus periphery are legitimate, we are concerned that comparison between tumors can be compromised by differential input functions (rate of infusion) and thus our current and future studies will include a reference tissue, as proposed by Yankeelov *et al* (35).

**Apparent diffusion coefficient (ADC)** maps are shown for thin slices from representative Dunning prostate tumors of each subline in Figures 9 and 10. Each tumor shows some heterogeneity. In Figure 10 color representations are provided for a representative AT1 tumor, with 3 selected slices before and two hours after administration of Baviximab. Table 4 provides mean values and compares the statistical significance of difference between the sublines. While the maps showed no significant differences between the AT1 and MAT-Lu tumor types, all the other comparisons revealed significant differences and the H showed much lower ADC values.

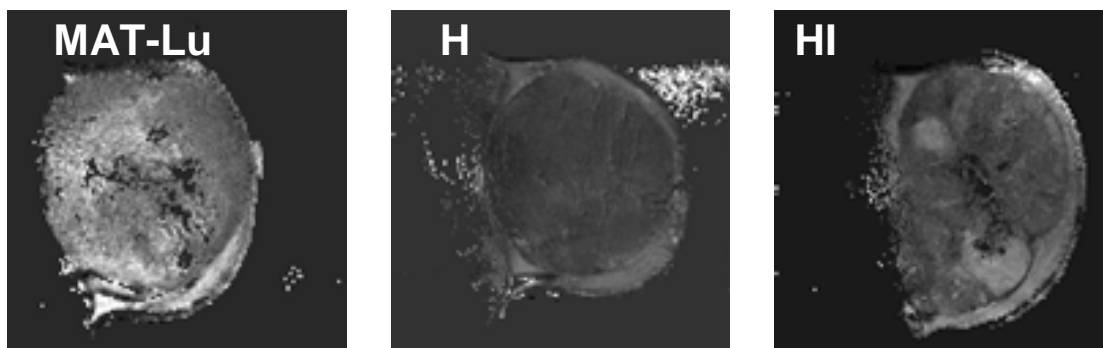


**Figure 9. Apparent diffusion maps obtained by proton MRI at 4.7 T of Dunning prostate R3327 tumors growing in rats.** Each image represents a slice of a tumor observed *in vivo* presenting diffusion maps obtained with 4 b-value diffusion gradients (MR parameters, FOV = 30 mm, TR = 2,300 ms, TE= 50 ms, in plane resolution 230  $\mu\text{m}$ , slice thickness 2 mm with a total acquisition time of 20 mins)

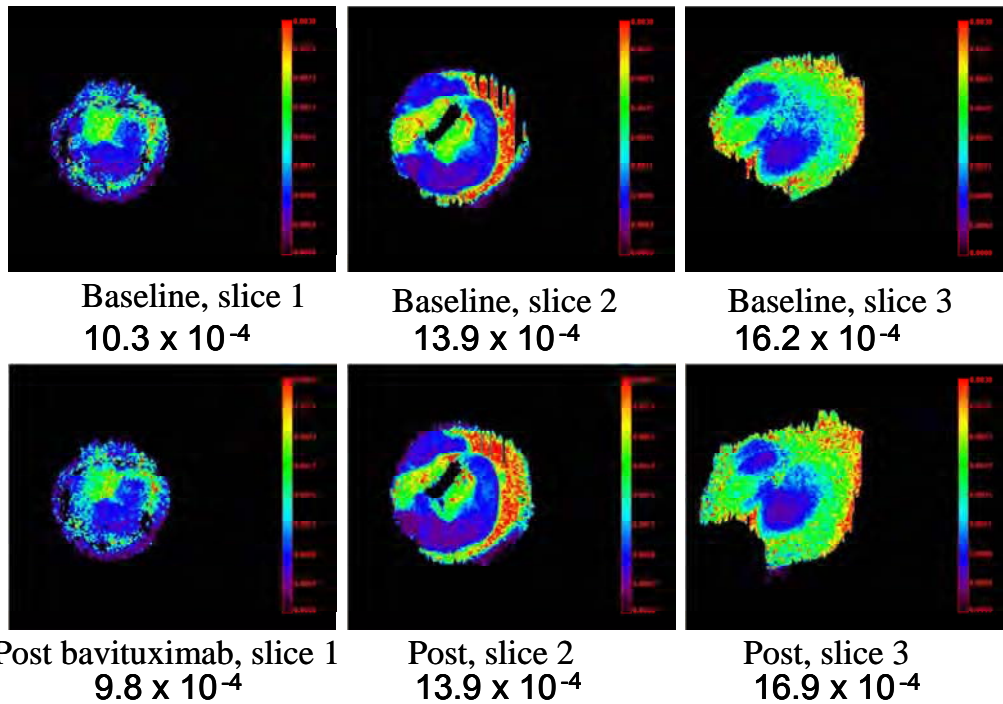


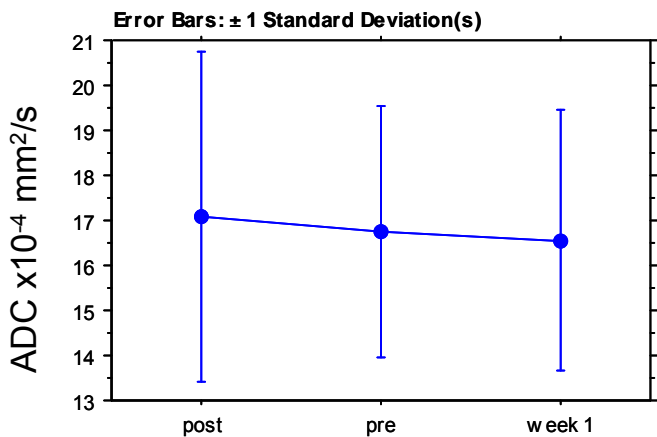
**Figure 10.** Apparent diffusion maps obtained by proton MRI at 4.7 T of Dunning prostate R3327-AT1 tumor. Data as for Figure 9, but showing three consecutive image slices in representative AT1 tumor. Distinct baseline heterogeneity is apparent with mean ADC ranging from  $10.2 \times 10^{-4}$  to  $16.2 \times 10^{-4}$   $\text{mm}^2/\text{s}$ . The lower image shows the same slices 2 h after administration of 2.5 mg/kg bavituximab. There were no significant acute changes.

	Mean	Std. Dev.
AT1	12.9	.92
H	2.6	3.83
HI	16.7	2.80
MAT-Lu	11.8	2.44

Fisher's PLSD for ADC pre  
Effect: Tumor type  
Significance Level: 5 %

	Mean Diff.	Crit. Diff	P-Value	
AT1, H	10.292	3.710	<.0001	S
AT1, HI	-3.839	3.153	.0196	S
AT1, MAT-Lu	1.079	3.349	.5083	
H, HI	-14.130	3.387	<.0001	S
H, MAT-Lu	-9.213	3.570	<.0001	S
HI, MAT-Lu	4.918	2.987	.0027	S

**Table 4.** Left Relative ADC values for groups of Dunning prostate tumors. Right Statistical comparison of ADC values for tumor types showing levels of significance for analysis of variance based on Fisher's test for HI tumors below:



Fisher's PLSD for ADC  
Effect: Time  
Significance Level: 5 %

	Mean Diff.	Crit. Diff	P-Value
post, pre	.337	3.314	.8335
post, week 1	.525	3.580	.7622
pre, week 1	.188	3.580	.9139

**Figure 11.** Variation in ADC with respect to bavituximab administration Data shown for a group of 7 HI tumors. No significant changes were observed.

**DOCENT** (Dynamic Oxygen Challenge Evaluated by NMR  $T_1$  and  $T_2^*$ ).

We have found that BOLD (blood oxygen level dependant) and TOLD (tissue oxygen level dependent) responses to hyperoxic gas breathing directly reflect tumor hypoxia and its response to hyperoxic gas breathing in Dunning prostate rat tumors (Figs. 12 and 13) based on  $^{19}\text{F}$  oximetry and BOLD/TOLD comparisons of corresponding cohorts of rats. It should be noted that the BOLD/TOLD measurements used carbogen as the hyperoxic gas, while many of the  $^{19}\text{F}$  measurements used oxygen. As shown in figures 12 and 13, BOLD and TOLD responses clearly reflect the  $p\text{O}_2$  changes found using  $^{19}\text{F}$  MRI (FREDOM). Small HI tumors showed large increases in both  $T_2^*$ - and  $T_1$ -weighted signal in response to breathing carbogen (hyperoxic challenge) (mean maximum  $\Delta\text{SI}$  (%) =  $20.2 \pm 0.8$  and  $6.5 \pm 0.2$ , respectively). Large HI and small AT1 tumors showed moderate increase in signal intensity in both  $T_2^*$ - and  $T_1$ - weighted signal (mean maximum  $\Delta\text{SI}$  (%) =  $8.2 \pm 0.4$  and  $4.6 \pm 0.1$  for big HI and  $5.1 \pm 0.1$  and  $3.5 \pm 0.1$  for small AT1, respectively). On the other hand, there was little response to breathing carbogen in large AT1 tumors (mean maximum  $\Delta\text{SI}$  (%) =  $0.0 \pm 0.1$  and  $1.17 \pm 0.05$ , respectively). While our acquisition sequences were specifically  $T_2^*$ -weighted or  $T_1$ -weighted, we note that each case could be subject to modulation by the other parameter. Inspection of the response curves in Figures 12 and 13 shows different kinetics, shapes and asymptotes for the BOLD and TOLD responses indicating that sensitivity to each parameter is valid. As expected,  $T_2^*$  changes preceded  $T_1$  changes indicating enhanced vascular oxygenation led to subsequent increased tissue  $p\text{O}_2$ .

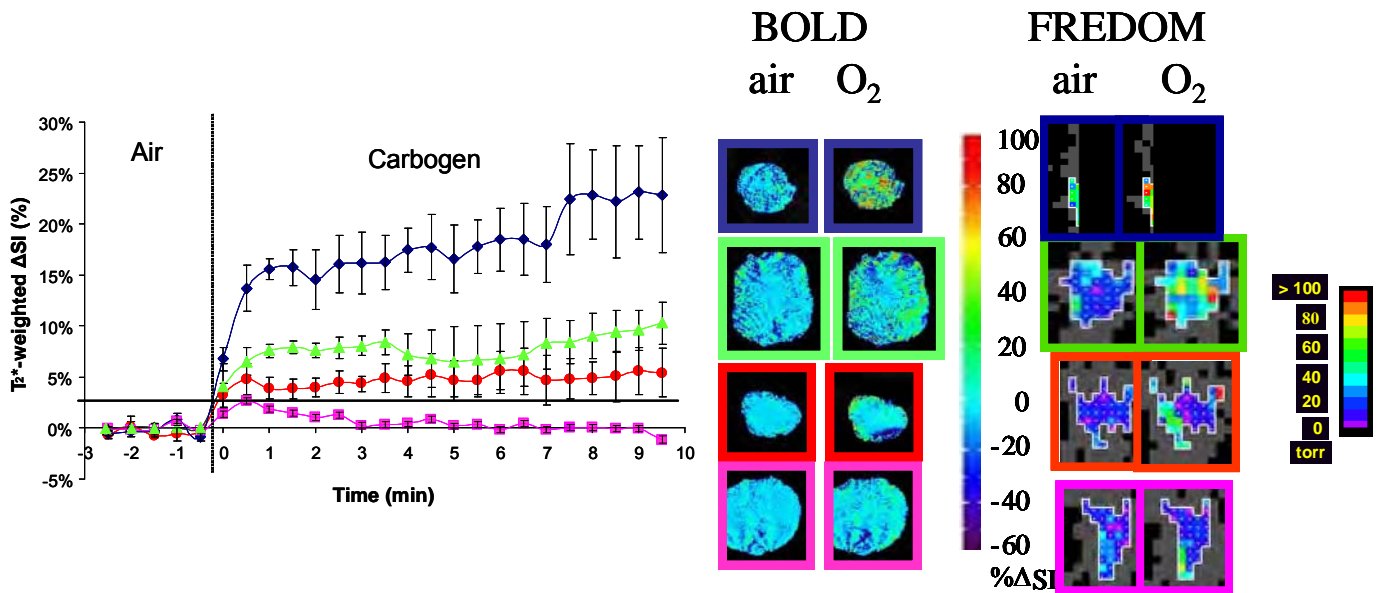


**Figure 12. BOLD dynamics** BOLD ( $T_2^*$ -weighted) signal response was examined in groups of Dunning prostate AT1 and HI tumors, known to exhibit differential response based on  $^{19}\text{F}$  MRI (36, 37). Small HI (n=5) (dark blue), small AT1 (n=8) (red line) and large HI (n=3) (green line) tumors all showed a large signal response ( $>2\%$ ) to carbogen breathing. It was particularly large for the small HI tumors ( $>10\%$ ). Large AT1 tumors (n=3) (pink line) showed a significantly smaller response.

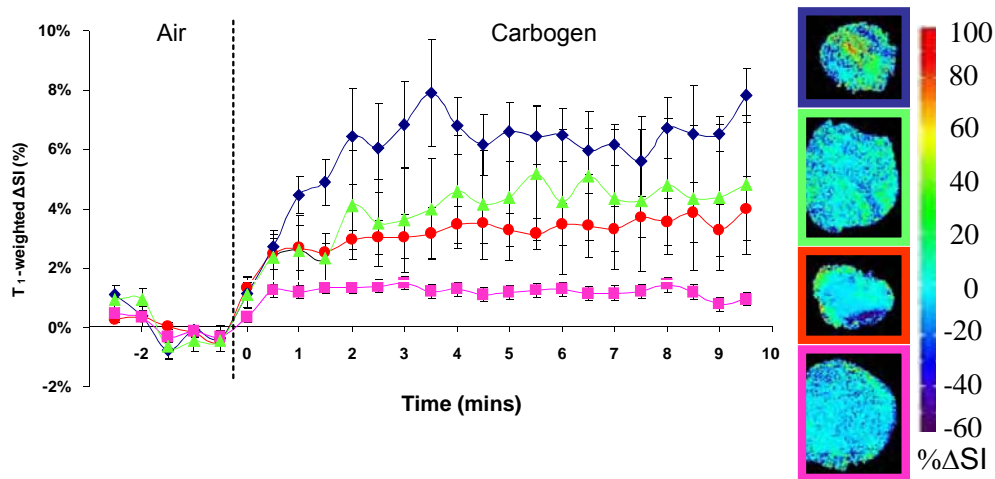


**Figure 13. TOLD dynamics** Interleaved with the  $T_2^*$  response in Figure 12,  $T_1$ -weighted signal response was also examined in the groups of Dunning prostate AT1 and HI tumors. As for  $T_2^*$  response, small HI (blue), AT1 (red) and large HI (green) tumors all showed a large signal response, while large AT1 tumors (pink) showed a significantly smaller response.

Changes in  $T_1$  and  $T_2^*$  correspond closely with previous reports based on quantitative  $^{19}\text{F}$  NMR oximetry (36, 37). Specifically, large AT1 tumors are hypoxic and resist modulation by hyperoxic gas (6). These preliminary data suggest that  $T_1$ - and  $T_2^*$ -weighted signal response to carbogen challenge reveals unresponsive hypoxic tumors. There appear to be three types of tumor in terms of hypoxia and its modulation by breathing hyperoxic gas. Category III tumors (well oxygenated and hence no benefit from  $\text{O}_2$  breathing) show a BOLD  $T_2^*$  signal increase of  $>10\%$  and  $T_1$  increase  $>5\%$ . Category I tumors (hypoxic and resistant to modulation, hence no therapeutic benefit from breathing  $\text{O}_2$ ) have  $\Delta\text{SI} < 2\%$  for both  $T_1$ - and  $T_2^*$ -weighted imaging. Category II tumors, which show a  $\Delta\text{SI}$  for both  $T_1$ - and  $T_2^*$ -weighted imaging in the range 2 to 10% and exhibit therapeutic benefit from the host breathing oxygen during irradiation. These are the most critical to identify, since the simple adjuvant of breathing oxygen is expected to enhance therapeutic response. Since such measurements are entirely non-invasive they appear worthy of further exploration and correlation with response to therapy. We are now funded to undertake rigorous correlative investigations to validate these initial observations (R01 CA139043-01A1). Significantly, such measurements have the potential for rapid translation to the clinic and could facilitate identification of patients with hypoxic tumors, both resistant and amenable to interventions. Indeed, these methods are being incorporated into a DOD CDMRP Prostate Initiative clinical trial for underserved men in collaboration with Dr. Timmerman (PC074348).

### Task 3: Months 3-15

Response to multiple doses of Baviximab. Use MRI to measure  $\text{pO}_2$ , perfusion characteristics and diffusion characteristics of tumors with respect to repeated Baviximab administration (assess response over a period of weeks/months by MRI and tumor volume). Completed.

MAT-Lu tumors show heterogeneous baseline  $\text{pO}_2$ , but generally minimal acute response to administration of baviximab.

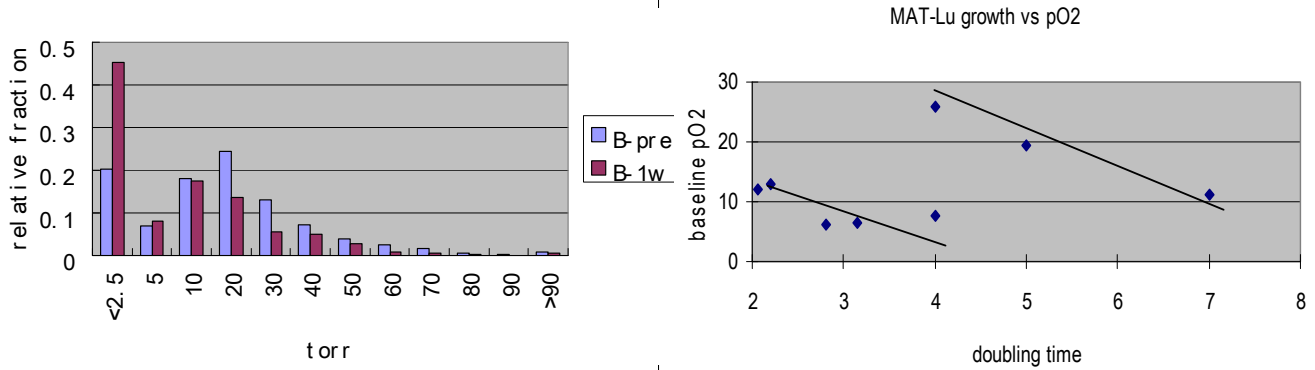


**Figure 14. Chronic changes in pO<sub>2</sub> accompanying multiple doses of bavituximab in MAT-Lu tumors.** **Left:** Histogram presents distribution of pO<sub>2</sub> values measured using <sup>19</sup>F MR oximetry for a group of 8 small tumors. Blue bars are pre therapy and purple 7 days later after 3 doses (2.5 mg/kg) of bavituximab. Distinct hypoxiation of these tumors is apparent. This may be due to the drug, but is likely attributable to rapid growth seen in the tumor which has about 2 day volume doubling time (VDT). **Right:** There appear to be correlations between pre-therapy baseline pO<sub>2</sub> and time (days) to double in volume during bavituximab therapy (thrice weekly). However, tumors appear to fall into two separate groups, requiring further evaluation.

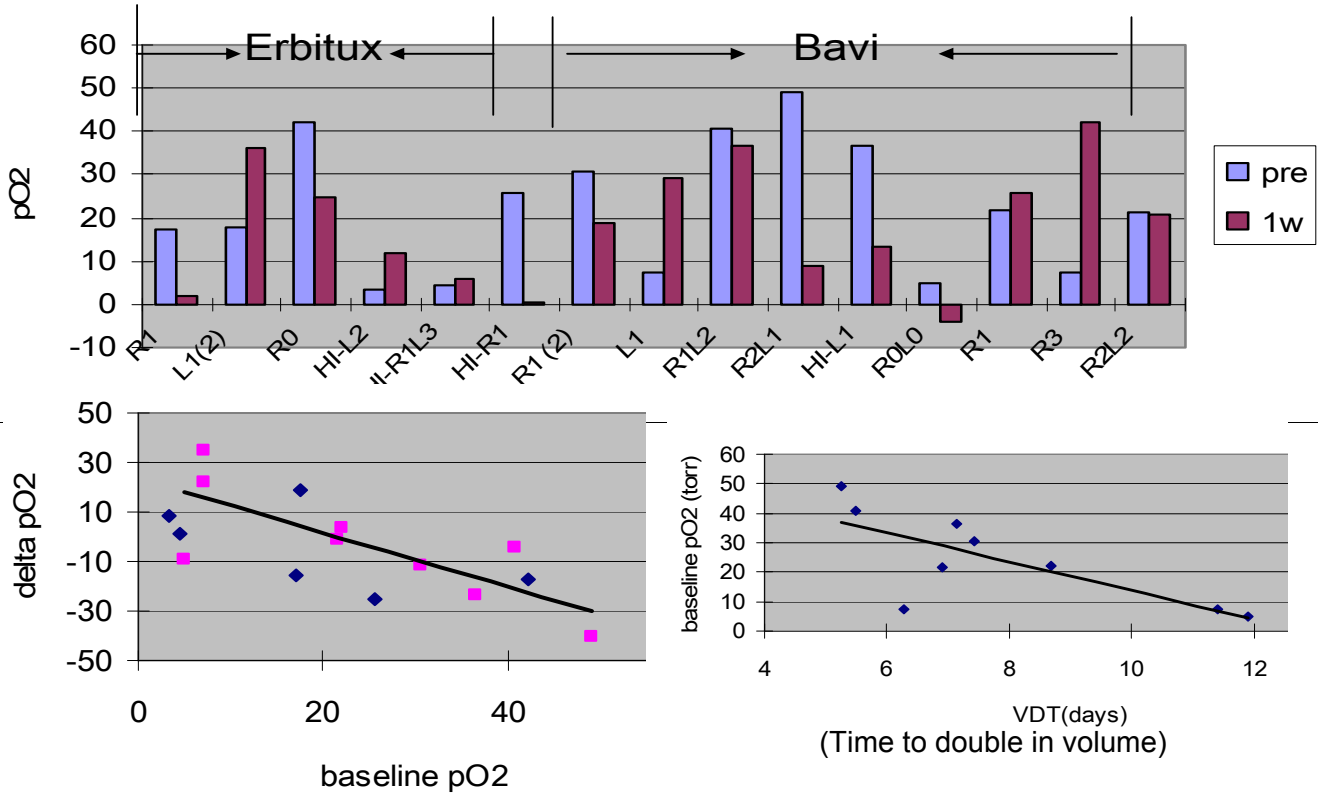


**Figure 15. Chronic changes in pO<sub>2</sub> accompanying multiple doses of bavituximab in HI tumors.**

Upper: Histogram comparing pO<sub>2</sub> pre treatment and after 7 days (3 doses) of bavituximab or control antibody erbitux.

Lower graphs- left- Change in pO<sub>2</sub> over 7 days of treatment ( $\Delta pO_2$ ) with erbitux (pink) or bavituximab (blue) appears to be related to baseline pO<sub>2</sub> prior to therapy. Right: Time to double in volume during therapy appears to be related to baseline pO<sub>2</sub>, as also seen for MAT-Lu tumors in Figure 14.

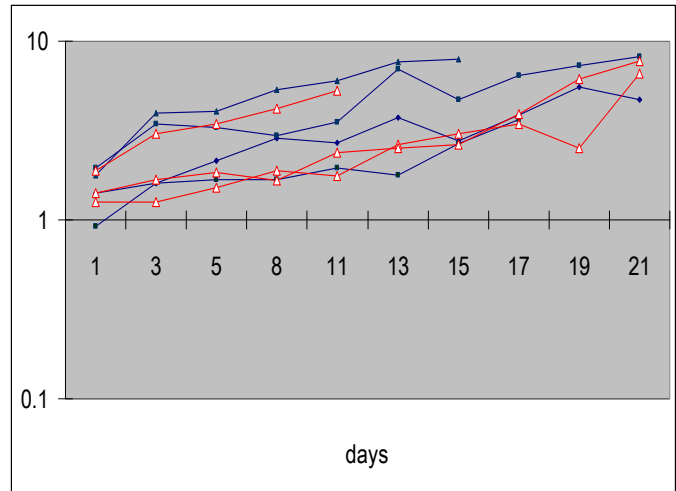
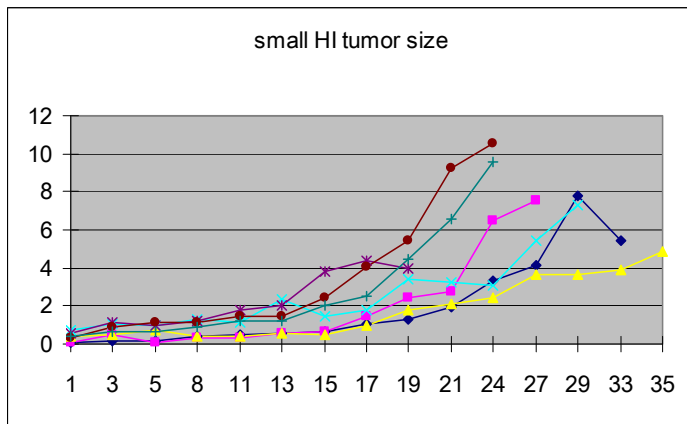


**Figure 16. Growth curves for HI tumors with respect to bavituximab therapy.**

Left: individual small tumors all receiving bavituximab; right: individual medium sized tumors receiving treatment (thrice weekly) with erbitux (red) or bavituximab (blue).

H tumors indicated strong therapeutic response (Figure 17). Each tumor showed either reduction in growth or tumor shrinkage. Tumors of the faster growing cell lines appeared to respond less well to therapy. However, they generally develop massive central necrosis with only a thin peripheral rim of viable tumors. In many cases this was revealed as ulceration leaving a donut cavity. Thus, there is extensive tumor control, but volume measurement based on respective dimensions alone does not appropriately reveal the control.

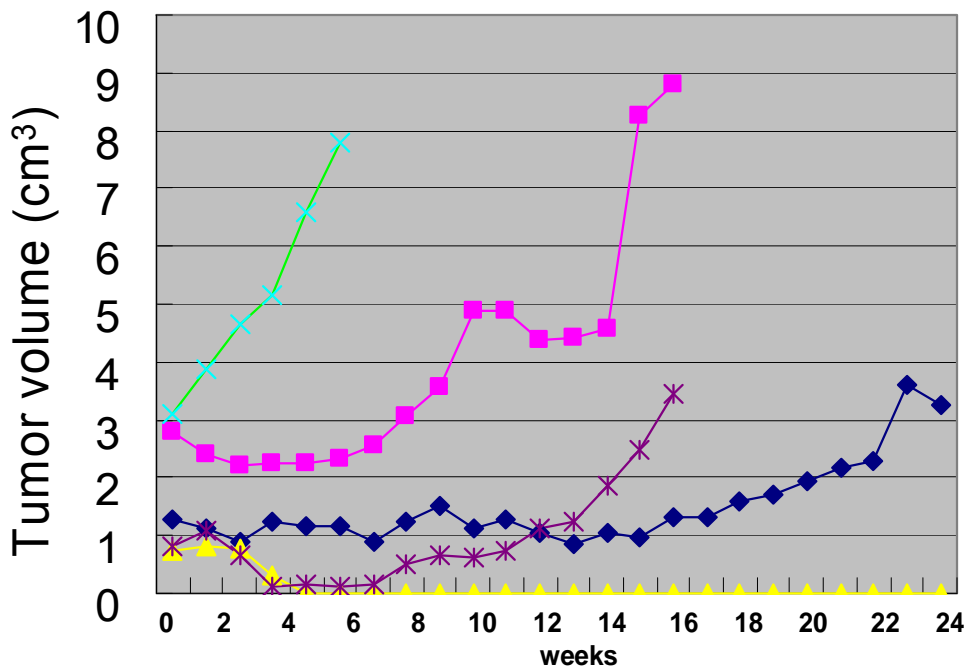


**Figure 17. Growth curves for H tumors with respect to bavituximab therapy.** Growth curves for initial groups of control and bavituximab-treated H tumors. Separate curves are shown for highly responsive small H tumors (yellow ▲; n=2); responsive small tumors (blue ◆; 1 tumor) and somewhat less responsive large tumors (pink ■; 2 tumors). Bavituximab treated tumors received 2.5 mg/kg IP thrice weekly starting on day 1. For comparison a large tumor designated by green label received equivalent dose of control, antibody rituximab.

We have continued the assessment of treatment of H tumors with bavituximab. Inexplicably, the latest investigations show essentially no growth delay even for small H tumors (Fig. 18).

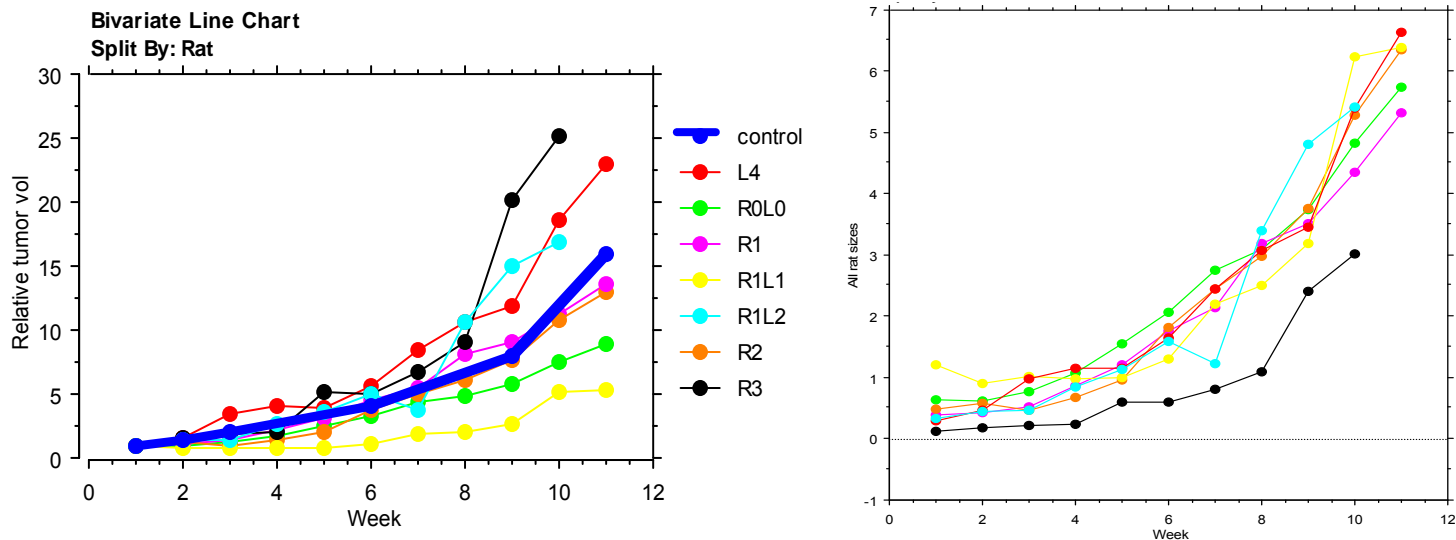


**Figure 18. Growth rates of Dunning prostate R3327 - H tumors with respect to repeat doses of bavituximab.**

Left: Relative tumor volumes for 7 individual small H tumors measured over a period of 11 weeks of thrice weekly treatment with bavituximab (2.5 mg/kg IP). A predicted mean growth rate for untreated control tumors shown by the thick blue line. Apparently some treated tumors grew faster than controls although some indicate tumor growth delay. Right: absolute tumor volumes based on caliper measurements for the tumors at left. Intriguingly, the two tumor showing largest growth delay (R1L1 and R0L0) also showed quite different DCE MRI characteristics at 7 days compared with most tumors (Figure 19).

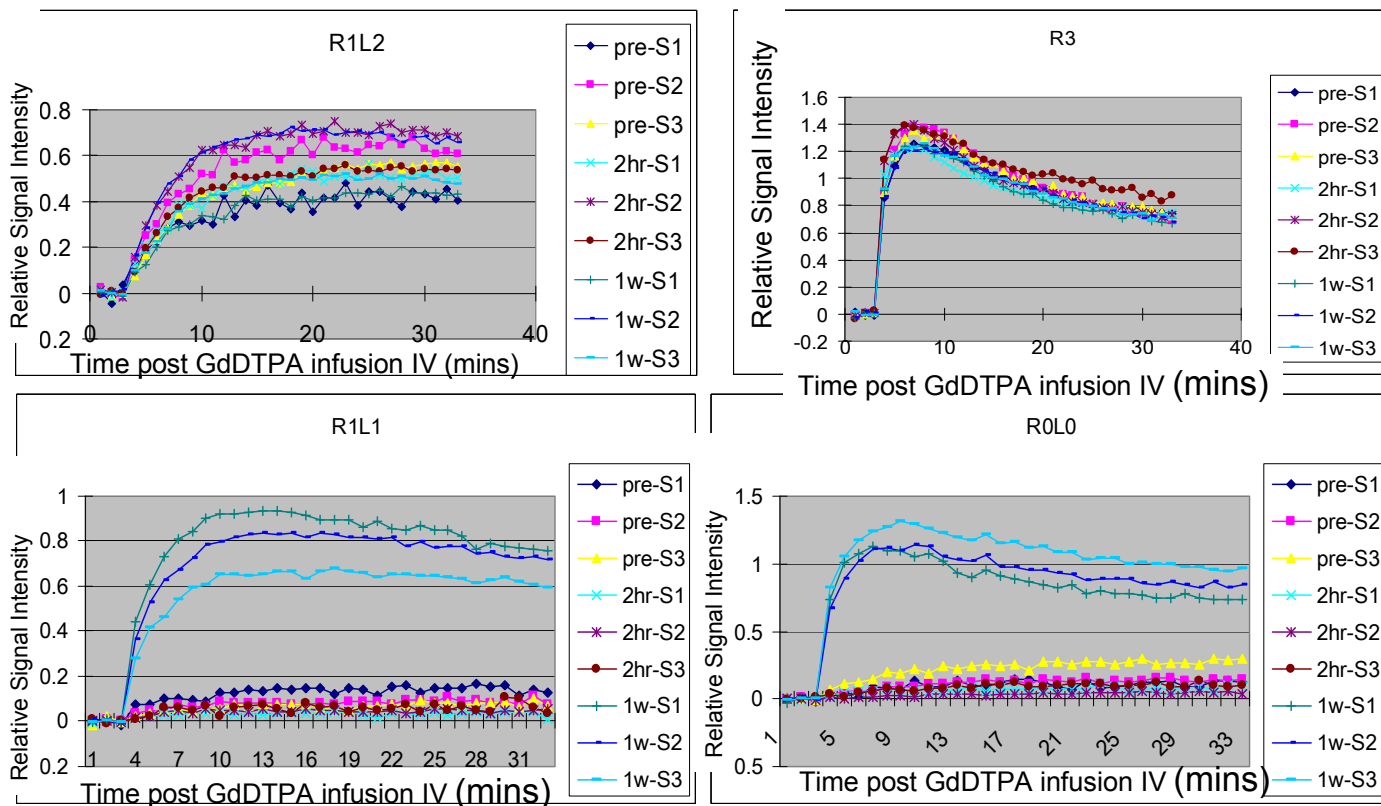


**Figure 19. DCE curves for representative H tumors with respect to bavituximab therapy.** For each tumor signal intensity–time curves are presented for three consecutive parallel slices through the tumor following bolus administration of Gd-DTPA. Investigations were repeated 2 h later and after 7 days (following three doses of bavituximab). Tumors R1L2 and R3 show essentially no variation in the curves for the repeat measurements

and each appears to grow faster than predicted control tumor in Figure 18. However, R1L1 and R0L0 both show growth rates considerably slower than control and greatly increased DCE response after 7 days. It is tempting to suggest that this represents vascular normalization as postulated by Rakesh Jain in his analysis of vascular targeting agents (38).

**Task 4: Months 3-18**

Histological analysis- assess distribution of Bavituximab, necrosis, hypoxia, perfusion based on dyes and antibodies.

Histology confirmed different tumor characteristics such as hypoxia and levels of PS expression. Tumors have been stored and provided an archive for ongoing IHC. Data were included in the manuscript published in Clinical Cancer Research ((39) appended).

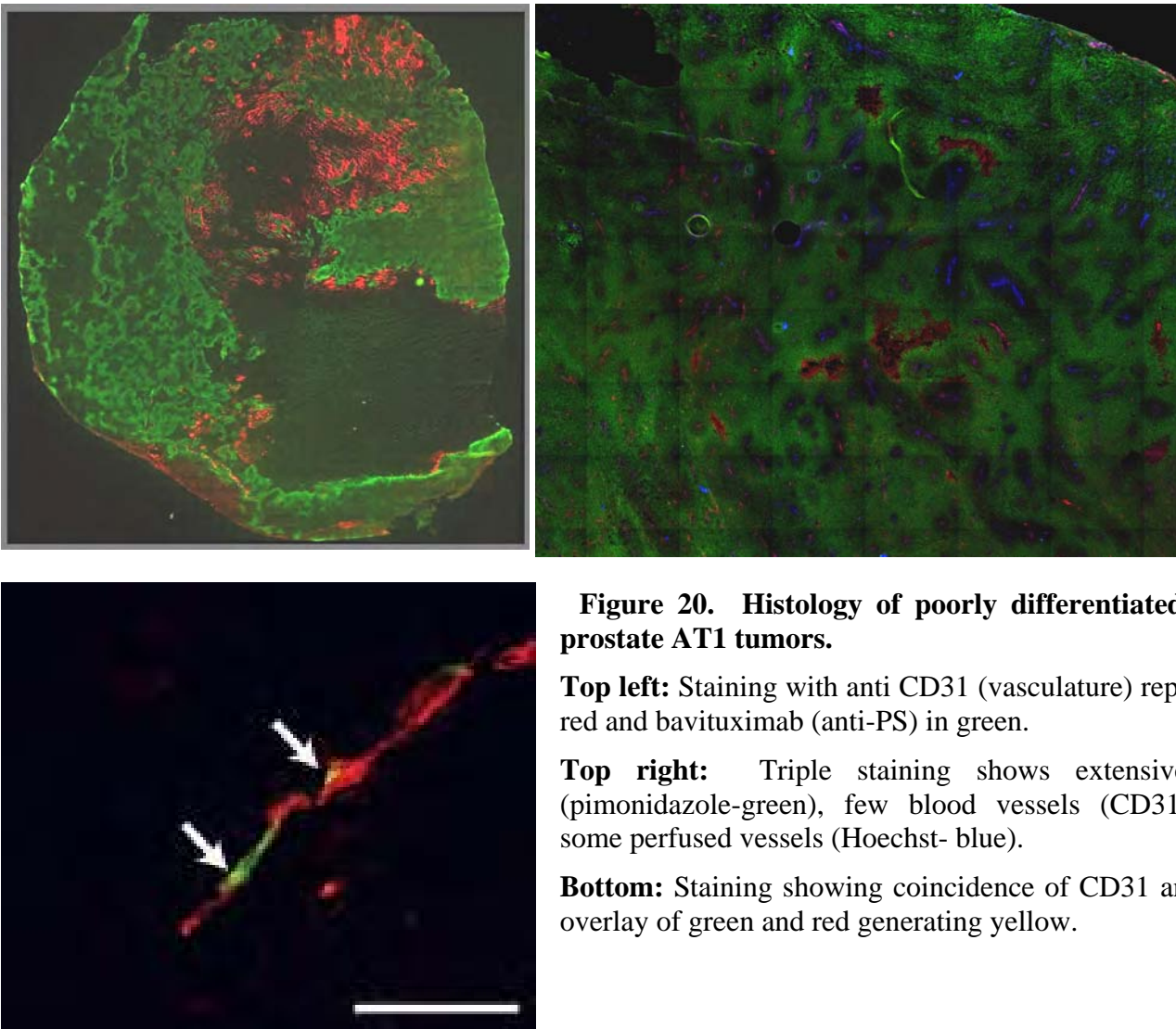


**Figure 20. Histology of poorly differentiated Dunning prostate AT1 tumors.**

**Top left:** Staining with anti CD31 (vasculature) represented in red and bavituximab (anti-PS) in green.

**Top right:** Triple staining shows extensive hypoxia (pimonidazole-green), few blood vessels (CD31-red), and some perfused vessels (Hoechst- blue).

**Bottom:** Staining showing coincidence of CD31 and PS with overlay of green and red generating yellow.

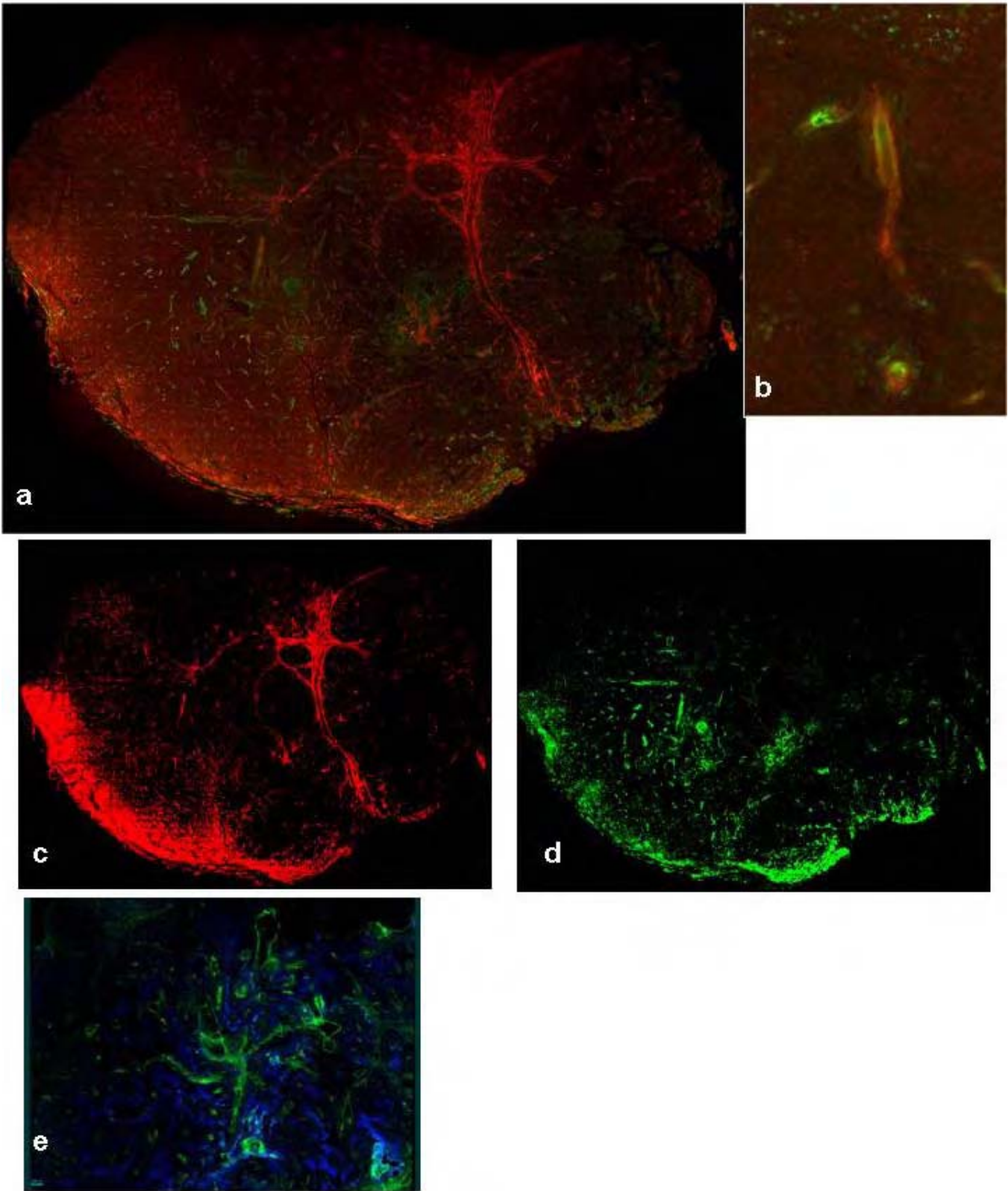


**Figure 21: Histology of moderately differentiated Dunning prostate HI tumors.**

- a) Whole mount showing bavituximab (PS) green on CD31 red; b) magnification showing overlap in blood vessel. c) Color separation of showing CD31 in red; d) color separation showing bavituximab in green; and e) PS in green and hypoxia based on pimonidazole in blue.

**Task 5: Month 12**

Prepare annual report and manuscript.

Completed and approved.

**Task 6: Months 15-18**

Implant tumors of the four sublines R3327- MAT-Lu, AT1, HI and H (6 tumors of each of 4 sublines with 3 treatment sizes (0.5 cm, 1 cm, 1.5 cm diameter; respectively 0.06 cm<sup>3</sup>, 0.5 cm<sup>3</sup>, 1.7 cm<sup>3</sup>) = 144 experimental rat tumors: Tasks 7 and 8 are based on these rats).

Completed year 2

**Task 7: Months 16-30**

Assess tumor growth delay in response to combined Vatumixab<sup>TM</sup> with tirapazamine (SR4233: 3-amino-1,2,4-benzotriazine 1,4 dioxide). Use MRI to assess differential response to therapy compared with tumors receiving Vatumixab<sup>TM</sup> alone.

Growth of small AT1 tumors based on external caliper measurements with respect to various drug combinations. Since tumors are expected to be hypoxic the hypoxia selective cytotoxin tirapazamine was added. For comparison data are shown for the standard chemotherapeutic docetaxel.

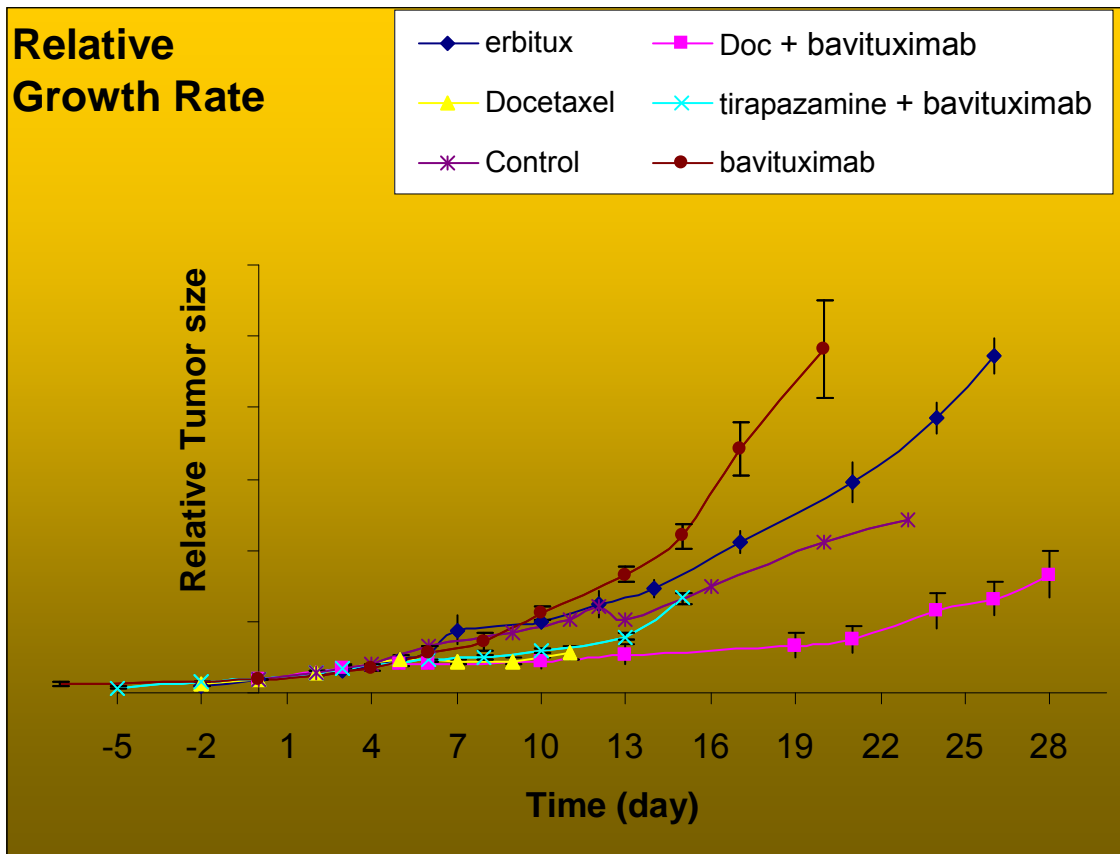


**Figure 22. Growth curves for groups of treated AT1 tumors**

Purple \* control untreated tumors; brown ● bavituximab at 2.5 mg/kg thrice weekly; cyan x bavituximab (2.5 mg/kg IP thrice weekly) + tirapazamine (25 mg/kg IP weekly); blue ◆ control antibody –erbitux (2.5 mg/kg thrice weekly); yellow ▲ - docetaxel (5 mg/kg, ip- only 4 doses due to toxicity) pink ■ bavituximab (2.5 mg/kg IP thrice weekly) + docetaxel (2.5 mg/kg, ip - only 4 doses due to toxicity). Either docetaxel alone or in combination provided the most effective tumor growth delay. However the required dose of docetaxel alone (5

mg/kg) caused unacceptable toxicity, whereas the addition of baviximab provided similar control at a lower, much better tolerated dose.

**Task 8: Month 24**

Prepare annual report and manuscript.

Completed and approved.

**Phase 3 - Evaluate combined therapy (Vatuximab™ plus tirapazamine) in models of advanced metastatic prostate cancer using xenografts in an intra osseous model.**

**Task 9: Months 24-30**

Implant luciferase transfected tumors of each of the tumor types PC3 and C4-2 (LNCaP) in femur of nude mice. Multiple tumors of both sublines have been implanted. This model is not trivial and approximately 50% of mice from the first implantation cycle died within 24 h of implantation. A second attempt by a new technician using smaller tumor cell inoculums gave a more reasonable 20% attrition and this is now reproducible in our hands.

**Task 10: Months 24-34**

Assess tumor growth and therapeutic efficacy. Mice will be examined weekly to assess tumor burden using bioluminescent imaging. C4-2 tumors will also be assessed based on PSA in blood. MRI will be used to assess tumor perfusion. Six groups of tumors will be evaluated” three each with PC3 and C4-2 tumors. For each tumor type there will be control untreated tumors, tumors treated with Vatuximab™ alone and tumors treated with combined Vatuximab™ and tirapazamine (60 nude mice)

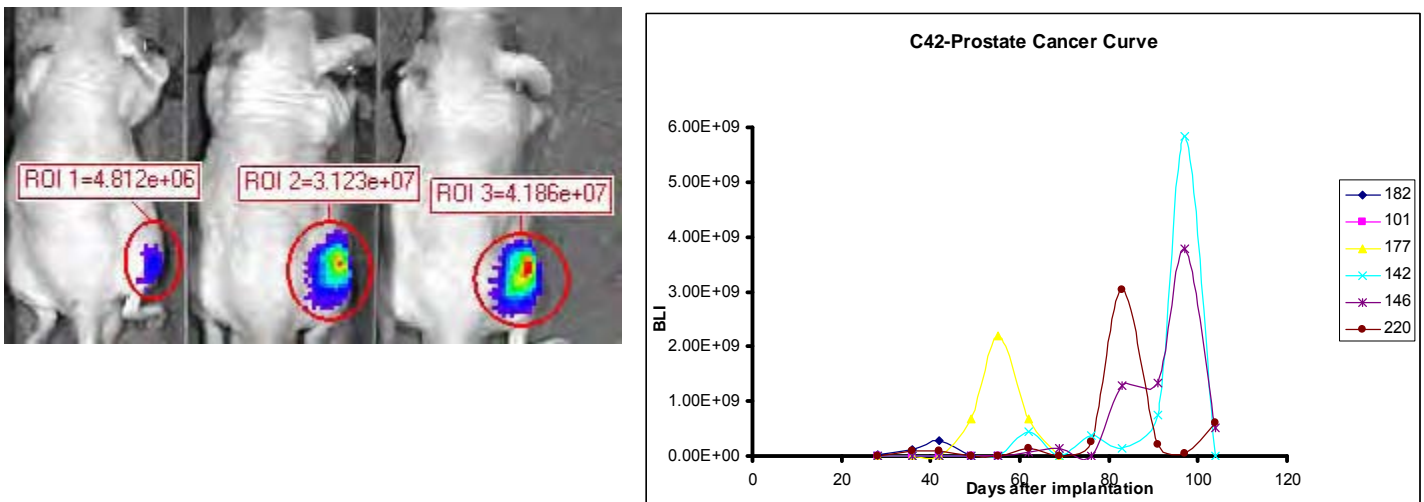


**Figure 23. BLI of intra osseous C4-2 tumors.**

A representative group of nude mice with C4-2 tumors growing intra osseously following implantation in right femur. Images acquired using a Caliper Xenogen Spectrum system in 3 s, 10 mins after administration of 100 mg/kg luciferin SC.

The graph below shows BLI intensity for a group of six C4-2 tumors over a period of 105 days. Overall light intensity increased, but unexpected oscillations in intensity were observed and studies with C4-2 were discontinued.

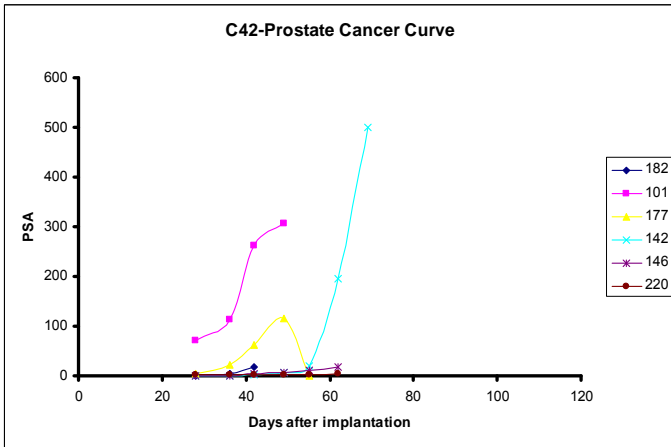


**Figure 24. PSA levels for developing C4-2 tumors.** Prostate specific antigen was measured in blood samples over a period of 70 days following tumor implantation. Levels varied greatly, but a close correlation between PSA and BLI intensity was observed for the tumors shown in graphs below.

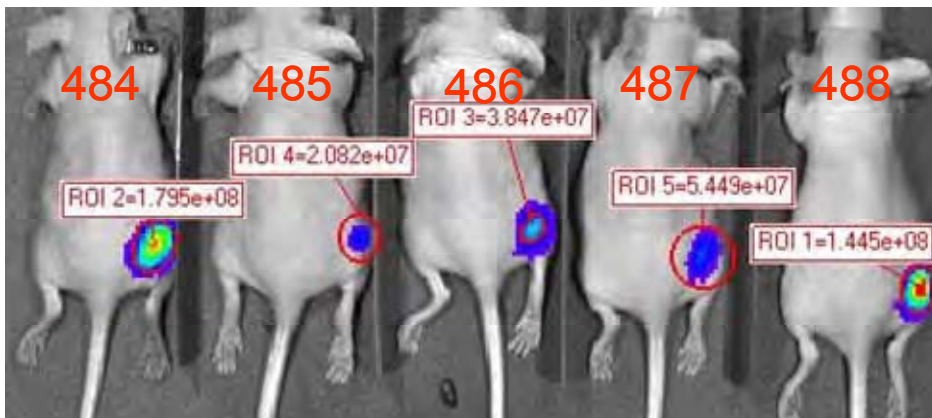
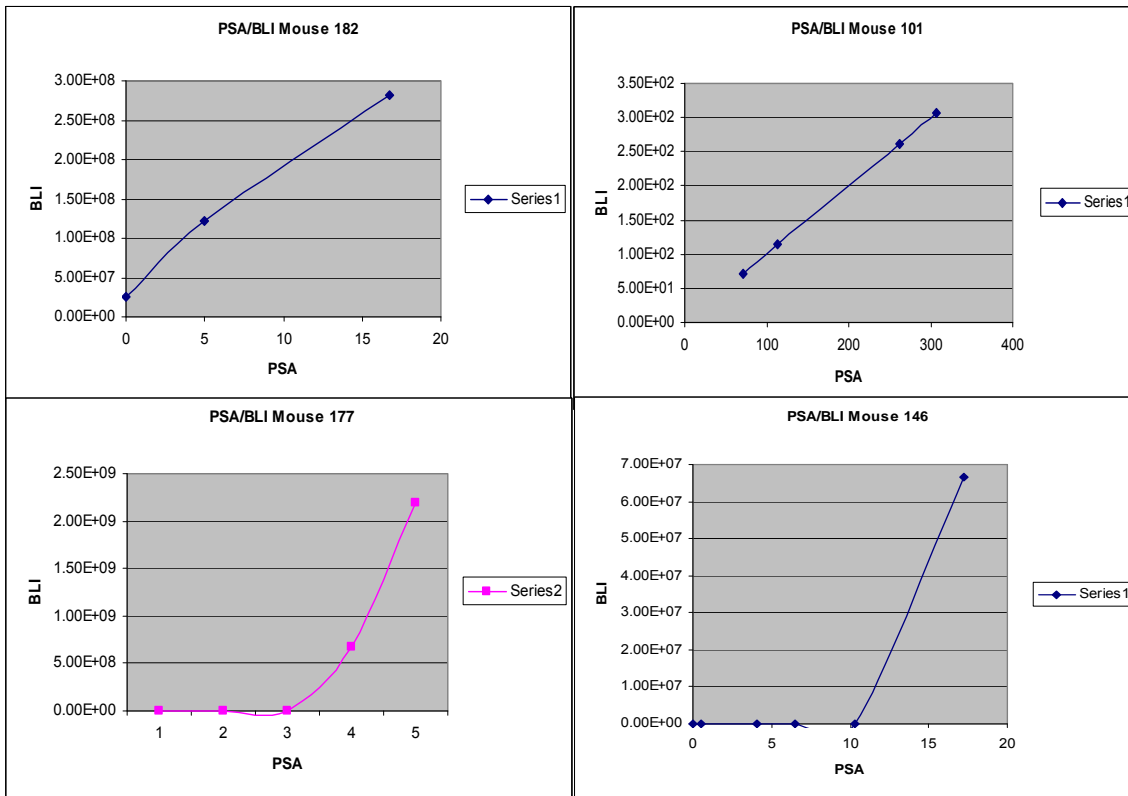
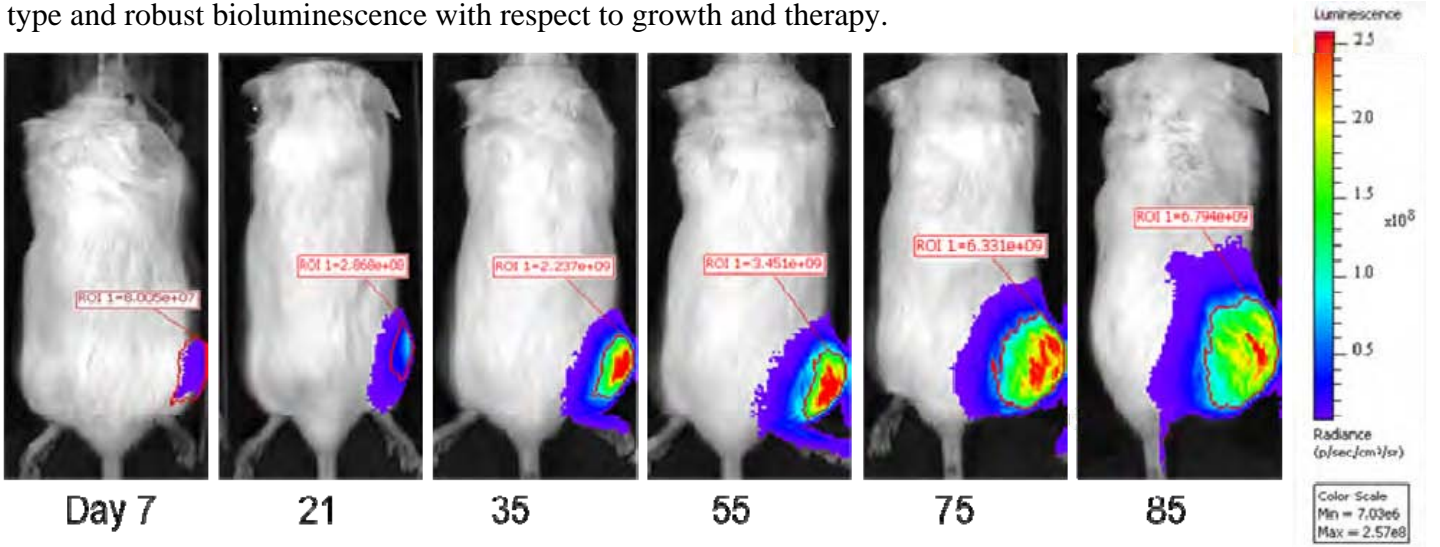


**Figure 25. BLI of intra osseous PC3-luc tumors.** Human tumors growing in femur of nude mice.

An initial PC3-luc tumor line appeared to exhibit gene silencing. Based on BLI alone the tumor appeared to regress even in the absence of therapy, and yet visually the tumors continued to grow. Therefore, new clones were developed and one was chosen, which provides strong luciferase expression, similar growth rate to wild type and robust bioluminescence with respect to growth and therapy.



Above- control tumor growth: intrasosseous PC3-luc; below same tumor model treated with 2aG4 and docetaxel

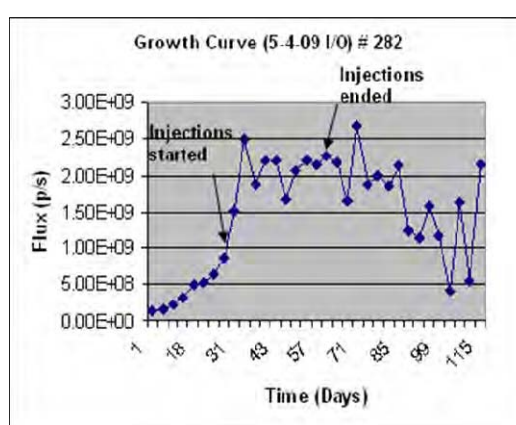
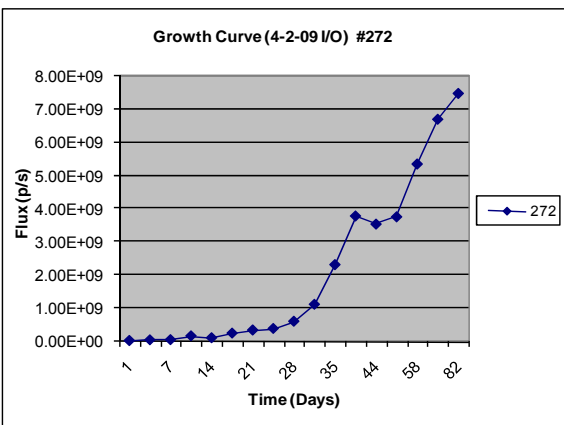
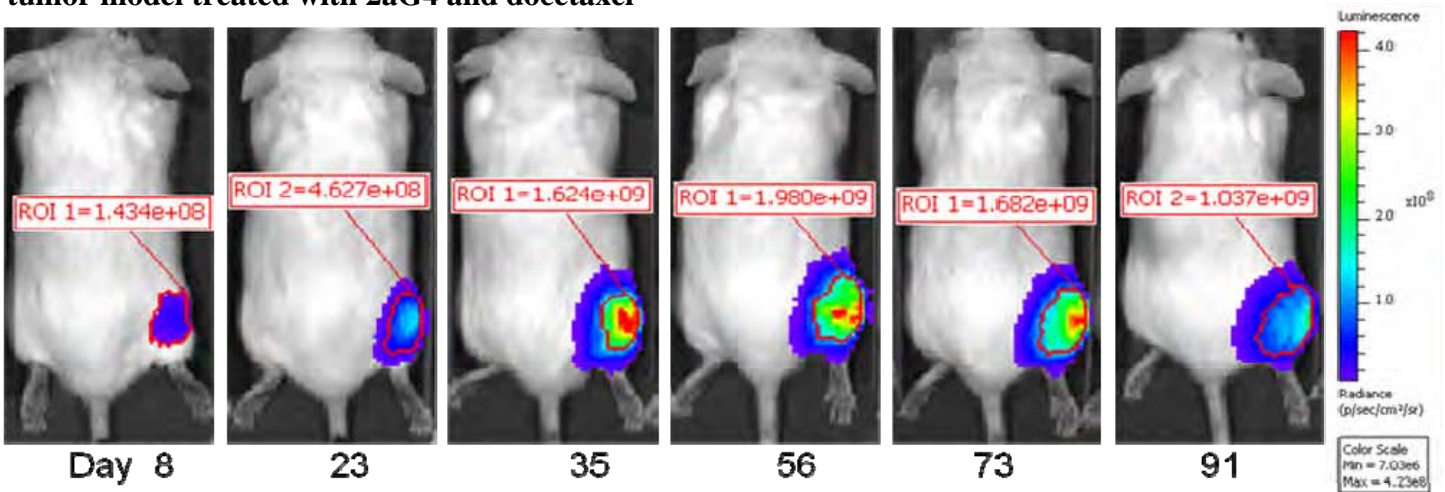
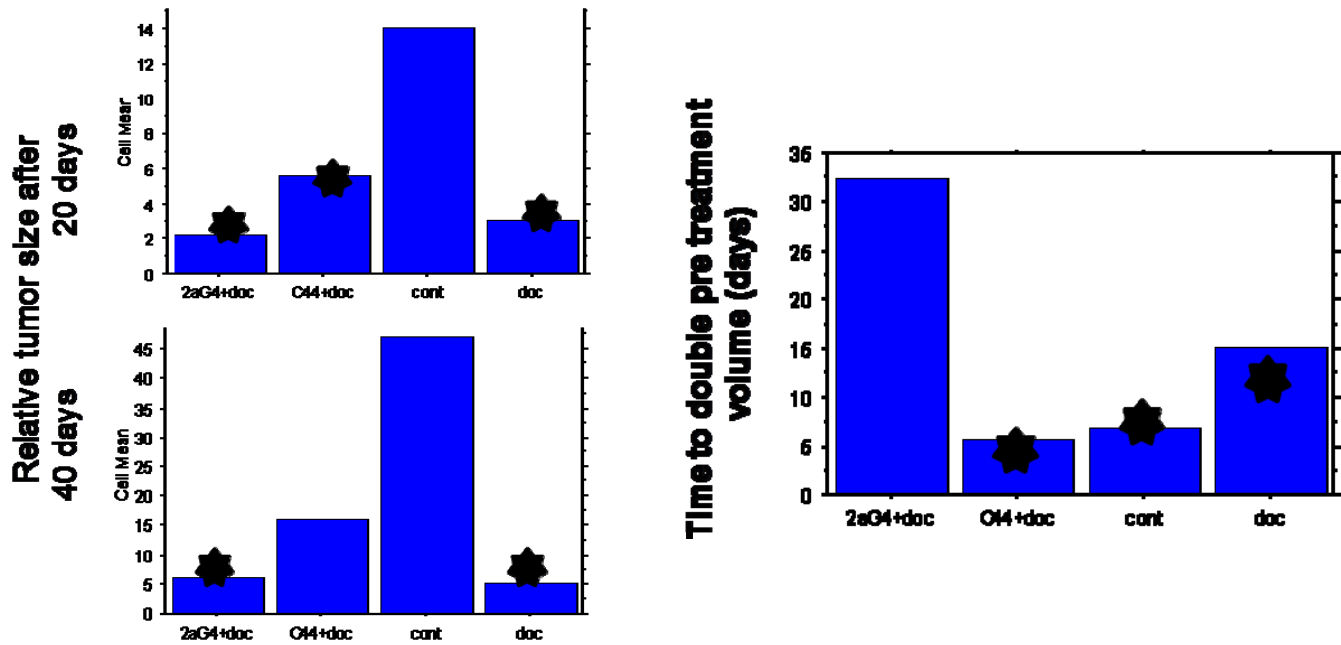


Figure 26. Assessment of PC3 tumor growth with respect to therapy.

Sequential bioluminescent images are shown for two PC3-luc tumors growing in SCID mice. Upper row was control and lower row treated with bavituximab +

docetaxel. Curves show BLI light intensity for these representative mice- control at left (#272) and #282 receiving twice weekly 2aG4 (enhanced bavituximab) antibody.  $\beta 2$  glycoprotein 1 was added as a required co-factor for studies in mice. In addition, docetaxel was administered. BLI was repeated weekly. The control tumor showed continuous growth until sacrifice. By comparison the treated tumor appeared to stop growing after the 2<sup>nd</sup> dose of bavituximab + docetaxel and tumor control remained stable for about 3 months, even after therapy ceased.



**Figure 27. Assessment of PC3 tumor growth with respect to therapy.**

Groups of mice received i) 2aG4 (enhanced bavituximab 100  $\mu$ g, twice weekly + docetaxel 5 mg/kg, 2x weekly) or ii) control C44 (100  $\mu$ g, twice weekly + docetaxel 5 mg/kg, 2x weekly) antibody or iii) no therapy or iv) docetaxel alone (5 mg/kg, 2x weekly = 10 mg/kg/week). For groups (i) and (ii)  $\beta$ 2 glycoprotein-1 (100  $\mu$ g, 2x weekly) was added as a required co-factor for studies in mice. Twenty days after starting therapy all treated groups were significantly smaller ( $p < 0.05$ ) than control tumors (graph at upper left). After 40 days Groups (i) and (iii) were significantly smaller than control, but not Group iii. Data can also be analyzed in terms of time to double in pre-treatment volume and this shows that the 2aG4 + docetaxel group had significantly longer volume doubling time than any of the other groups  $p < 0.05$ ; graph at right).

#### **Task 10: Months 34-36**

Prepare manuscript and final report.

The report is provided herewith.

#### **KEY RESEARCH ACCOMPLISHMENTS:**

- Examined changes in tumor oxygenation in response to bavituximab administration. Only HI tumors showed significant hypoxiation.
- Examined changes in tumor perfusion following bavituximab. Only H tumor showed significant change (reduction)
- No changes in apparent diffusion coefficients were found following bavituximab administration.
- Some H tumors showed significant reduction in growth rate (based on tumor volume) and growth delay (or shrinkage) was maintained over many weeks while additional doses of bavituximab were administered.
- The faster growing rat tumors showed central necrosis and tumor control based on histological examination, but simply measuring whole tumor volume did not readily reveal tumor control due to peripheral rim which continued to grow.

- In rats bavituximab + docetaxel gave strongest growth delay, but docetaxel causes weight loss and severe toxicity.
- Bioluminescent imaging conveniently reveals tumor growth in the femur as an intra osseous model of prostate tumor metastasis in mice.
- In mice bavituximab + docetaxel gave significant growth delay.
- Generated new clones of PC3 human prostate tumors stably expressing luciferase, as well as secondary reporter genes, such as mCherry.
- Discovered that BOLD (blood oxygen level dependant contrast) and TOLD (tissue oxygen level dependant contrast) <sup>1</sup>H MRI appear to serve as surrogates for evaluating tumor hypoxia. We achieved robust population average data and are now funded to pursue rigorous investigations in individual tumors as a foundation for personalized hypoxia sensitive medicine. While others had previously exploited BOLD and TOLD separately we have combined them as part of a new test: DOCENT (Dynamic Oxygen Challenge Evaluated by NMR T<sub>1</sub> and T<sub>2</sub>\*).

## REPORTABLE OUTCOMES:

### 1. Peer-reviewed Papers

Peer-reviewed manuscripts were published. Each credits this grant and is based in part on studies funded by the grant. The papers are included in the appendix.

- Jennewein M, Lewis MA, Zhao D, Tsyganov T, Slavine N, He J, Watkins L, Kodibagkar VD, O’Kelly S, Kulkarni P, Antich PP, Hermanne A, Rösch F, Mason RP and Thorpe PE,” Vascular imaging of solid tumors in rats with a radioactive arsenic-labeled antibody that binds exposed phosphatidylserine” *Clin. Cancer Res.*, 14: 1377-1385 (2008).
- Kodibagkar VD, Wang X, Pacheco-Torres J, Gulaka P and Mason RP “Proton Imaging of Siloxanes to map Tissue Oxygenation Levels (PISTOL): a tool for quantitative tissue oximetry” *NMR Biomed* 21 899-907 (2008)
- Kodibagkar VD, Wang X, Mason RP. “Physical principles of quantitative nuclear magnetic resonance oximetry.” *Front Biosci.* 13:1371-84 (2008).

### 2. Book Chapter

- “Non-Invasive Physiology and Pharmacology Using <sup>19</sup>F Magnetic Resonance”, J.X. Yu, W. Cui, D. Zhao, and R. P. Mason, CHAPTER 5, In FLUORINE AND HEALTH, A. Tressaud & G. Haufe (Eds) 2008 Elsevier B.V.

### 3. Submitted manuscript

- “Blood Oxygen Level Dependent (BOLD) and Gd-DTPA dynamic contrast enhanced (DCE) MRI: comparison of two prostate tumor sublines exhibiting different vascular development”, L. Jiang, D. Zhao, E. W. Hahn, A. J. van der Kogel, J. Bussink, P. Peschke, and R. P. Mason under revision

### 4. Peer-reviewed Grants

Research results have formed the basis for new CDMRP sponsored prostate cancer research. In addition, research results and the needs of this current grant directly assisted UT Southwestern winning significant grants for infrastructure from the NCI. These will both enhance the current studies and future prostate cancer research at UT Southwestern and the surrounding community.

New CDMRP prostate cancer initiative grants building on developments in current grant:

1. Timmerman (PI UT Southwestern)  
“Stereotactic Body Radiation Therapy for Underserved Populations of Men With Low- and Intermediate-Risk Prostate Cancer”  
PC074348 US Department of Defense 05/08-05/11
2. Nguyen (PI UT Arlington- subcontract to UT Southwestern Cui and Hsieh)  
“Polymer Magnetic Nanogels as Targeted and Controlled Drug Release Carriers”  
W81XWH-08-PCRP-IDA DOD Prostate Cancer Idea Development Award  
02/01/2009-01/31/2012
3. Thorpe (PI UT Southwestern)  
“Targeting Phosphatidylserine to Improve Hormone Therapy of Prostate Cancer”  
PC081501 - (FY08) DOD PCRP Prostate Cancer Idea Development Award
4. Yin (PI UT Southwestern)  
“Androgen Deprivation Therapy Induces a Marker for Immunotherapy of Prostate Cancer”  
PC080475 (FY08) DOD PCRP Post doc Award

New NIH grants building on foundation

5. Kumar (PI Tufts University- subcontract to UTSW Mason)  
”Fluorinated Cell Surfaces to Modulate Biological Function”  
NIH/NCI 1R01CA125033-01A2
6. Mason (PI UT Southwestern)  
NIH/NCI  
Hypoxia and Radiotherapy: Evaluation and Mitigation in Tumors  
Major Goal: Develop a prognostic test to reveal tumor hypoxia  
R01 CA139043-01A1 - 01/10 – 12/14

Infrastructure at UT Southwestern building on foundation of current grant

7. Mason (PI UT Southwestern)  
NIH/National Cancer Institute \$334,600  
Small Animal Bioluminescence and Fluorescence Imaging System (with 3D capability)  
Major Goal: Purchase a commercial bioluminescence imaging system to accelerate development of new therapies in cancer research  
1S10RR024757-01 - 04/01/08 – 03/31/09
8. Mason (PI UT Southwestern)  
ARRA-NIH \$295,533  
Small Animal Ultrasound System (VisualSonics Vevo 770)  
Role: Principle Investigator  
1S10RR02564801 - 05/09 - 04/10
9. Mason (PI UT Southwestern)  
NIH – SAIR \$300,000 annual  
UT Southwestern Small Animal Imaging Resource Program

Major Goal: Oversight of multi-modality imaging resource  
1U24CA126608-01 - 03/01/07 – 02/28/12

10. Willson (PI UT Southwestern)  
NIH/NCI \$1,000,000  
Cancer Center Support Grant  
Major Goal: Provide Infrastructure support  
Role: Resource Director  
P30 CA142543-01 - 01/01/10 – 12/31/14

## 5. Conference proceedings

- i) “Differential physiological response to carbogen of two diverse prostate tumor lines detected by tissue water  $^1\text{H}$  MRI”, J. Pacheco-Torres, D. Zhao, J. McAnally, and R. P. Mason, *Second International Conference of European Society for Molecular Imaging*, Naples, Italy , June 14-15, 2007
- ii) “Vatuximab<sup>TM</sup>: Optimizing Therapeutic Strategies For Prostate Cancer Based on Dynamic MR Tumor Oximetry”, R. P. Mason; W. Cui; D. Zhao; A. J. van der Kogel; J. Bussink; J. Pacheco Torres; J. McAnally; L. Watkins; P. Peschke; and P. Thorpe. *Innovative Minds in Prostate Cancer Today - IMPaCT* meeting, September 5-8, Atlanta, Georgia, 2007. It may also be viewed at [http://www.utsouthwestern.edu/vgn/images/portal/cit\\_56417/62/36/410903DOD\\_poster\\_for\\_ralph\\_pdf.pdf](http://www.utsouthwestern.edu/vgn/images/portal/cit_56417/62/36/410903DOD_poster_for_ralph_pdf.pdf)
- iii) “DOCENT-Dynamic Oxygen Challenge Evaluated by NMR T<sub>1</sub> and T<sub>2</sub>\* of Tumors”, D. Zhao, J. Pacheco Torres, P. Peschke and R. P. Mason, *Imaging in 2020 Jackson Hole* 2007. It may also be viewed at [http://www.utsouthwestern.edu/vgn/images/portal/cit\\_56417/15/33/416771Imaging2020-2007.pdf](http://www.utsouthwestern.edu/vgn/images/portal/cit_56417/15/33/416771Imaging2020-2007.pdf)
- iv) “DOCENT (Dynamic Oxygen Challenge Evaluated by NMR T<sub>1</sub> and T<sub>2</sub>\* of Tumors) - new methodology for measuring tumor oxygenation” J. Pacheco-Torres, D. Zhao, A. Contero, S. Cerdan and R. P. Mason, *ESMRB*, Valencia Spain 2008
- v) “DOCENT- Dynamic Oxygen Challenge Evaluated by NMR T<sub>1</sub> and T<sub>2</sub>\* of Tumors”, J. Pacheco-Torres, D. Zhao, A. Contero, P. Peschke, and R. P. Mason, *16<sup>th</sup> ISMRM, # 450, Toronto, Canada*, May 2008
- vi) “Tumor oxygen dynamics assessed non-invasively” J. Pacheco-Torres, D. Zhao, P. Peschke, S. Cerdan, **R. P. Mason**. 100<sup>th</sup> Annual meeting AACR, #237, Denver CO April 2009

New prostate cancer tumor stable clones developed as part of this research:

PC3-luc, PC3-mCherry, PC3-luc-mCherry.

**CONCLUSIONS:** Bavituximab causes little acute pathophysiological response in prostate tumors. Its effect is more subtle than classic vascular disrupting agents. In combination with docetaxel there was significantly enhanced tumor growth delay, notably in the intra osseous model of metastatic prostate cancer. Non-invasive oxygen sensitive  $^1\text{H}$  MRI (BOLD and TOLD) reveals hypoxic versus well oxygenated or oxygenatable tumors promising a new approach to characterizing tumors *in situ*. This may provide a practical approach for stratifying

patients for hypoxia sensitive therapy. Since hypoxic tumors are reported to be more aggressive, an assessment of prostate cancer hypoxic may help stratify patients for appropriate watchful waiting versus aggressive therapy and potentially predict efficacy of radiotherapy.

## References

1. Thorpe, P. E., Chaplin, D. J., and Blakey, D. C. The first international conference on vascular targeting: meeting overview. *Cancer Res.*, *63*: 1144-1147, 2003.
2. Thorpe, P. E. Vascular Targeting Agents as Cancer Therapeutics. *Clin. Cancer Res.*, *10*: 415-427, 2004.
3. Burrows, F. J. and Thorpe, P. E. Vascular-targeting- a new approach to the therapy of solid tumors. *Pharmacol. Ther.*, *64*: 155-174, 1994.
4. Ran, S., Downes, A., and Thorpe, P. E. Increased exposure of anionic phospholipids on the surface of tumor blood vessels. *Cancer Res.*, *62*: 6132-6140, 2002.
5. Ran, S., He, J., Huang, X., Soares, M., Scothorn, D., and Thorpe, P. E. Anti-tumor effects of a monoclonal antibody directed against anionic phospholipids on the surface of tumor blood vessels in mice. *Clin. Cancer Res.*, *11*: 1551-1562, 2005.
6. Ran, S. and Thorpe, P. E. Phosphatidylserine is a marker of tumor vasculature and a potential target for cancer imaging and therapy. *Int. J. Radiat. Oncol. Biol. Phys.*, *54*: 1479-1484, 2002.
7. Peregrine <http://ir.peregrineinc.com/phoenix.zhtml?c=74236&p=irol-newsArticle&ID=696919&highlight=>.
8. Zhao, D., Constantinescu, C., Hahn, E. W., and Mason, R. P. Differential oxygen dynamics in two diverse Dunning prostate R3327 rat tumor sublines (MAT-Lu and HI) with respect to growth and respiratory challenge. *Int. J. Radiat. Oncol. Biol. Phys.*, *53*: 744-756, 2002.
9. Zhao, D., Ran, S., Constantinescu, A., Hahn, E. W., and Mason, R. P. Tumor oxygen dynamics: correlation of in vivo MRI with histological findings. *Neoplasia*, *5*: 308-318, 2003.
10. Lohr, F., Wenz, F., Flentje, M., Peschke, P., and Hahn, E. Measurement of proliferative activity of three different sublines of Dunning rat prostate tumor R3327. *Strahlenther. Onkol.*, *169*: 438-445, 1993.
11. Eble, M. J., Wenz, F., Bachert, K. B., Lohr, F., and Peschke, P. Invasive pO<sub>2</sub> histography in Dunning prostate tumor R-3327-AT1 and R3327-HI: Correlation with <sup>31</sup>P-MR spectroscopy and in-vivo radiosensitivity. *In*: P. W. Vaupel, D. K. Kelleher, and M. Günderoth (eds.), *Tumor Oxygenation*, pp. 95-105. Stuttgart: Gustav Fischer, 1995.
12. Peschke, P., Hahn, E. W., Wenz, F., Lohr, F., Brauschweig, F., Wolber, G., Zuna, I., and Wannenmacher, M. Differential sensitivity of three sublines of the rat Dunning prostate tumor system R3327 to radiation and/or local tumor hyperthermia. *Radiat. Res.*, *150*: 423-430, 1998.
13. Isaacs, J. T., Isaac, W. B., Feitz, W. F. J., and Scheres, J. Establishment and characterization of 7 Dunning prostate cancer cell lines and their use in developing methods for predicting metastatic ability of prostate cancer. *Prostate*, *9*: 261-281, 1986.
14. Tennant, T. R., Kim, H., Sokoloff, M., and Rinker-Schaeffer, C. W. The Dunning model. *Prostate*, *43*: 295-302, 2000.
15. Bedikian, A. Y., Legha, S. S., Eton, O., Buzaid, A. C., Papadopoulos, N., Coates, S., Simmons, T., Neefe, J., and von Roemeling, R. Phase II trial of tirapazamine combined with cisplatin in chemotherapy of advanced malignant melanoma. *Ann. Oncol.*, *8*: 363-367, 1997.
16. Rischin, D., Peters, L., Fisher, R., Macann, A., Denham, J., Poulsen, M., Jackson, M., Kenny, L., Penniment, M., Corry, J., Lamb, D., and B., M. Tirapazamine, Cisplatin, and Radiation versus Fluorouracil, Cisplatin, and Radiation in patients with locally advanced head and neck cancer: a randomized phase II trial of the Trans-Tasman Radiation Oncology Group (TROG 98.02). *J Clin Oncol*, *23*: 79-87, 2005.
17. Lara, P. N. J., Frankel, P., Mack, P. C., Gumerlock, P. H., Galvin, I., Martel, C. L., Longmate, J., Doroshov, J. H., Lenz, H. J., Lau, D. H., and Gandara, D. R. Tirapazamine plus carboplatin and

- paclitaxel in advanced malignant solid tumors: a california cancer consortium phase I and molecular correlative study. *Clin Cancer Res*, 9: 4356-4362, 2003.
18. Fabbri, F., Brigladori, G., Carloni, S., Ulivi, P., Tesei, A., Silvestrini, R., Amadori, D., and Zoli, W. Docetaxel-ST1481 Sequence Exerts a Potent Cytotoxic Activity on Hormone-Resistant Prostate Cancer Cells by Reducing Drug Resistance-Related Gene Expression. *Prostate*, 70: 219-227.
  19. Ploussard, G., Paule, B., Salomon, L., Allory, Y., Terry, S., Vordos, D., Hoznek, A., Vacherot, F., Abbou, C. C., Culine, S., and de la Taille, A. Pilot trial of adjuvant paclitaxel plus androgen deprivation for patients with high-risk prostate cancer after radical prostatectomy: results on toxicity, side effects and quality-of-life. *Prostate Cancer and Prostatic Diseases*, 13: 97-101.
  20. Michels, J., Ellard, S. L., Le, L., Kollmannsberger, C., Murray, N., Guns, E. S. T., Carr, R., and Chi, K. N. A phase IB study of ABT-751 in combination with docetaxel in patients with advanced castration-resistant prostate cancer. *Annals of Oncology*, 21: 305-311.
  21. Wu, T. T., Sikes, R. A., Cui, Q., Thalmann, G. N., Kao, C., Murphy, C. F., Yang, H., Zhau, H. E., Balian, G., and Chung, L. W. K. Establishing human prostate cancer cell xenografts in bone: induction of osteoblastic reaction by prostate-specific antigen-producing tumors in athymic and scid/bg mice using LNCaP and lineage-derived metastatic sublines. *Int. J. Cancer*, 77: 887-894, 1998.
  22. Baudelet, C. and Gallez, B. Current issues in the utility of blood oxygen level dependent MRI for the assessment of modulations in tumor oxygenation *Curr Med Imaging Rev.*, 1: 229-243, 2005.
  23. Jiang, L., Zhao, D., Constantinescu, A., and Mason, R. P. Comparison of BOLD contrast and Gd-DTPA Dynamic Contrast Enhanced imaging in rat prostate tumor. *Magn. Reson. Med.*, 51: 953-960, 2004.
  24. Robinson, S. P., Howe, F. A., and Griffiths, J. R. Noninvasive monitoring of carbogen-induced changes in tumor blood flow and oxygenation by functional MRI. *Int. J. Radiat. Oncol. Biol. Phys.*, 33: 855-859, 1995.
  25. Robinson, S. P., Howe, F. A., Rodrigues, L. M., Stubbs, M., and Griffiths, J. R. Magnetic resonance imaging techniques for monitoring changes in tumor oxygenation and blood flow. *Semin. Radiat. Oncol.*, 8: 198-207, 1998.
  26. Robinson, S. P., Collingridge, D. R., Howe, F. A., Rodrigues, L. M., Chaplin, D. J., and Griffiths, J. R. Tumor response to hypercapnia and hyperoxia monitored by FLOOD magnetic resonance imaging. *NMR Biomed*, 12: 98-106, 1999.
  27. Robinson, S. P., Rijken, P. F., Howe, F. A., McSheehy, P. M., van der Sanden, B. P., Heerschap, A., Stubbs, M., Van Der Kogel, A. J., and Griffiths, J. R. Tumor vascular architecture and function evaluated by non-invasive susceptibility MRI methods and immunohistochemistry. *J. Magn. Reson. Imaging.*, 17: 445-454, 2003.
  28. Howe, F. A., Robinson, S. P., McIntyre, D. J., Stubbs, M., and Griffiths, J. R. Issues in flow and oxygenation dependent contrast (FLOOD) imaging of tumours. *NMR in Biomed.*, 14: 497-506, 2001.
  29. Fan, X., River, J. N., Zamora, M., Al-Hallaq, H. A., and Karczmar, G. S. Effect of carbogen on tumor oxygenation: combined fluorine-19 and proton MRI measurements. *Int. J. Radiat. Oncol. Biol. Phys.*, 54: 1202-1209, 2002.
  30. Al-Hallaq, H. A., River, J. N., Zamora, M., Oikawa, H., and Karczmar, G. S. Correlation of magnetic resonance and oxygen microelectrode measurements of carbogen-induced changes in tumor oxygenation. *Int. J. Radiat. Oncol. Biol. Phys.*, 41: 151-159, 1998.
  31. Al-Hallaq, H. A., Zamora, M. A., Fish, B. L., Halpern, H. J., Moulder, J. E., and Karczmar, G. S. Using high spectral and spatial resolution bold MRI to choose the optimal oxygenating treatment for individual cancer patients. *In: Oxygen Transport to Tissue Xxiv*, Vol. 530, pp. 433-440. 2003.
  32. Matsumoto, K., Bernardo, M., Subramanian, S., Choyke, P., Mitchell, J. B., Krishna, M. C., and Lizak, M. J. MR assessment of changes of tumor in response to hyperbaric oxygen treatment. *Magn. Reson. Med.*, 56: 240-246, 2006.
  33. O'Connor, J. P. B., Jackson, A., Buonaccorsi, G. A., Buckley, D. L., Roberts, C., Watson, Y., Cheung, S., McGrath, D. M., Naish, J. H., Rose, C. J., Dark, P. M., Jayson, G. C., and Parker, G. J. M. Organ-specific effects of oxygen and carbogen gas inhalation on tissue longitudinal relaxation times. *Magn. Reson. Med.*, 58: 490-496, 2007.

34. Zhao, D., Jiang, L., and Mason, R. P. Measuring Changes in Tumor Oxygenation. *Methods Enzymol*, 386: 378-418, 2004.
35. Yankeelov, T. E., Luci, J. J., Lepage, M., Li, R., Debusk, L., Lin, P. C., Price, R. R., and Gore, J. C. Quantitative pharmacokinetic analysis of DCE-MRI data without an arterial input function: a reference region model. *Magn Reson Imaging*, 23: 519-529., 2005.
36. Zhao, D., Constantinescu, A., Chang, C.-H., Hahn, E. W., and Mason, R. P. Correlation of Tumor Oxygen Dynamics with Radiation Response of the Dunning Prostate R3327-HI Tumor. *Radiat. Res.*, 159: 621-631, 2003.
37. Bourke, V. A., Zhao, D., Gilio, J., Chang, C.-H., Jiang, L., Hahn, E. W., and Mason, R. P. Correlation of Radiation Response with Tumor Oxygenation in the Dunning Prostate R3327-AT1 Tumor. *Int. J. Radiat. Oncol. Biol. Phys.*, 67: 1179-1186, 2007.
38. Jain, R. K. Normalization of tumor vasculature: an emerging concept in antiangiogenic therapy. *Science*, 307:58-62: 58-62, 2005.
39. Jennewein, M., Lewis, M., Zhao, D., Tsyganov, T., Slavine, N., He, J., Watkins, L., Kodibagkar, V., O'Kelly, S., Kulkarni, P., Antich, P., Hermanne, A., Rösch, F., Mason, R., and Thorpe, P. Vascular imaging of solid tumors in rats with a radioactive arsenic-labeled antibody that binds exposed phosphatidylserine. *Clin. Cancer Res.*, 14: 1377-1385, 2008.

## APPENDICES:

### 1. Abstract for the DOD "Innovative Minds in Prostate Cancer Today - IMPaCT" meeting on September 5-8, 2007, at the Hyatt Regency in Atlanta, Georgia.

Ralph P. Mason; Weina Cui; Dawen Zhao; Albert J. van der Kogel (Department of Radiation Oncology, University Medical Center Nijmegen, Nijmegen, Netherlands); Johan Bussink (Department of Radiation Oncology, University Medical Center Nijmegen, Nijmegen, Netherlands); Jesús Pacheco Torres (Instituto de Investigaciones Biomédicas "Alberto Sols" CSIC/UAM, Madrid, Spain); Jennifer McAnally; Linda Watkins; Peter Peschke (German Cancer Center, Heidelberg, Germany); and Philip Thorpe.

Targeting tumor vasculature promises a new effective therapy for prostate cancer, since a blood supply is required for the tumor to grow and develop. We proposed a new approach, using the novel antibody 3G4 (now called bavituximab), which targets phosphatidylserine (PS) expressed on tumor vasculature. In collaboration with Peregrine Pharmaceuticals, this agent is being developed for clinical trials. Normally, PS exclusively resides on the cytosolic leaflet of the plasma membrane. However, in tumors PS becomes externalized and provides a target. The agent not only targets various tumors, but also induces vascular damage and tumor regression with minimal accompanying toxicity. Our goal is to evaluate the dynamic effects of 3G4 on tumor pathophysiology, so as to optimize combination with additional drugs for synergistic therapeutic response.

Magnetic resonance imaging is used to follow the induction and development of tumor vascular damage *in vivo* in diverse syngeneic rat tumors (Dunning R3327-MAT-Lu, AT1, HI and H) known to exhibit differential vascular extent and growth rates. Specifically, we are examining changes in diffusion coefficients (ADCs), perfusion and vascular leakiness based on dynamic contrast enhancement (DCE) and hypoxiation based on NMR oximetry (*FREDOM*-Fluorocarbon Relaxometry using Echo Planar imaging for Dynamic Oxygen Mapping).

Before therapy all tumors exhibit substantial heterogeneity. MAT-Lu and AT1 tumors exhibit similar ADCs, while HI tumors are significantly greater and H tumors substantially lower. Groups of AT1 and H tumors showed significant differences in DCE signal response between central and peripheral regions. No regional differences were observed for the pharmacokinetic parameter *Kep* for either tumor type. Histology confirmed that H tumors are better perfused and exhibit much less hypoxia (based on Hoechst dye distribution, CD31-staining, and pimonidazole uptake). During baseline air breathing all tumors show quite similar oxygenation patterns typically ranging from regions of hypoxia ( $pO_2 < 5$  torr) to normoxia ( $pO_2 \sim 40$  torr).

Administration of bavituximab produced no significant acute changes in ADC over 2 h. In most tumors there appeared to be no changes in perfusion based on DCE. However, several H tumors indicated reduced perfusion at 2 h, which was restored after 1 week.  $pO_2$  values were quite variable among individual tumors. Most showed no significant response to administration of bavituximab. However, several HI tumors showed significant hypoxiation during the 2 h following administration.

H tumors indicated strong therapeutic response. Each tumor showed reduction in growth or tumor shrinkage. Tumors of the faster growing cell lines appeared to respond less well to therapy. However, many develop massive central necrosis with only a thin peripheral rim of viable tumor, often revealed as ulceration leaving a donut cavity. Thus, there is extensive tumor control, but volume measurement based on respective dimensions alone does not appropriately reveal the extent of control.

Our data are preliminary, but we have demonstrated proof of principle. Importantly, this therapy is associated with little or no toxicity and could be effective at any stage of tumor development. We are initiating combined studies with tirapazamine to exploit the observed hypoxiation. Success will confirm the potential of this new therapeutic approach to prostate cancer in man and lay the foundation for future clinical trials.

## **2. Second International Conference of European Society for Molecular Imaging, June 14-15, 2007 in Naples, Italy**

“Differential physiological response to carbogen of two diverse prostate tumor lines detected by tissue water 1H MRI” J. Pacheco-Torres<sup>1,2</sup>, D. Zhao<sup>2</sup>, J. McAnally<sup>2</sup>, and R. P. Mason<sup>2</sup>

<sup>1</sup>Instituto de Investigaciones Biomédicas "Alberto Sols" - CSIC, Madrid, Spain

<sup>2</sup>University of Texas Southwestern Medical Center, Dallas, Texas, United States

Tumor oxygenation play important roles in cancer malignancy. Recently, studies have suggested a possibility of assessing tissue oxygenation based on the shortening of the tissue water T1 due to oxygen. Here, we are investigating differences in T1- and T2\*-weighted signal intensity, as well as maps of R1, R2 and R2\* in response to carbogen between two Dunning prostate R3327 rat tumor sublines: AT1 (anaplastic and poorly vascularized) and HI (moderately well differentiated and vascularized).

In response to carbogen breathing, significantly increased signal intensity in both T1 and T2\*-weighted images was found in both the tumor lines. Much higher enhancement in both T1 and T2\*-weighted signal was observed in HI compared with AT1 tumors (mean maximum  $\Delta SI(\%) = 8.6 \pm 2.2$  vs.  $5.4 \pm 0.7$  in T1-weighted;  $23.9 \pm 8$  vs.  $9.8 \pm 1.8$  in T2\*-weighted). R1 maps revealed that carbogen induced significantly increased R1 values in both periphery and center of the HI tumors (mean  $\Delta R1 = 0.012$  (periphery) vs.  $0.006$  s<sup>-1</sup> (center);  $p < 0.01$ ), while no significant increase was seen in the AT1 tumors. Similarly, reduction in R2\* values in response to carbogen was found in the HI tumor, but not the AT1 tumors. These results are in line with previous studies in these two tumor lines.

While SI of T1-weighted image increased, T1 values were not shortened in the AT1 tumors with carbogen inhalation. This may be attributed to an increase in blood flow associated with carbogen. Since this approach is totally non-invasive it appears worthy of further investigations for characterizing tumors and response to adjuvant interventions.

## Physical principles of quantitative nuclear magnetic resonance oximetry

Vikram D. Kodibagkar<sup>1</sup>, Xianghui Wang<sup>1</sup>, Ralph P. Mason<sup>1</sup>

<sup>1</sup>Cancer Imaging Program, Department of Radiology, UT Southwestern, Dallas TX

### TABLE OF CONTENTS

1. Abstract
2. Introduction
  - 2.1. Tissue oxygenation and hypoxia
  - 2.2. Measurement of tissue oxygenation
  - 2.3. Magnetic Resonance in Bioscience
3. NMR and MRI oximetry
  - 3.1. Dependence of spin lattice relaxation rate of reporter molecules on pO<sub>2</sub>
  - 3.2. Diamagnetic contributions to R<sub>1</sub>
  - 3.3. Paramagnetic contribution of oxygen
  - 3.4. Measuring pO<sub>2</sub>
  - 3.5. New development: <sup>1</sup>H MRI based oximetry using hexamethyldisiloxane
4. Perspective and Conclusion
5. Acknowledgements
6. References

## 1. ABSTRACT

Over the years many techniques have been devised for the measurement of tissue oxygenation (oximetry). Oximetry using polarographic needle electrodes has long been considered a gold standard. Nuclear Magnetic Resonance (NMR) based oximetry uses exogenously administered reporter molecules such as perfluorocarbons to quantitatively interrogate oxygen tension (pO<sub>2</sub>). This technique has been successfully used *in vivo* in the preclinical setting and shows promise for clinical applications. NMR pO<sub>2</sub> reporter molecules display a linear dependence of the spin lattice relaxation rate on pO<sub>2</sub>, which forms the basis of this technique. Physical principles of spin lattice relaxation of pO<sub>2</sub> reporter molecules and the pO<sub>2</sub> dependence of relaxation rate are discussed in this review. Practical considerations for choice of reporter molecules for *in vivo* measurements, general methodology and new developments are also described.

## 2. INTRODUCTION

### 2.1. Tissue oxygenation and hypoxia

Oxygen is essential for tissue health and any reduction in its supply can lead to rapid cellular dysfunction and cell death. It is also an important variable in the treatment of many medical conditions including tumors, peripheral vascular disease, and stroke. In solid tumors, oxygen delivery is impaired by structural abnormalities present in the tumor vasculature such as chaotic vessel architecture. In addition, the altered tumor cell metabolism with elevated metabolic rates contributes to the occurrence of low tissue oxygenation (hypoxia). Hypoxia can adversely affect the efficacy of radiation therapy, chemotherapy, and photodynamic therapy (1). These therapies rely on creation of reactive oxygen species, which can kill cancer cells by damaging DNA and sub cellular organelles (2). Reactive oxygen species are also formed as a natural byproduct of normal metabolism of

## MR Oximetry

oxygen and have important roles in cell signaling (3). Production of reactive oxygen species from molecular oxygen by macrophages and neutrophils probably plays a key role in cell-mediated immunity and microbiocidal activity (4). Measurements of  $pO_2$  in tumors have been found to have prognostic value and the probability of disease-free survival is significantly lower for patients with hypoxic tumors (5-8). Given the importance of oxygen, the ability to measure tissue oxygen tension non-invasively may have a significant impact in understanding mechanisms of tissue function and in clinical prognosis of disease. Quantitative tissue oximetry remains a challenge, especially *in vivo* and this review will consider progress in magnetic resonance approaches and the physical foundations underpinning the method.

### 2.2. Measurement of tissue oxygenation

Many techniques have been used to assess tissue oxygenation *in vivo*, both qualitative and quantitative as reviewed extensively (1, 9, 10). Direct measurement methods include those using electrodes and fiber-optic probes. These methods have been used for *in vivo* research and also in the clinical setting, but are invasive and may be unsuitable for routine human use. Indirect methods such as those based on Magnetic Resonance (MR) measure parameters that report on local oxygenation status (see section 3).

Measurements of  $pO_2$  using polarographic needle electrodes have long been considered a gold standard (1, 11, 12). Typically, an anode is placed on the skin and polarized with a constant voltage. The polarographic needle electrode (cathode) consists of a gold filament embedded within a flexible stainless steel housing with an oxygen permeable membrane covering the opening. The cathode is inserted into the tissue of interest and electrical current is generated at the tip of the electrode, which is proportional to the tissue oxygen pressure. Polarographic electrodes are calibrated in phosphate buffered normal saline, bubbled with gases with a range of  $pO_2$ s. Multiple electrodes may be placed at different locations in tissue in order to measure spatial heterogeneity and one can make dynamic measurements to gauge the response to intervention (13). The invasiveness of this technique can be minimized by use of electrode tips as fine as a few microns (14), but these are fragile and are susceptible to stray electromagnetic fields. The Eppendorf Histogram is an improved version of this technique that can make multiple successive measurements along tracks in tissue using a stepwise motion of the needle electrode under computer control (15). It has been successfully used in the clinical setting and revealed hypoxia in many tumor types that are externally accessible (6-8, 12, 16-19). The drawbacks of polarographic electrodes are that measurements can be affected by changes in pH, salinity, and ionic strength. Electrodes also consume oxygen, and thus, may bias readings especially under hypoxic conditions (such as found in tumors) and over long measurement periods.

Another quantitative method for measuring the partial pressure of dissolved or gaseous oxygen utilizes fiber-optic oxygen sensors based on fluorescence.

Typically, an optical fiber carries excitation light to the fluorophore coating at the probe tip. Fluorescence generated at the tip is returned by the optical fiber to a spectrometer. When oxygen in the gas or liquid sample diffuses into the fluorophore coating, it quenches the fluorescence. Commercial instruments exploit various parameters such as fluorescence lifetime (OxyLite™) or relative fluorescence intensity (FOXY™), which are correlated with  $pO_2$ , and hence, a calibration curve can be used to measure  $pO_2$  *in vivo*. The fluorophores used in commercial systems may be platinum based (OxyLite™) or ruthenium based (FOXY™). This method does not consume oxygen during measurement, but the fluorophore coating may wear off after several measurements and needs to be re-applied to the fiber. Weak detected fluorescence intensity is a clear sign that fluorophore coating needs to be re-applied. Probes can be coated with oxygen permeable coatings to further protect the fluorophore. This usually slows the response time of measurement. Several recent applications have been reported (20-31). Fiber optic probes are more fragile than the Eppendorf Histogram.

Qualitative methods have been used to non-invasively identify tumor regions that are hypoxic based on selective accumulation of specially designed reporter molecules in such regions (32). Following intravenous infusion, these reporter molecules are trapped in tissues in the absence of oxygen, very much like molecules such as pimonidazole and EF5 that are widely used in histological assessment of hypoxia (33). Many such reporter molecules have been developed for different modalities such as NMR (34-36), positron emission tomography (PET) (37-40) and single photon emission computed tomography (SPECT) (41, 42). The red shift of the fluorescence of green fluorescent protein (GFP) under hypoxic conditions has also been used to image hypoxia by fluorescence imaging (43). Exploiting various biochemical pathways that are under oxygen regulation such as induction of hypoxia-inducible factor 1 (HIF-1) or introduction of transgenes with hypoxic response elements (HREs) coupled to reporter genes has enabled the visualization of hypoxia by optical imaging (44-47).

### 2.3. Magnetic Resonance in Bioscience

In biomedicine, the abundant hydrogen nuclei from tissue water can be utilized to obtain high-resolution anatomical images using Magnetic Resonance Imaging (MRI) to probe living systems non-invasively. Of all medical imaging modalities, MRI provides the best combination of spatial and temporal resolution to yield superb anatomical detail and functional information. It has become an invaluable clinical tool for diagnosis of many diseases. Using tricks of nuclear spin physics it is possible to obtain information beyond structural anatomy. Routinely, one can study diverse aspects of physiology, such as vasculature and blood flow (48-50), cellularity and apparent diffusion (51-54), vascular and tissue oxygenation (9, 55-59) as well as tissue perfusion and endothelial permeability (60, 61). The development of contrast agents and reporter molecules has pushed the limits of detection and established MRI as a tool for molecular imaging (62-64). Assessment of key metabolites such as lactate, choline

## MR Oximetry

and N-acetyl aspartate (NAA) by proton NMR has enabled the assessment of metabolic changes at onset of disease (65-71).

Magnetic Resonance (MR) based techniques to measure oxygenation may be divided into quantitative and qualitative methods. Qualitative MR techniques, such as BOLD (Blood Oxygen Level Dependant) contrast use blood oxygenation status as a surrogate marker for tissue oxygenation. BOLD can provide high spatial and temporal resolution and can assess dynamic changes in vascular oxygenation using endogenous deoxyhemoglobin, and is the basis for functional MRI. For large blood vessels where imaging voxels are wholly within a vessel quantitative oximetry has been reported (55, 72, 73). However, since BOLD contrast (changes in  $T_2^*$ ) depends on the amount of deoxyhemoglobin it is influenced by hematocrit, vascular volume, pH and flow. While signal changes are sensitive to changes in vascular oxygenation, the relationship with tissue  $pO_2$  is neither straightforward nor direct in tissues (58). Quantitative MR oximetry techniques have been developed based on reporter molecules for nuclear magnetic resonance (NMR) (9, 74-76) and electron paramagnetic resonance (EPR) (10, 77-81). EPR is a technique that is very similar to NMR in that they both result from the Zeeman interaction of a spin with an external magnetic field. Unlike NMR where nuclei like protons with non-zero nuclear spin give rise to the signal, EPR relies on unpaired electrons. EPR oximetry, much like NMR oximetry, relies on the indirect methods that exploit the paramagnetic properties of molecular oxygen. Paramagnetic oxygen not only relaxes nuclear spins, but also is effective in electronic  $T_1$  and  $T_2$  relaxation of other paramagnetic species or radicals. The EPR linewidth of the radical is broadened and the change in the relaxation rate is often proportional to the concentration of oxygen over a wide range of oxygen tensions. Similar to NMR oximetry, *in vivo* EPR oximetry also requires prior intravenous or intramuscular infusion of free radicals, or direct implantation of particulate spin probes into the tissue of interest. This technique has been reviewed extensively elsewhere (81, 82). The method can offer exceptional sensitivity at very low  $pO_2$  values. A primary shortcoming is the lack of widespread EPR instrumentation for small animal investigations, *let alone* clinical studies.

Although extensive reviews exist on NMR oximetry (9, 76), they have generally focused on applications. Here, we focus on the underlying physical principles. NMR based oximetry uses exogenously administered reporter molecules to interrogate oxygen tension ( $pO_2$ ). Such exogenous agents, which can quantitatively report tissue oxygenation, have been successfully used *in vivo* in the preclinical setting. NMR  $pO_2$  reporter molecules are often perfluorocarbons, which display a linear dependence of the  $^{19}F$  spin lattice relaxation rate  $R_1$  ( $=1/T_1$ ) on  $pO_2$ . We will also describe an analogous  $^1H$  NMR approach using a recently identified  $^1H$   $pO_2$  reporter molecule hexamethyldisiloxane (83).

## 3. NMR AND MRI OXIMETRY

### 3.1. Dependence of spin lattice relaxation rate of reporter molecules on $pO_2$

Molecular oxygen is paramagnetic and therefore tends to shorten nuclear spin-lattice relaxation times,  $T_1$  and  $T_2$ , in solution or *in vivo*. Most of the NMR oximetry applications utilize the linear dependence of the  $^{19}F$  longitudinal (spin-lattice) relaxation rate ( $R_1=1/T_1$ ) of fluorine nuclei of perfluorocarbons (PFC) on the partial pressure of oxygen (9, 84, 85). PFCs exhibit specific characteristics that are critical for *in vivo* oximetry: high oxygen solubility and hydrophobicity. Hydrophobicity ensures the exchange of gases between the PFC and surrounding tissue, while preventing the exchange of aqueous ions, which could perturb  $R_1$ . The linear dependence of PFC  $R_1$  on  $pO_2$  can be understood as follows. One can visualize two types of PFC molecules in the PFC pool, those with and without oxygen in their vicinity. If those free of oxygen have a **diamagnetic** longitudinal relaxation rate of  $R_{1d}$ , the ones with oxygen in their immediate vicinity have a longitudinal relaxation rate of  $R_{1d} + R_{1p}$ , where  $R_{1p}$  is the **paramagnetic** contribution of oxygen. Since the oxygen molecules rapidly diffuse in the solvent, the observed relaxation rate for each type of fluorine atom is a molar weighted average:

$$R_1 = (1-x)R_{1d} + x(R_{1d} + R_{1p}) = R_{1d} + xR_{1p} \quad (1)$$

where  $x$  is the mole fraction of oxygen. Since PFCs behave as essentially ideal liquids, the solubility of oxygen in the PFCs obeys Henry's law,

$$pO_2 = k * x \quad (2)$$

where  $k$  is a constant that reflects solubility of oxygen in the PFC. It is therefore different for different PFCs. Combining eqs. 1 and 2

$$R_1 = R_{1d} + pO_2 * R_{1p} / k \quad (3)$$

Thus, the plot of  $R_1$  vs.  $pO_2$  at a given temperature should be linear, with an intercept of  $R_{1d}$  and a slope of  $R_{1p}/k$ .  $R_{1d}$  is the anoxic relaxation rate, *i.e.*, the relaxation rate in absence of oxygen, and  $R_{1p}$  is the relaxation rate due to the paramagnetic contribution of oxygen dissolved in the solution or tissue.

### 3.2. Diamagnetic contributions to $R_1$

The diamagnetic contribution  $R_{1d}$  to the total relaxation rate of PFCs generally results from a combination of  $^{19}F$ - $^{19}F$  dipole-dipole (DD) interactions and  $^{19}F$  chemical-shift anisotropy (CSA) at high magnetic fields. When molecular motions are in the extreme narrowing region the DD contribution to  $R_{1d}$  ( $R_{1DD}$ ) is independent of the magnetic-field strength (86), but the CSA contribution to  $R_{1d}$  ( $R_{1CSA}$ ) varies directly as the square of the magnetic-field strength (87). Thus, at relatively low magnetic fields, the CSA contribution to relaxation is negligible, while at high

magnetic fields it is comparable to the contribution of DD interactions. In general, we can treat DD and CSA interactions as independent and additive contributions to  $R_{1d}$ , but they can be correlated in some cases. DD and CSA interactions within a  $CF_2$  or  $CF_3$  group can interfere with each other because they both are fixed to the same physical structure and this correlation can cause the relaxation curve to be multi exponential by introducing a slow relaxing component (88-90) in some cases. Generally such effects on  $R_{1d}$  are negligible. Any inter-molecular DD contribution can be assimilated into the intramolecular DD contribution and represented by an effective  $^{19}F$ - $^{19}F$  distance  $r_{FF}$ . An exact expression for the DD and CSA relaxation times depends on the structure and the molecular dynamics of the functional group under consideration (*i.e.*,  $CF_3$ ,  $CF_2$ , or  $CF$ ) and can be quite complicated. Some knowledge of the molecular dynamics may allow assumptions to compute an exact expression, which can then be compared with experimental observations. For example, internal rotation of the  $CF_2$  groups in a linear chain PFC may be sterically hindered and considered to be fixed motionless in a rigid sphere that undergoes isotropic rotational diffusion. For the terminal  $CF_3$  group, reorientation results from the same isotropic rotational diffusion of the rigid sphere and random internal  $120^\circ$  jumps about the three-fold symmetry axis fixed in the sphere. It is reasonable to assume that the principle component of the chemical shift tensor lies along the C-F bond and one can use chemical-shielding anisotropy ( $\Delta\sigma$ ) and asymmetry ( $\eta_\sigma$ ) values from literature. Such internal motion will lead to extra terms and the angular dependence in the equations for the  $CF_3$  group compared to the  $CF_2$  group. Shukla *et al.* (91) calculated the DD and CSA relaxation rates for the  $CF_2$  and  $CF_3$  groups of perfluorotributylamine (PFTB) and compared theory with experimental measurements of  $R_{1a}$  ( $= R_{1DD} + R_{1CSA}$ ). For the  $CF_2$  group,

$$R_{1DD} = \frac{(N-1)3\gamma^4\hbar^2}{10r_{FF}^6} [j_1(\omega_0) + 4j_2(2\omega_0)] \quad (4)$$

$$R_{1CSA} = \frac{2(\gamma B_0 \Delta\sigma)^2}{15} \left(1 + \frac{\eta_\sigma^2}{3}\right) j_1(\omega_0) \quad (5)$$

while for the  $CF_3$  groups,

$$R_{1DD} = \frac{(N-1)3\gamma^4\hbar^2}{10r_{FF}^6} \times \left\{ \left[ \frac{1}{4} (3\cos^2\Delta_{DD} - 1)^2 \right] [j_1(\omega_0) + 4j_2(2\omega_0)] + \left[ 1 - \frac{1}{4} (3\cos^2\Delta_{DD} - 1)^2 \right] [j_{1j}(\omega_0) + 4j_{2j}(2\omega_0)] \right\} \quad (6)$$

$$R_{1CSA} = \frac{2(\gamma B_0 \Delta\sigma)^2}{15} \left(1 + \frac{\eta_\sigma^2}{3}\right) \left\{ \left[ \frac{1}{4} (3\cos^2\Delta_{CSA} - 1)^2 \right] j_1(\omega_0) + \left[ 1 - \frac{1}{4} (3\cos^2\Delta_{CSA} - 1)^2 \right] j_{1j}(\omega_0) \right\} \quad (7)$$

where N is the number of  $^{19}F$  nuclei in the group (2 for  $CF_2$  and 3 for  $CF_3$ ),  $\gamma$  is the gyromagnetic ratio of  $^{19}F$ ,  $B_0$  is the spectrometer magnetic-field strength and  $\omega_0$  is the corresponding  $^{19}F$  Larmor frequency ( $= \gamma B_0$ ).  $\Delta_{DD}$  is the angle between the F-F vector and the internal rotation axis and  $\Delta_{CSA}$  is the angle between the principle axis of the chemical-shift tensor and the internal rotation axis. The spectral density functions  $j_n(n\omega_0)$  and  $j_{nj}(n\omega_0)$  are related to the correlation times of isotropic rotational diffusion of the molecule ( $\tau_c$ ) and internal rotation of the  $CF_3$  group around the symmetry axis ( $\tau_{ci}$ ), respectively, by

$$j_n(n\omega_0) = \frac{\tau_c}{1 + (n\omega_0\tau_c)^2} \quad (8)$$

$$j_{nj}(n\omega_0) = \frac{\tau_{ci}}{1 + (n\omega_0\tau_{ci})^2} \quad (9)$$

where

$$1/\tau_{ci} = 1/\tau_c + 1/\tau_{ci} \quad (10)$$

Assuming that all bond angles for the  $CF_3$  groups are tetrahedral ( $\Delta_{DD}=90^\circ$ ,  $\Delta_{CSA}=71^\circ$ ), eqns. 6 and 7 reduce to

$$R_{1DD} = \frac{3\gamma^4\hbar^2}{5r_{FF}^6} \times \{0.25[j_1(\omega_0) + 4j_2(2\omega_0)] + 0.75[j_{1j}(\omega_0) + 4j_{2j}(2\omega_0)]\} \quad (11)$$

$$R_{1CSA} = \frac{2(\gamma B_0 \Delta\sigma)^2}{15} \left(1 + \frac{\eta_\sigma^2}{3}\right) \{0.11j_1(\omega_0) + 0.89j_{1j}(\omega_0)\} \quad (12)$$

In the motional narrowing limit  $j_n(n\omega_0) \rightarrow \tau_c$  and  $j_{nj}(n\omega_0) \rightarrow \tau_{ci}$ , and further simplification of the above equations is possible. The relative contributions of DD and CSA to  $R_{1d}$  can vary with temperature and magnetic field. In the case of perfluorotributylamine (PFTB),  $R_{1CSA}$  was found to be greater than  $R_{1DD}$  for  $CF_2$  groups at high fields, while  $R_{1DD}$  dominates over  $R_{1CSA}$  for the  $CF_3$  group (91). Internal molecular rotation of the  $CF_3$  group results in a greater fractional decrease in  $R_{1CSA}$  compared to the fractional decrease in  $R_{1DD}$ . From eqns. 4, 5, 11 and 12, in the limit where internal rotation is extremely fast (*i.e.*,  $\tau_{ci}, \tau_{ci} \rightarrow 0$ ),  $R_{1DD}(CF_3) = R_{1DD}(CF_2)/2$  and  $R_{1CSA}(CF_3) = R_{1CSA}(CF_2)/9$ .

The anoxic contribution to the relaxation rate,  $R_{1d}$ , represents the lower limit of  $R_1$  with respect to  $pO_2$  reporter molecules. Accurate determination is essential for calibration, as it represents "0 torr". In the case of a molecule like hexafluorobenzene (HFB), the expression for  $R_{1DD}$  will be similar to eqn. 4. However, three different F-F distances must be taken into account. Each F nucleus has two ortho ( $r_{FF} \sim 2.91\text{\AA}$ ), two meta ( $r_{FF} \sim 5.04\text{\AA}$ ) and one para ( $r_{FF} \sim 5.82\text{\AA}$ ) F neighbors and the total  $R_{1DD}$  will be a sum of these three components. Due to the strong  $1/r_{FF}^6$  dependence, the para and the meta contributions may be small (1/27 and 1/128 of the ortho

## MR Oximetry

contribution, respectively, accounting for the distances and number of atoms), but this has not been verified. Compared to CF<sub>3</sub> (r<sub>FF</sub> ~2.41Å) and CF<sub>2</sub> (r<sub>FF</sub> ~2.38Å) groups the closest FF distance in HFB is larger, and hence, one might expect R<sub>1DD</sub> to be smaller. Indeed, the anoxic relaxation rate of HFB (~0.08 s<sup>-1</sup>) is smaller than those of the α-CF<sub>2</sub> (~1.35 s<sup>-1</sup>) and CF<sub>3</sub> (~0.88 s<sup>-1</sup>) resonances in PFTB (91, 92). Of course, the differences in R<sub>1d</sub> for different perfluorocarbons cannot be accounted for by considering the F-F distances only; molecular dynamics and CSA contributions play a major role as well.

### 3.3. Paramagnetic contribution of oxygen

The presence of dissolved oxygen affects the chemical shift as well as the relaxation rates of the PFC molecules in their vicinity. The measured paramagnetic chemical shift, Δσ<sub>p</sub>, in presence of oxygen results from a Fermi contact interaction between molecular oxygen and PFC nuclei and is given by (86, 93)

$$\Delta\sigma_p = \frac{Axn_M hS(S+1)\gamma^2 g_e^2 \beta_e^2}{g_N^2 \beta_N^2 kT} \quad (13)$$

where A is the hyperfine constant, x is the mole fraction of oxygen, n<sub>M</sub> is the number of PFC molecules surrounding an oxygen molecule, h and k are Planck and Boltzmann constants, γ is the nuclear gyromagnetic ratio, g<sub>e</sub>β<sub>e</sub> and g<sub>N</sub>β<sub>N</sub> are the electron and nuclear magnetic moments, S is the total electron spin of the paramagnetic species (S = 1 for O<sub>2</sub>), and T is the absolute temperature. Using eqns. 2 and 13 one could try to measure pO<sub>2</sub> from the chemical shift using a predetermined calibration curve. However, Δσ<sub>p</sub> is usually small and is superimposed upon chemical shifts induced by changes in bulk magnetic susceptibility due to the presence of oxygen. Separating the two effects would require the ability to apply B<sub>0</sub> perpendicular, as well as parallel to the sample(93). For *in vivo* imaging, shimming could also affect the measurement of Δσ<sub>p</sub> and this method has not been used to measure pO<sub>2</sub>.

The presence of any dissolved oxygen results in a paramagnetic contribution, R<sub>1p</sub>, which is given by (93, 94)

$$R_{1p} = \frac{2S(S+1)\gamma^2 g^2 \beta^2}{15r^6} \left[ \frac{3\tau_c}{1 + \omega_I^2 \tau_c^2} + \frac{7\tau_c}{1 + \omega_S^2 \tau_c^2} \right] \quad (14)$$

where r is the distance between the paramagnetic center and the nucleus concerned, ω<sub>S</sub> is the angular frequency of electron resonance, and ω<sub>I</sub> is the angular frequency of nuclear resonance. Here, we ignore the contribution due to contact interaction as oxygen does not form a complex with the PFCs, and hence the hyperfine interaction would be very small. The correlation time for the reorientation of the coupled magnetic moment vectors, τ<sub>c</sub>, is given by

$$1/\tau_c = 1/\tau_s + 1/\tau_r + 1/\tau_e \quad (15)$$

where τ<sub>s</sub> is the electron spin relaxation time, τ<sub>r</sub> is the rotational correlation time, and τ<sub>e</sub> is the residence time of

the paramagnetic species. In the motional narrowing limit, ω<sub>S</sub>τ<sub>c</sub> << 1 and ω<sub>S</sub>τ<sub>c</sub> << 1 so eqn. 11 simplifies to

$$R_{1p} = \frac{8\gamma^2 g^2 \beta^2 \tau_c}{3r^6} \quad (16) \text{ for } S=1.$$

R<sub>1p</sub> determines the sensitivity of the PFC spin lattice relaxation rate to the presence of oxygen. PFCs with multiple <sup>19</sup>F atoms (with unique chemical shifts) generally exhibit a different R<sub>1</sub> response of each resonance to pO<sub>2</sub> (*i.e.*, different slopes on an R<sub>1</sub> vs. pO<sub>2</sub> graph). These differences are a result of the inverse dependence of R<sub>1p</sub> on r<sup>6</sup> and imply that oxygen has a preferred approach to each PFC molecule. If the average distances between the oxygen molecule and various fluorine atoms in a PFC are different, R<sub>1p</sub> would be larger for the fluorine nuclei that are closer to the oxygen molecule. Effective spin diffusion within the molecule can lead to the reduction of differences in the slopes. The preferences of the approach of oxygen to different parts of the PFCs are most likely due to steric factors rather than specific binding as formation of complexes or preferential binding would manifest itself as a very high R<sub>1</sub> of a particular fluorine atom compared to its neighbors. The oxygen molecule may prefer to approach the ends of the PFCs simply because there is more space available at the ends than in the bridgehead positions or the middle of a chain. This is clearly seen by comparing the slopes of different fluorine atoms of the cis and trans isomers of perfluorodecalin (PFD) (94). In the case of trans-perfluorodecalin, the larger difference in oxygen access to the end chain fluorine atoms compared to bridgehead fluorine atoms leads to a larger variability in the slopes compared to cis-perfluorodecalin. The slope does not vary greatly between terminal CF<sub>3</sub> groups of perfluorotributylamine (PFTB), perfluorotripropylamine (PFTP) and perfluorooctyl bromide (PFOB or perflubron) (91), and thus, relative pO<sub>2</sub> sensitivity of this resonance is determined by R<sub>1d</sub>, which is different in all three cases. The CF<sub>2</sub> resonances from these PFCs show high sensitivity to temperature within the temperature range 5-50 °C. The terminal trifluoromethyl groups have greater sensitivity to oxygen and lower sensitivity to temperature (compared to CF<sub>2</sub> groups). The CF<sub>3</sub> resonance of PFOB exhibits greater sensitivity to pO<sub>2</sub> than PFTB or PFTP. Internal motion also aids R<sub>1p</sub>, and hence pO<sub>2</sub> sensitivity. For example, the bulky CF<sub>2</sub>Br group of PFOB is less sensitive to pO<sub>2</sub> than the CF<sub>3</sub> group on the other end of the molecule.

In general, each contribution (R<sub>1d</sub> and R<sub>1p</sub>) to R<sub>1</sub> is temperature dependent at a given field and exhibits a maximum at a temperature at which the inverse of corresponding correlation time matches the Larmor frequency. The constant k, which represents the oxygen solubility of the PFC, is also temperature dependent. On increasing the temperature, oxygen solubility in the PFC decreases and both R<sub>1p</sub> and R<sub>1d</sub> decrease for liquids in the motional narrowing regime (ω<sub>0</sub>τ<sub>c</sub> << 1). The temperature dependence of these relaxation rates can reveal information of the molecular dynamics that dominate these relaxation processes. In case of both anoxic and oxidic PFTB the R<sub>1</sub> maxima were observed to occur at similar temperatures (91). This implies that in this case the τ<sub>c</sub> that

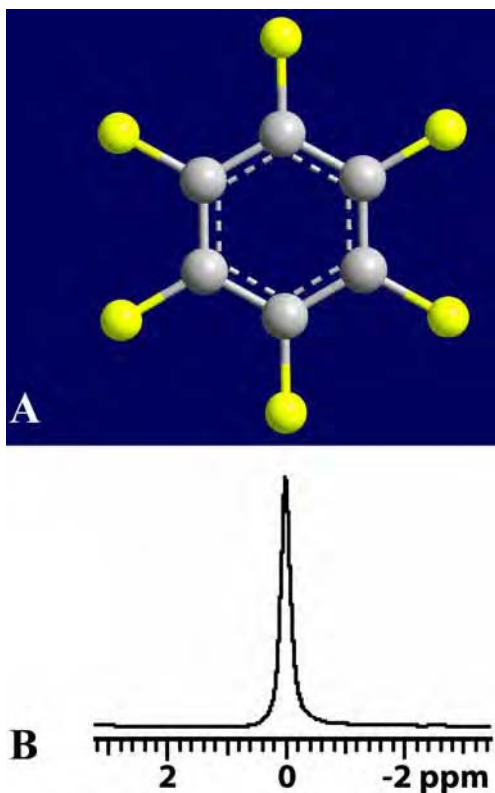


**Figure 1.** (a) Hexafluorobenzene and (b) its  $^{19}\text{F}$  NMR spectrum.

determine  $R_{1p}$  and  $R_{1d}$  are approximately equal. Therefore, the residence time of an oxygen molecule near a given PFTB molecule may be comparable to the molecular rotational correlation time of PFTB. This represents a strong influence of residence time on  $R_{1p}$ , possibly as important as the inter-nuclear fluorine-oxygen distance.

### 3.4. Measuring $p\text{O}_2$

Although there is no theoretical reason to expect linearity in  $R_{1d}$  and  $R_{1p}$  with temperature, a linear approximation can be made for  $R_{1d}$  and  $R_{1p}/k$  from a purely practical standpoint within the biologically relevant temperature range (*e.g.*, 30-42 °C). If the respective relaxation rate maxima occur in the middle of this range, the slope and intercept may “appear” to be temperature independent). For characterizing the  $p\text{O}_2$  and temperature dependence, the neat PFC or emulsion is typically placed in gas-tight NMR glass tubes, saturated by bubbling for 20-30 minutes with a range of standard gases (*e.g.*, 0%, 5%, 10%, 21% and 100 %  $\text{O}_2$  -balance  $\text{N}_2$ ) and sealed. Each sealed tube is inserted in a circulating water bath and the  $T_1$  is measured as a function of temperature. The data at each temperature is fit to eqn. 3

$$R_1 [\text{s}^{-1}] = A' + B' * p\text{O}_2 \quad (12)$$

where  $A'$  ( $=R_{1d}$ ) and  $B'$  ( $=R_{1p}/k$ ) are constants at a given temperature. If we assume a linear dependence of  $A'$  and

$B'$  on temperature  $T$ , then  $A' = A + C * T$  and  $B' = B + D * T$ , giving a temperature-dependent model (95):

$$R_1 [\text{s}^{-1}] = A + B * p\text{O}_2 + C * T + D * p\text{O}_2 * T \quad (13)$$

where  $A$ ,  $B$ ,  $C$  and  $D$  are constants. For PFCs with multiple resonances these constants are usually different for each resonance, discussed earlier. For such PFCs  $p\text{O}_2$  and temperature can be estimated simultaneously by solving two simultaneous equations (corresponding to eqn. 13 for 2 resonances) using the measured values of  $R_1$  for each resonance (95). In graphical terms, in a 3-dimensional variable space ( $R_1 = f(p\text{O}_2, T)$ ) the ordinates corresponding to the intersection of  $R_1$  iso-contours of the two resonances are  $p\text{O}_2$  and  $T$ , respectively. Multi resonance PFC spectra can provide multiple estimates of  $p\text{O}_2$ , if temperature is known, or  $p\text{O}_2$  and temperature by solving simultaneous equations, as needed.

For imaging, multiple resonances could lead to chemical shift artifacts or reduced signal-to-noise following selective excitation or editing (96, 97). In practice, a PFC such as hexafluorobenzene (HFB) with a single resonance (Figure 1 a, b), high  $p\text{O}_2$  sensitivity and minimal temperature sensitivity is preferable (75). Perfluoro-15-crown-5-ether (15-C-5) also has quite similar characteristics, and shorter absolute  $T_1$ s making data acquisition potentially faster, but a higher  $R_1$  sensitivity to temperature and it is less readily available (9, 74). While a smaller  $A'$  value represents greater sensitivity, it also implies that the PFC has longer  $T_1$  values (smaller  $R_1$ ) under hypoxic conditions, where  $R_1$  may be close to  $A'$ . Indeed, the  $T_1$  of HFB at 4.7 T may reach 12 s, limiting the current temporal resolution of  $p\text{O}_2$  measurements using HFB to 6 ½ min (98). However, use of echo planar imaging as in the *FREEDOM* (Fluorocarbon Relaxometry using Echo planar imaging for Dynamic Oxygen Mapping) approach allows images, and hence, spatially resolved oxygen distributions to be acquired in the same time as spectroscopy (9). Following a direct intra-tissue injection, dynamic changes in oxygenation in response to hyperoxic intervention can be monitored *in vivo* (Figure 2). A further improvement in temporal resolution is possible by using other approaches such as those based on the Look-Locker technique (99, 100). Even then, a complete sampling of the relaxation curve would require at least 1 min ( $\sim 5 * T_1$  for HFB under hypoxic conditions). The slope  $B'$  represents the effect of oxygen and hence a greater slope is desirable for measurement accuracy. A greater slope would result in a wider separation of measured  $T_1$  values especially at low  $p\text{O}_2$  values. A high slope could result from higher  $R_{1p}$  or a smaller  $k$  (higher  $\text{O}_2$  solubility). From eqn. 2 we can see that for a given  $p\text{O}_2$ , a smaller  $k$  reflects a larger  $\text{O}_2$  mole fraction  $x$ .

The solubility of oxygen (and gases in general) in perfluorocarbons and hydrofluorocarbons is three to ten times higher than observed in the parent hydrocarbons or in water (101, 102). It was shown that a model of continuous diffusion of oxygen, that accounts for the  $T_1$  and  $T_2$  relaxation of benzene, fails in the case of HFB, leading to either impossibly short residence times for oxygen or

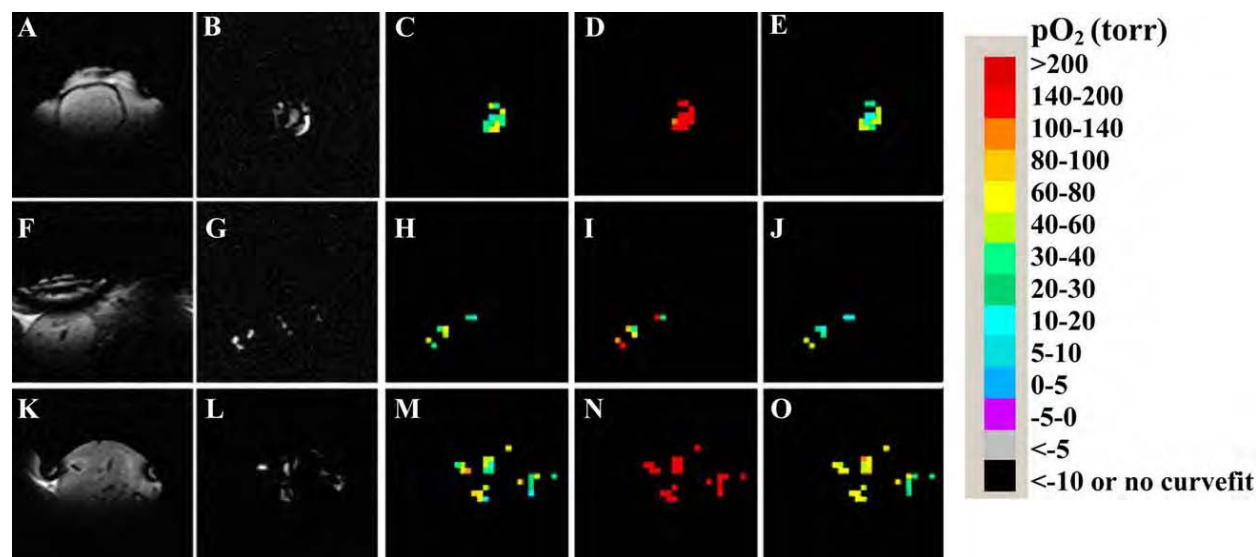


**Figure 2.** Dynamic  $^{19}\text{F}$  MR oximetry. Monitoring changes in oxygenation at locations in the brain (a-e), kidney and liver (f-j) and thigh (k-o) of Sprague Dawley rat with respect to oxygen challenge following direct intra-tissue injection of HFB (50  $\mu\text{l}$ ) at discrete locations. Spin-echo anatomical images (a,f,k), spin-echo images of hexafluorobenzene injected into the tissue (b,g,l) and the corresponding time course *FREDOM* pO<sub>2</sub> maps (c,h,m: baseline air breathing, d,i,n: 30 min oxygen and e,j,o: 30 min after return to air breathing) showing the response to hyperoxic gas intervention. Data obtained in collaboration with Dr. Mark Rollins and Dr. Lisa Wilmes of UCSF.

impossibly small distance of closest approach between fluorine and oxygen (93). The presence of the larger fluorine atoms appears to result in the existence of numerous large “vacancies” or “channels” in the liquid “lattice”, which the oxygen molecules occupy successively by random jumps. The oxygen solubility of long chained aliphatic fluorocarbons are observed to be higher than that of cyclic or aromatic fluorocarbons (102), which suggests that aliphatic chains form large channels in the liquid state, which accommodate more oxygen molecules unlike planar aromatic structures that may result in tighter “packing” with smaller vacancies. This exceptionally high solubility motivated the use of perfluorocarbons as blood substitutes for oxygen delivery to tissues (103, 104). Fluosol-DA (Green Cross Corp., Osaka, Japan) a perfluorotripropylamine based emulsion was the first PFC emulsion clinically tested and approved for clinical use as perfusate for percutaneous coronary angioplasty, but was later withdrawn from the market because of low oxygen delivery capacity under physiologic conditions, lack of clear clinical benefit and development of flow-through catheters (105-108). More recently, Oxygent<sup>TM</sup> (Alliance Corp., San Diego, CA), an emulsion of perfluorooctyl bromide (perflubron) with a higher oxygen solubility and improved emulsion stability has been tested in clinical trials (109, 110). In terms of *in vivo* oximetry, due to their high oxygen solubility and hydrophobicity, PFCs essentially act as molecular amplifiers by displaying extra sensitivity to oxygen and insensitivity to variations in ionic constituents compared to the surrounding tissue water.

$^{19}\text{F}$  MR based oximetry has several strengths and a few weaknesses. The nuclear spin  $\frac{1}{2}$   $^{19}\text{F}$  nucleus has  $\gamma$  of

40.05 MHz/T (compared to 42.58 MHz/T for  $^1\text{H}$ ) and about 83% NMR sensitivity compared to  $^1\text{H}$ . It is 100 % abundant (isotopically) and the amount of endogenous fluorine in the body is very small (mostly present in form of solid fluorides in bones and teeth). Due to a very short T<sub>2</sub> relaxation time, the NMR signal from endogenous fluorine is undetectable in most biological systems. Given the absence of background signals, the exogenously administered PFC is readily observed.  $^{19}\text{F}$  MR oximetry has been used as a research tool for many years (9, 74, 75, 84, 85, 98, 111-136). However, to date the method has not been translated to the routine clinical setting, since most clinical MRI scanners lack a  $^{19}\text{F}$  capability. PFCs have been observed in patients following administration as adjuvant to radiotherapy and as residues in the eye, where they are used as tamponades during retinal surgery (127, 137, 138). A  $^1\text{H}$  pO<sub>2</sub> reporter molecule could have greater immediate applicability and higher potential for clinical translation.

### 3.5. New development: $^1\text{H}$ MRI based oximetry using hexamethyldisiloxane

The  $^1\text{H}$  R<sub>1</sub> of tissue water has been shown to be sensitive to tissue oxygenation (139), but many other factors like metal ions, cellularity, pH, ionic strength can also affect relaxation of tissue water. This makes quantitative measurements impossible except in tissues such as the vitreous humor in the eye and cerebrospinal fluid, where ionic and protein content is low or known and constant (140-143). Even then, R<sub>1</sub> sensitivity to oxygen is low (B' = 0.0002 s<sup>-1</sup>/torr) and to temperature is high. We have recently identified hexamethyldisiloxane (HMDSO, Figure 3) as a  $^1\text{H}$  NMR probe of pO<sub>2</sub> (analogous to PFCs) and shown the feasibility of tissue oximetry using  $^1\text{H}$ -NMR spectroscopic relaxometry (83). We have also implemented

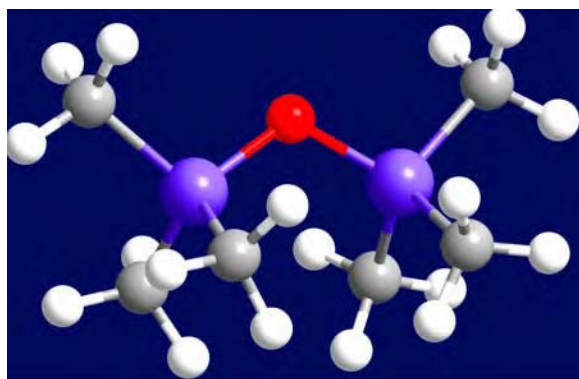


Figure 3. Structure of hexamethyldisiloxane (HMDSO).

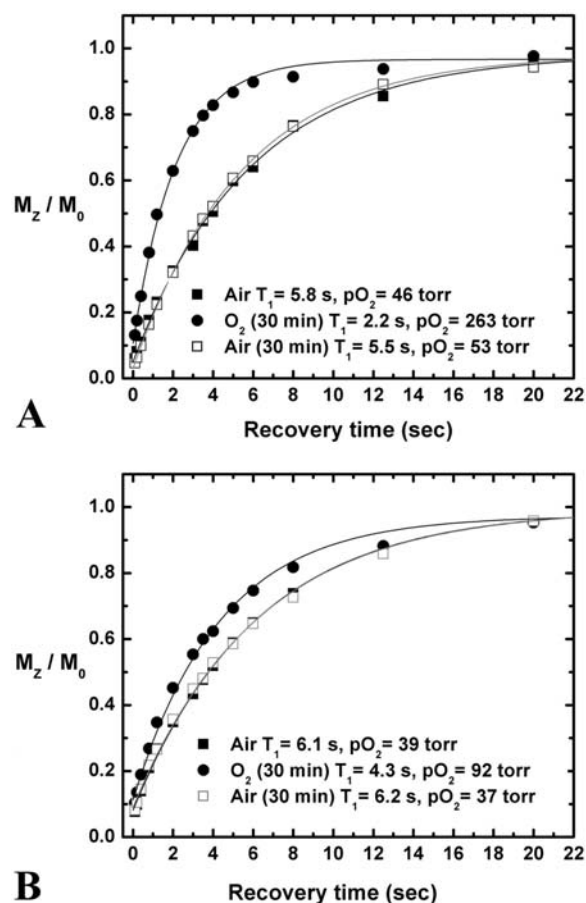


Figure 4. Dynamic  $^1\text{H}$  oximetry. HMDSO magnetization recovery curves *in vivo* in response to hyperoxic challenge following direct intra-tissue injection of HMDSO (50  $\mu\text{l}$ ) at discrete locations. Chemical shift selective spectroscopy with suppression of fat and water signals permitted relaxometry of HMDSO. On switching breathing gas from air ( $\blacksquare$ ) to oxygen for 30 min ( $\bullet$ ) a larger change in  $T_1$  (corresponding to a larger change in  $pO_2$ ) is observed in thigh muscle (a) compared to AT1 prostate tumor (b) which is reversed in both cases by switching back to air breathing ( $\square$ ).

an imaging based method: Proton Imaging of Silanes to map Tissue Oxygenation Levels (PISTOL) for spatial mapping of  $pO_2$  (144).

HMDSO is a symmetric molecule with a single NMR signal close to that of the chemical shift standard tetramethylsilane (TMS) (83). It is therefore well separated from water and reasonably separated from fat. HMDSO has many characteristics similar to PFCs: it is a highly hydrophobic mobile liquid, non-toxic, with high gas solubility and is readily available and cheap. At a given temperature,  $R_1$  of HMDSO showed a linear dependence on  $pO_2$ , with constants  $A' = 0.1126 \pm 0.0010[\text{s}^{-1}]$  and  $B' = 0.00130 \pm 0.00002 [(\text{torr}\cdot\text{s})^{-1}]$  at  $37^\circ\text{C}$ . The  $T_1$  values range from 8.7 s ( $pO_2 = 0$  torr) to 1 s ( $pO_2 = 760$  torr) at  $37^\circ\text{C}$ . A small temperature dependence was observed in the temperature range 26–46  $^\circ\text{C}$ . Fitting the calibration data to the temperature-dependant model (eqn. 13) yielded constants  $A = 0.1479 \pm 0.0028 \text{ s}^{-1}$ ,  $B = (1.79 \pm 0.05) \times 10^{-3} (\text{s torr})^{-1}$ ,  $C = (-9.57 \pm 0.81) \times 10^{-4} (\text{s }^\circ\text{C})^{-1}$ , and  $D = (-1.23 \pm 0.13) \times 10^{-5} (\text{s torr }^\circ\text{C})^{-1}$ . In this temperature range, linear approximation resulted in errors  $< 3\%$ . The  $pO_2$  and temperature sensitivities of HMDSO are similar to 15-C-5.

Using a spectroscopic approach,  $pO_2$  was measured in rat thigh muscle and Dunning prostate R3327 AT1 adenocarcinomas in response to an oxygen challenge (83). Changes in relaxation times in response to hyperoxia and differential response in tumor versus healthy thigh muscle can be easily seen from the HMDSO magnetization recovery curves (Figure 4). Clearance of HMDSO from muscle was seen to be slow with a half-life  $\sim 35$  h, so that minimal change would be observed during typical MR studies of oxygen dynamics in response to acute interventions. HMDSO is quite inert and it has been reported that no treatment-related signs of toxicity or mortality or other statistically significant deleterious effects were noted in studies where Fisher rats were exposed to up to 6000 ppm HMDSO by inhalation (145, 146).

Like PFCs, HMDSO is lipophilic and is essentially immiscible in aqueous solutions. The boiling point and hydrophobicity of HMDSO suggest that it could be emulsified for intravenous delivery, as popular for several PFCs (147) and such an attempt is currently underway. HMDSO is readily and cheaply available from many commercial vendors and easy to store. One key difference in this  $^1\text{H}$  MR approach compared to  $^{19}\text{F}$  oximetry is the need to effectively suppress water and fat signals and perform relaxometry on the silane signal. In PISTOL, we have developed an effective approach using a combination of frequency selective excitation of the silane resonance and CHES (148) suppression of the water and fat resonances is used followed by EPI detection for measuring  $T_1$  values (144). As with HFB, ARDVARC (Alternating Relaxation Delays with Variable Acquisitions for Reduction of Clearance effects) protocol (98) is used in conjunction with this sequence to obtain  $T_1$  values.

#### 4. PERSPECTIVE AND CONCLUSION

An important advantage of MR oximetry compared to hypoxia imaging using nuclear and optical imaging agents is that one can quantitatively measure tissue  $pO_2$  as opposed to qualitatively labeling hypoxic regions. Thus issues such as hypoxia specificity, oxygen dependency of agent binding and clearance of unbound agents do not come into play and affect interpretation. Dynamic measurements with transient interventions such as hyperoxia (9) or acute effects of vascular targeting (149) are not possible with nuclear and optical techniques. Optical imaging methods to image hypoxia to date rely on transfection to express bioluminescent (45, 47) or fluorescent proteins (44, 46) and are thus inappropriate for clinical application. In any case light penetration in tissue would be a problem for human use.

MR oximetry has found extensive use in pre clinical studies because it provides essentially unique insight into tissue oxygenation- specifically spatial and temporal resolution revealing heterogeneity and dynamic response to intervention. Moreover, precision achieved is appropriate for radiobiological studies of tumors. To date  $^{19}F$  NMR approaches have been used to examine vascular oxygenation following i.v. administration of PFC emulsion or tissue oxygenation following vascular clearance and sequestration in tissue. However, accumulation occurs predominantly in tumor periphery biasing measurements towards well-perfused regions. Moreover, there is substantial uptake by the reticuloendothelial system (RES). While this allows effective measurements of  $pO_2$  in liver, spleen and bone marrow, it is less satisfactory for oncological investigations. An alternate approach is direct injection of the reporter molecule into the tissue of interest. The possibility of targeting emulsion to specific antigens such fibrin for cardiovascular imaging opens further possibilities (150).

The development of PISTOL, a quantitative  $^1H$  MR method for dynamic imaging of  $pO_2$  opens further opportunities for *in vivo* studies. This method has a high potential of translation to the clinical setting. With current state-of-the-art MR hardware, it would be easy to generate effective water and fat suppression needed for PISTOL as used in detection of metabolites by Magnetic Resonance Spectroscopy (MRS). In both the research and clinical setting, it will now be possible to add quantitative oximetry to a protocol consisting of other  $^1H$ -MR based functional techniques such as dynamic contrast enhancement, diffusion measurements, and MRS, but the minimal invasiveness of the technique has to be taken into account. Development of targeted nano-emulsions for intravenous delivery might help circumvent the need for direct intra-tissue injections, if high targeting specificity is achieved. Other  $^1H$   $pO_2$  reporter molecules could be identified or synthesized, which could have higher oxygen sensitivity than HMDSO. We foresee MR oximetry as a valuable tool for assessing tissue oxygenation status in various disease states, helping to evaluate the acute and chronic response of therapeutic interventions and aiding in the screening of new

drugs, such as vascular targeting and anti angiogenic agents which can perturb tissue oxygenation.

#### 5. ACKNOWLEDGMENTS

Investigations discussed here have been supported by the Texas Affiliate of the American Heart Association, the Whitaker Foundation, the American Cancer Society, the Department of Defense Breast and Prostate Cancer Initiatives and the National Institute of Health. Most recent funding is from the NCI SAIRP U24 CA126608 and the work in Figure 2 was supported by the Foundation for Anesthesia Education and Research.

#### 6. REFERENCES

1. Tatum, J. L., G. J. Kelloff, R. J. Gillies, J. M. Arbeit, J. M. Brown, K. S. Chao, J. D. Chapman, W. C. Eckelman, A. W. Fyles, A. J. Giaccia, R. P. Hill, C. J. Koch, M. C. Krishna, K. A. Krohn, J. S. Lewis, R. P. Mason, G. Melillo, A. R. Padhani, G. Powis, J. G. Rajendran, R. Reba, S. P. Robinson, G. L. Semenza, H. M. Swartz, P. Vaupel, D. Yang, B. Croft, J. Hoffman, G. Liu, H. Stone & D. Sullivan: Hypoxia: importance in tumor biology, noninvasive measurement by imaging, and value of its measurement in the management of cancer therapy. *Int J Radiat Biol*, 82, 699-757 (2006)
2. Okunieff, P., B. Fenton & Y. Chen: Past, present, and future of oxygen in cancer research. *Adv Exp Med Biol*, 566, 213-22 (2005)
3. Poli, G., G. Leonarduzzi, F. Biasi & E. Chiarotto: Oxidative stress and cell signalling. *Curr Med Chem*, 11, 1163-82 (2004)
4. Bergamini, C. M., S. Gambetti, A. Dondi & C. Cervellati: Oxygen, reactive oxygen species and tissue damage. *Curr Pharm Des*, 10, 1611-26 (2004)
5. Brizel, D. M., G. S. Sibly, L. R. Prossnitz, R. L. Scher & M. W. Dewhirst: Tumor hypoxia adversely affects the prognosis of carcinoma of the head and neck. *Int. J. Radiat. Oncol. Biol. Phys.*, 38, 285-289 (1997)
6. Rofstad, E. K., K. Sundfor, H. Lyng & C. G. Trope: Hypoxia-induced treatment failure in advanced squamous cell carcinoma of the uterine cervix is primarily due to hypoxia-induced radiation resistance rather than hypoxia-induced metastasis. *Br. J. Cancer*, 83, 354-9 (2000)
7. Fyles, A., M. Milosevic, D. Hedley, M. Pintilie, W. Levin, L. Manchul & R. P. Hill: Tumor hypoxia has independent predictor impact only in patients with node-negative cervix cancer. *J Clin Oncol*, 20, 680-7 (2002)
8. Fyles, A., M. Milosevic, M. Pintilie, A. Syed, W. Levin, L. Manchul & R. P. Hill: Long-term performance of interstitial fluid pressure and hypoxia as prognostic factors in cervix cancer. *Radiother Oncol*, 80, 132-7 (2006)
9. Zhao, D., L. Jiang & R. P. Mason: Measuring changes in tumor oxygenation. *Methods Enzymol*, 386, 378-418 (2004)
10. Swartz, H. M. & J. F. Dunn: Measurements of oxygen in tissues: overview and perspectives on methods. In: Oxygen Transport to Tissue XXIV. Eds: J. F. Dunn & H. M. Swartz. Kluwer Academic, New York (2003)
11. Stone, H. B., J. M. Brown, T. Phillips & R. M. Sutherland: Oxygen in human tumors: correlations between

- methods of measurement and response to therapy. *Radiat Res.*, 136, 422-434 (1993)
12. Vaupel, P., K. Schlenger, C. Knoop & M. Hockel: Oxygenation of human tumors: evaluation of tissue oxygen distribution in breast cancers by computerized O<sub>2</sub> tension measurements. *Cancer Res*, 51, 3316-22 (1991)
  13. Cater, D. B. & I. A. Silver: Quantitative measurements of oxygen tension in normal tissues and in the tumours of patients before and after radiotherapy. *Acta radiol*, 53, 233-56 (1960)
  14. Crawford, D. W. & M. A. Cole: Performance evaluation of recessed microcathodes: criteria for tissue pO<sub>2</sub> measurement. *J Appl Physiol*, 58, 1400-5 (1985)
  15. Nozue, M., I. Lee, F. Yuan, B. A. Teicher, D. M. Brizel, M. W. Dewhirst, C. G. Milross, L. Milas, C. W. Song, C. D. Thomas, M. Guichard, S. M. Evans, C. J. Koch, E. M. Lord, R. K. Jain & H. D. Suit: Interlaboratory variation in oxygen tension measurement by Eppendorf "Histogram" and comparison with hypoxic marker. *J Surg Oncol*, 66, 30-8 (1997)
  16. Brizel, D. M., S. P. Scully, J. M. Harrelson, L. J. Layfield, J. M. Bean, L. R. Prosnitz & M. W. Dewhirst: Tumor oxygenation predicts for the likelihood of distant metastases in human soft tissue sarcoma. *Cancer Res.*, 56, 941-3 (1996)
  17. Movsas, B., J. D. Chapman, E. M. Horwitz, W. H. Pinover, R. E. Greenberg, A. L. Hanlon, R. Iyer & G. E. Hanks: Hypoxic regions exist in human prostate carcinoma. *Urology*, 53, 11-8 (1999)
  18. Rudat, V., B. Vanselow, P. Wollensack, C. Bettscheider, S. Osman-Ahmet, M. J. Eble & A. Dietz: Repeatability and prognostic impact of the pretreatment pO<sub>2</sub> histography in patients with advanced head and neck cancer. *Radiother Oncol*, 57, 31-7 (2000)
  19. Aquino-Parsons, C., A. Green & A. I. Minchinton: Oxygen tension in primary gynaecological tumours: the influence of carbon dioxide concentration. *Radiother Oncol*, 57, 45-51 (2000)
  20. Griffiths, J. R. & S. P. Robinson: The OxyLite: a fibre-optic oxygen sensor. *British Journal of Radiology*, 72, 627-630 (1999)
  21. Bussink, J., J. H. A. M. Kaanders, A. M. Strik, B. Vojnovic & A. J. van der Kogel: Optical sensor-based oxygen tension measurements correspond with hypoxia marker binding in three human tumor xenograft lines. *Radiation Research*, 154, 547-555 (2000)
  22. Mason, R. P., D. Zhao, A. Constantinescu & A. Obeid: Tumor oximetry: comparison of <sup>19</sup>F MR EPI (FREEDOM) and the fiber-optic OxyLite™. *Proc Intl Soc Magn Reson Med*, 8, 1040 (2000)
  23. Braun, R. D., J. L. Lanzen, S. A. Snyder & M. W. Dewhirst: Comparison of tumor and normal tissue oxygen tension measurements using OxyLite or microelectrodes in rodents. *Am J Physiol Heart Circ Physiol*, 280, H2533-44 (2001)
  24. Seddon, B. M., D. J. Honess, B. Vojnovic, G. M. Tozer & P. Workman: Measurement of tumor oxygenation: *in vivo* comparison of a luminescence fiber-optic sensor and a polarographic electrode in the p22 tumor. *Radiat Res*, 155, 837-46 (2001)
  25. Jarm, T., G. Sersa & D. Miklavcic: Oxygenation and blood flow in tumors treated with hydralazine: evaluation with a novel luminescence-based fiber-optic sensor. *Technol Health Care*, 10, 363-80 (2002)
  26. Urano, M., Y. Chen, J. Humm, J. A. Koutcher, P. Zanzonico & C. Ling: Measurements of tumor tissue oxygen tension using a time-resolved luminescence-based optical oxylite probe: comparison with a paired survival assay. *Radiat Res*, 158, 167-73 (2002)
  27. Gu, Y. Q., V. A. Bourke, J. G. Kim, A. Constantinescu, R. P. Mason & H. L. Liu: Dynamic response of breast tumor oxygenation to hyperoxic respiratory challenge monitored with three oxygen-sensitive parameters. *Applied Optics*, 42, 2960-2967 (2003)
  28. Brurberg, K. G., H. K. Skogmo, B. A. Graff, D. R. Olsen & E. K. Rofstad: Fluctuations in pO<sub>2</sub> in poorly and well-oxygenated spontaneous canine tumors before and during fractionated radiation therapy. *Radiother Oncol*, 77, 220-6 (2005)
  29. Brurberg, K. G., M. Thuen, E. B. Ruud & E. K. Rofstad: Fluctuations in pO<sub>2</sub> in irradiated human melanoma xenografts. *Radiat Res*, 165, 16-25 (2006)
  30. Elas, M., K. H. Ahn, A. Parasca, E. D. Barth, D. Lee, C. Haney & H. J. Halpern: Electron paramagnetic resonance oxygen images correlate spatially and quantitatively with Oxylite oxygen measurements. *Clin Cancer Res*, 12, 4209-17 (2006)
  31. Wen, B., M. Urano, J. A. O'Donoghue & C. C. Ling: Measurements of partial oxygen pressure pO<sub>2</sub> using the OxyLite system in R3327-AT tumors under isoflurane anesthesia. *Radiat Res*, 166, 512-8 (2006)
  32. Ballinger, J. R.: Imaging hypoxia in tumors. *Semin Nucl Med*, 31, 321-9 (2001)
  33. Ljungkvist, A. S., J. Bussink, J. H. Kaanders & A. J. van der Kogel: Dynamics of tumor hypoxia measured with bioreductive hypoxic cell markers. *Radiat Res*, 167, 127-45 (2007)
  34. Maxwell, R. J., P. Workman & J. R. Griffiths: Demonstration of tumor-selective retention of fluorinated nitroimidazole probes by <sup>19</sup>F magnetic resonance spectroscopy *in vivo*. *Int J Radiat Oncol Biol Phys*, 16, 925-9 (1989)
  35. Raleigh, J. A., A. J. Franko, D. A. Kelly, L. A. Trimble & P. S. Allen: Development of an *in vivo* <sup>19</sup>F magnetic resonance method for measuring oxygen deficiency in tumors. *Magn Reson Med*, 22, 451-66 (1991)
  36. Aboagye, E. O., R. J. Maxwell, M. R. Horsman, A. D. Lewis, P. Workman, M. Tracy & J. R. Griffiths: The relationship between tumour oxygenation determined by oxygen electrode measurements and magnetic resonance spectroscopy of the fluorinated 2-nitroimidazole SR-4554. *Br J Cancer*, 77, 65-70 (1998)
  37. Jerabek, P. A., T. B. Patrick, M. R. Kilbourn, D. D. Dischino & M. J. Welch: Synthesis and biodistribution of <sup>18</sup>F-labeled fluoronitroimidazoles: potential *in vivo* markers of hypoxic tissue. *Int J Rad Appl Instrum [A]*, 37, 599-605 (1986)
  38. Rasey, J. S., Z. Grunbaum, S. Magee, N. J. Nelson, P. L. Olive, R. E. Durand & K. A. Krohn: Characterization of radiolabeled fluoromisonidazole as a probe for hypoxic cells. *Radiat Res*, 111, 292-304 (1987)
  39. Lewis, J. S., D. W. McCarthy, T. J. McCarthy, Y. Fujibayashi & M. J. Welch: Evaluation of <sup>64</sup>Cu-ATSM *in*

- vitro* and *in vivo* in a hypoxic tumor model. *J Nucl Med*, 40, 177-83 (1999)
40. Dolbier, W. R., Jr., A. R. Li, C. J. Koch, C. Y. Shiue & A. V. Kachur: [18F]-EF5, a marker for PET detection of hypoxia: synthesis of precursor and a new fluorination procedure. *Appl Radiat Isot*, 54, 73-80 (2001)
41. Mannan, R. H., V. V. Somayaji, J. Lee, J. R. Mercer, J. D. Chapman & L. I. Wiebe: Radioiodinated 1- (5-iodo-5-deoxy-beta-D-arabinofuranosyl)-2-nitroimidazole (iodoazomycin arabinoside: IAZA): a novel marker of tissue hypoxia. *J Nucl Med*, 32, 1764-70 (1991)
42. Li, L., J. M. Yu, L. G. Xing, G. R. Yang, X. D. Sun, J. Xu, H. Zhu & J. B. Yue: Hypoxic imaging with <sup>99m</sup>Tc-HL91 single photon emission computed tomography in advanced nonsmall cell lung cancer. *Chin Med J (Engl)*, 119, 1477-80 (2006)
43. Takahashi, E., T. Takano, Y. Nomura, S. Okano, O. Nakajima & M. Sato: *In vivo* oxygen imaging using green fluorescent protein. *Am J Physiol Cell Physiol*, 291, C781-7 (2006)
44. Vordermark, D., T. Shibata & J. M. Brown: Green fluorescent protein is a suitable reporter of tumor hypoxia despite an oxygen requirement for chromophore formation. *Neoplasia*, 3, 527-34 (2001)
45. Payen, E., M. Bettan, A. Henri, E. Tomkiewicz, A. Houque, I. Kuzniak, J. Zuber, D. Scherman & Y. Beuzard: Oxygen tension and a pharmacological switch in the regulation of transgene expression for gene therapy. *J Gene Med*, 3, 498-504 (2001)
46. Raman, V., D. Artemov, A. P. Pathak, P. T. Winnard, Jr., S. McNutt, A. Yudina, A. Bogdanov, Jr. & Z. M. Bhujwala: Characterizing vascular parameters in hypoxic regions: a combined magnetic resonance and optical imaging study of a human prostate cancer model. *Cancer Res*, 66, 9929-36 (2006)
47. Safran, M., W. Y. Kim, F. O'Connell, L. Flippin, V. Gunzler, J. W. Horner, R. A. Depinho & W. G. Kaelin, Jr.: Mouse model for noninvasive imaging of HIF prolyl hydroxylase activity: assessment of an oral agent that stimulates erythropoietin production. *Proc Natl Acad Sci U S A*, 103, 105-10 (2006)
48. Abramovitch, R., D. Frenkiel & M. Neeman: Analysis of subcutaneous angiogenesis by gradient echo magnetic resonance imaging. *Magn. Reson. Med.*, 39, 813-24 (1998)
49. Brasch, R. C., K. C. Li, J. E. Husband, M. T. Keogan, M. Neeman, A. R. Padhani, D. Shames & K. Turetschek: *In vivo* monitoring of tumor angiogenesis with MR imaging. [Review]. *Acad. Radiol.*, 7, 812-23 (2000)
50. Cao, Y., Z. Shen, T. L. Chenevert & J. R. Ewing: Estimate of vascular permeability and cerebral blood volume using Gd-DTPA contrast enhancement and dynamic T2\*-weighted MRI. *J Magn Reson Imaging*, 24, 288-96 (2006)
51. Roberts, T. P. & H. A. Rowley: Diffusion weighted magnetic resonance imaging in stroke. *Eur J Radiol*, 45, 185-94 (2003)
52. Sotak, C. H.: Nuclear magnetic resonance (NMR) measurement of the apparent diffusion coefficient (ADC) of tissue water and its relationship to cell volume changes in pathological states. *Neurochem Int*, 45, 569-82 (2004)
53. Sykova, E.: Diffusion properties of the brain in health and disease. *Neurochem Int*, 45, 453-66 (2004)
54. Charles-Edwards, E. M. & N. M. deSouza: Diffusion-weighted magnetic resonance imaging and its application to cancer. *Cancer Imaging*, 6, 135-43 (2006)
55. Foltz, W. D., N. Merchant, E. Downar, J. A. Stainsby & G. A. Wright: Coronary venous oximetry using MRI. *Magnetic Resonance in Medicine*, 42, 837-48 (1999)
56. Neeman, M., H. Dafni, O. Bukhari, R. D. Braun & M. W. Dewhirst: *In vivo* BOLD contrast MRI mapping of subcutaneous vascular function and maturation: validation by intravital microscopy. *Magn. Reson. Med.*, 45, 887-98 (2001)
57. Howe, F. A., S. P. Robinson, D. J. McIntyre, M. Stubbs & J. R. Griffiths: Issues in flow and oxygenation dependent contrast (FLOOD) imaging of tumours. *NMR in Biomed.*, 14, 497-506 (2001)
58. Baudelet, C. & B. Gallez: How does blood oxygen level-dependent (BOLD) contrast correlate with oxygen partial pressure (pO<sub>2</sub>) inside tumors? *Magn. Reson. Med.*, 48, 980-986 (2002)
59. Baudelet, C. & B. Gallez: Current issues in the utility of blood oxygen level dependent MRI for the assessment of modulations in tumor oxygenation *Curr Med Imaging Rev.*, 1, 229-243 (2005)
60. Bhujwala, Z. M., D. Artemov, E. Aboagye, E. Ackerstaff, R. J. Gillies, K. Natarajan & M. Solaiyappan: The physiological environment in cancer vascularization, invasion and metastasis. *Novartis Found Symp*, 240, 23-38; discussion 38-45, 152-3 (2001)
61. Gillies, R. J., Z. M. Bhujwala, J. Evelhoch, M. Garwood, M. Neeman, S. P. Robinson, C. H. Sotak & B. Van Der Sanden: Applications of magnetic resonance in model systems: tumor biology and physiology. *Neoplasia*, 2, 139-51 (2000)
62. Yu, J. X., V. Kodibagkar, W. Cui & R. P. Mason: <sup>19</sup>F: a versatile reporter for non-invasive physiology and pharmacology using magnetic resonance. *Curr. Med. Chem.*, 12, 818-848 (2005)
63. Evans, S. M., S. Hahn, D. R. Pook, W. T. Jenkins, A. A. Chalian, P. Zhang, C. Stevens, R. Weber, G. Weinstein, I. Benjamin, N. Mirza, M. Morgan, S. Rubin, W. G. McKenna, E. M. Lord & C. J. Koch: Detection of hypoxia in human squamous cell carcinoma by EF5 binding. *Cancer Res*, 60, 2018-24 (2000)
64. Aime, S., C. Cabella, S. Colombatto, S. Geninatti Crich, E. Gianolio & F. Maggioni: Insights into the use of paramagnetic Gd (III) complexes in MR-molecular imaging investigations. *JMRI*, 16, 394-406 (2002)
65. Kurhanewicz, J., D. B. Vigneron, R. G. Males, M. G. Swanson, K. K. Yu & H. Hricak: The prostate: MR imaging and spectroscopy. Present and future. [Review]. *Radiol. Clin. North Amer.*, 38, 115-38 (2000)
66. Minati, L., M. Grisoli & M. G. Bruzzone: MR spectroscopy, functional MRI, and diffusion-tensor imaging in the aging brain: a conceptual review. *J Geriatr Psychiatry Neurol*, 20, 3-21 (2007)
67. Cecil, K. M.: MR spectroscopy of metabolic disorders. *Neuroimaging Clin N Am*, 16, 87-116, viii (2006)
68. Horn, M.: Cardiac magnetic resonance spectroscopy: a window for studying physiology. *Methods Mol Med*, 124, 225-48 (2006)
69. Shah, N., A. Sattar, M. Benanti, S. Hollander & L. Cheuck: Magnetic resonance spectroscopy as an imaging

- tool for cancer: a review of the literature. *J Am Osteopath Assoc*, 106, 23-7 (2006)
70. De Stefano, N. & M. Filippi: MR spectroscopy in multiple sclerosis. *J Neuroimaging*, 17 Suppl 1, 31S-35S (2007)
71. Martin, W. R.: MR Spectroscopy in Neurodegenerative Disease. *Mol Imaging Biol* (2007)
72. Li, K. C. P., G. A. Wright, L. R. Pelc, R. L. Dalamn, J. H. Brittain, H. Wegmueller, J. T. Lin & C. K. Song: Oxygen saturation of blood in the superior mesenteric vein. *Radiology*, 194, 321-325 (1995)
73. Wright, G. A., B. S. Hu & A. Macovski: Estimating oxygen saturation of blood *in vivo* with MR imaging at 1.5 T. *JMRI*, 1, 275-283 (1991)
74. Dardzinski, B. J. & C. H. Sotak: Rapid tissue oxygen tension mapping using  $^{19}\text{F}$  inversion-recovery echo-planar imaging of perfluoro-15-crown-5-ether. *Magn Reson Med*, 32, 88-97 (1994)
75. Mason, R. P., W. Rodbumrung & P. P. Antich: Hexafluorobenzene: a sensitive  $^{19}\text{F}$  NMR indicator of tumor oxygenation. *NMR Biomed.*, 9, 125-134 (1996)
76. Mason, R. P.: Non-invasive physiology:  $^{19}\text{F}$  NMR of perfluorocarbons. *Artif Cells Blood Substit Immobil Biotechnol*, 22, 1141-53 (1994)
77. Glockner, J. F. & H. M. Swartz: *In vivo* EPR oximetry using two novel probes: fusicidine and lithium phthalocyanine. *Adv Exp Med Biol*, 317, 229-34 (1992)
78. Swartz, H. M., K. J. Liu, F. Goda & T. Walczak: India ink: a potential clinically applicable EPR oximetry probe. *Magn. Reson. Med.*, 31, 229-232 (1994)
79. Zweier, J. L. & P. Kuppusamy: Electron paramagnetic resonance measurements of free radicals in the intact beating heart: A technique for detection and characterization of free radicals in whole biological tissues. *Proc. Natl. Acad. Sci. (USA)*, 85, 5703-5707 (1988)
80. Matsumoto, A., S. Matsumoto, A. L. Sowers, J. W. Koscielniak, N. J. Trigg, P. Kuppusamy, J. B. Mitchell, S. Subramanian, M. C. Krishna & K. Matsumoto: Absolute oxygen tension ( $\text{pO}_2$ ) in murine fatty and muscle tissue as determined by EPR. *Magn Reson Med*, 54, 1530-5 (2005)
81. Gallez, B., C. Baudelet & B. F. Jordan: Assessment of tumor oxygenation by electron paramagnetic resonance: principles and applications. *NMR Biomed.*, 17, 240-62 (2004)
82. Gallez, B. & H. M. Swartz: *In vivo* EPR: when, how and why? *NMR Biomed.*, 17, 223-5 (2004)
83. Kodibagkar, V. D., W. Cui, M. E. Merritt & R. P. Mason: Novel  $^1\text{H}$  NMR approach to quantitative tissue oximetry using hexamethyldisiloxane. *Magn Reson Med*, 55, 743-8 (2006)
84. Thomas, S. R.: The biomedical applications of Fluorine-19 NMR. In: *Magnetic Resonance Imaging*. Eds: C. L. Partain, R. R. Price, J. A. Patton, M. V. Kulkarni & A. E. J. James. W.B. Saunders Co., London (1988)
85. Mason, R. P.: Non-invasive physiology:  $^{19}\text{F}$  NMR of perfluorocarbon. *Art. Cells, Blood Sub. & Immobil. Biotech.*, 22, 1141-1153 (1994)
86. Abragam, A.: *The Principles of Nuclear Magnetism*. Oxford University Press, New York (1961)
87. McConnell, H. M. & C. H. Holm: Anisotropic chemical shielding and nuclear magnetic relaxation in liquids. *J. Chem. Phys.*, 25, 1289 (1956)
88. Blicharski, J. S.: Interference effect in nuclear magnetic relaxation. *Phys. Lett. A*, 24, 608 (1967)
89. Farrar, T. C. & J. D. Decatur: Temperature-Dependent NMR Relaxation Studies of  $\text{Na}_2\text{PO}_3$  in Solution. *J Phys Chem*, 94, 7395-7401 (1990)
90. Matson, G. B.: Methyl NMR relaxation: the effects of spin rotation and chemical shift anisotropy mechanisms. *J. Chem. Phys.*, 67, 5152 (1977)
91. Shukla, H. P., R. P. Mason, D. E. Woessner & P. P. Antich: A comparison of three commercial perfluorocarbon emulsions as high field NMR probes of oxygen tension and temperature. *J. Magn. Reson. Series B*, 106, 131-141 (1995)
92. Hunjan, S., R. P. Mason, A. Constantinescu, P. Peschke, E. W. Hahn & P. P. Antich: Regional tumor oximetry:  $^{19}\text{F}$  NMR spectroscopy of hexafluorobenzene. *Int J Radiat Oncol Biol Phys*, 41, 161-71 (1998)
93. Delpuech, J. J., M. A. Hamza, G. Serratrice & M. J. Stebe: Fluorocarbons as Oxygen Carriers .1. Nmr-Study of Oxygen Solutions in Hexafluorobenzene. *J Chem Phys*, 70, 2680-2687 (1979)
94. Parhami, P. & B. M. Fung: F-19 Relaxation Study of Perfluoro Chemicals as Oxygen Carriers. *J Phys Chem*, 87, 1928-1931 (1983)
95. Mason, R. P., H. Shukla & P. P. Antich: *In vivo* oxygen tension and temperature: simultaneous determination using  $^{19}\text{F}$  NMR spectroscopy of perfluorocarbon. *Magn Reson Med*, 29, 296-302 (1993)
96. Mason, R. P., P. P. Antich, E. E. Babcock, J. L. Gerberich & R. L. Nunnally: Perfluorocarbon imaging *in vivo*: A  $^{19}\text{F}$  MRI study in tumor-bearing mice. *Magn. Reson. Imaging*, 7, 475-485 (1989)
97. Babcock, E. E., R. P. Mason & P. P. Antich: Effect of homonuclear J modulation on  $^{19}\text{F}$  spin-echo images. *Magn. Reson. Med.*, 17, 178-188 (1991)
98. Hunjan, S., D. Zhao, A. Constantinescu, E. W. Hahn, P. P. Antich & R. P. Mason: Tumor oximetry: demonstration of an enhanced dynamic mapping procedure using fluorine-19 echo planar magnetic resonance imaging in the Dunning prostate R3327-AT1 rat tumor. *Int J Radiat Oncol Biol Phys*, 49, 1097-108 (2001)
99. Look, D. C. & D. R. Locker: Time saving in measurement of NMR and EPR relaxation times. *Rev. Sci. Instrum.*, 41, 250 (1970)
100. Caruthers, S. D., P. J. Gaffney, F. D. Hockett, R. Lamerichs, G. M. Lanza, A. M. Neubauer, M. J. Scott, S. A. Wickline & P. M. Winter:  $^{19}\text{F}$  MR techniques augment quantitative molecular imaging with paramagnetic perfluorocarbon nanoparticles at 1.5 T. *Proc Intl Soc Magn Reson Med*, 14, 1834 (2006)
101. Hamza, M. A., G. Serratrice, M. J. Stebe & J. J. Delpuech: Fluorocarbons as Oxygen Carriers .2. An Nmr-Study of Partially or Totally Fluorinated Alkanes and Alkenes. *J Magn Reson*, 42, 227-241 (1981)
102. Hamza, M. A., G. Serratrice, M. J. Stebe & J. J. Delpuech: Solute-Solvent Interactions in Perfluorocarbon Solutions of Oxygen - an Nmr-Study. *JACS*, 103, 3733-3738 (1981)
103. Kim, H. W. & A. G. Greenburg: Artificial oxygen carriers as red blood cell substitutes: a selected review and current status. *Artif Organs*, 28, 813-28 (2004)

104. Riess, J. G.: Perfluorocarbon-based oxygen delivery. *Artif Cells Blood Substit Immobil Biotechnol*, 34, 567-80 (2006)
105. Tremper, K. K., G. M. Vercellotti & D. E. Hammerschmidt: Hemodynamic Profile of Adverse Clinical Reactions to Fluosol-Da 20-Percent. *Critical Care Medicine*, 12, 428-431 (1984)
106. Gould, S. A., A. L. Rosen, L. R. Sehgal, H. L. Sehgal, L. A. Langdale, L. M. Krause, C. L. Rice, W. H. Chamberlin & G. S. Moss: Fluosol-Da as a Red-Cell Substitute in Acute Anemia. *New England Journal of Medicine*, 314, 1653-1656 (1986)
107. Bell, M. R., R. A. Nishimura, D. R. Holmes, K. R. Bailey, R. S. Schwartz & R. E. Vlietstra: Does Intracoronary Infusion of Fluosol-Da 20-Percent Prevent Left-Ventricular Diastolic Dysfunction During Coronary Balloon Angioplasty. *J Am Coll Cardiol*, 16, 959-966 (1990)
108. Kent, K. M., M. W. Cleman, M. J. Cowley, M. B. Forman, C. C. Jaffe, M. Kaplan, S. B. King, M. W. Krucoff, T. Lassar, B. McAuley, R. Smith, C. Wisdom & D. Wohlgeleit: Reduction of Myocardial-Ischemia During Percutaneous Transluminal Coronary Angioplasty with Oxygenated Fluosol. *Am J Cardiol*, 66, 279-284 (1990)
109. Spahn, D. R., K. F. Waschke, T. Standl, J. Motsch, L. Van Huynegem, M. Welte, H. Gombotz, P. Coriat, L. Verkh, S. Faithfull & P. Keipert: Use of perflubron emulsion to decrease allogeneic blood transfusion in high-blood-loss non-cardiac surgery: results of a European phase 3 study. *Anesthesiology*, 97, 1338-49 (2002)
110. Hill, S. E., B. J. Leone, N. S. Faithfull, K. E. Flaim, P. E. Keipert & M. F. Newman: Perflubron emulsion (AF0144) augments harvesting of autologous blood: a phase II study in cardiac surgery. *J Cardiothorac Vasc Anesth*, 16, 555-60 (2002)
111. Thomas, S. R., R. W. Millard, R. G. Pratt, Y. Shiferaw & R. C. Samarungta: Quantitative pO<sub>2</sub> imaging *in vivo* with perfluorocarbon F-19 NMR: tracking oxygen from the airway through the blood to organ tissues. *Art Cells, Blood Subst. Immobil. Biotechnol.*, 22, 1029-1042 (1994)
112. Thomas, S. R., R. G. Pratt, R. W. Millard, R. C. Samarungta, Y. Shiferaw, L. C. Clark Jr. & R. E. Hoffmann: Evaluation of the Influence of the Aqueous Phase Bioconstituent Environment on the F-19 T1 of Perfluorocarbon Blood Substitute Emulsions. *JMRI*, 4, 631-635 (1994)
113. Thomas, S. R., R. G. Pratt, R. W. Millard, R. C. Samarungta, Y. Shiferaw, A. J. McGoron & K. K. Tan: *In vivo* pO<sub>2</sub> imaging in the porcine model with perfluorocarbon F-19 NMR at low field. *Magn. Reson. Imaging*, 14, 103-114 (1996)
114. Zhao, D., A. Constantinescu, C.-H. Chang, E. W. Hahn & R. P. Mason: Correlation of Tumor Oxygen Dynamics with Radiation Response of the Dunning Prostate R3327-HI Tumor. *Radiat. Res.*, 159, 621-631 (2003)
115. Zhao, D., A. Constantinescu, L. Jiang, E. W. Hahn & R. P. Mason: Prognostic Radiology: quantitative assessment of tumor oxygen dynamics by MRI. *Am. J. Clin. Oncol*, 24, 462-466 (2001)
116. Zhao, D., S. Ran, A. Constantinescu, E. W. Hahn & R. P. Mason: Tumor oxygen dynamics: correlation of *in vivo* MRI with histological findings. *Neoplasia*, 5, 308-18 (2003)
117. Mason, R. P., P. P. Antich, E. E. Babcock, A. Constantinescu, P. Peschke & E. W. Hahn: Non-invasive determination of tumor oxygen tension and local variation with growth. *Int. J. Radiat. Oncol. Biol. Phys.*, 29, 95-103 (1994)
118. Mason, R. P., F. M. H. Jeffrey, C. R. Malloy, E. E. Babcock & P. P. Antich: A noninvasive assessment of myocardial oxygen tension: <sup>19</sup>F NMR spectroscopy of sequestered perfluorocarbon emulsion. *Magn. Reson. Med.*, 27, 310-317 (1992)
119. Mason, R. P., H. P. Shukla & P. P. Antich: Oxygen: a novel probe of tissue oxygen tension. *Biomater. Artif. Cells Immobil. Biotechnol.*, 20, 929-935 (1992)
120. Hunjan, S., R. P. Mason, A. Constantinescu, P. Peschke, E. W. Hahn & P. P. Antich: Regional tumor oximetry: <sup>19</sup>F NMR spectroscopy of hexafluorobenzene. *Int. J. Radiat. Oncol. Biol. Phys.*, 40, 161-71 (1998)
121. Song, Y., A. Constantinescu & R. P. Mason: Dynamic Breast tumor oximetry: the development of Prognostic Radiology. *Technol. Cancer Res. Treat.*, 1, 471-478 (2002)
122. Xia, M., V. Kodibagkar, H. Liu & R. P. Mason: Tumour oxygen dynamics measured simultaneously by near infrared spectroscopy and <sup>19</sup>F magnetic resonance imaging in rats. *Phys. Med. Biol.*, 51, 45-60 (2006)
123. Barker, B. R., R. P. Mason, N. Bansal & R. M. Peshock: Oxygen tension mapping by <sup>19</sup>F echo planar NMR imaging of sequestered perfluorocarbon. *JMRI*, 4, 595-602 (1994)
124. Sotak, C. H., P. S. Hees, H.-H. Huang, M.-H. Hung, C. G. Krespan & S. Reynolds: A new perfluorocarbon for use in fluorine-19 magnetic resonance spectroscopy. *Magn. Reson. Med.*, 29, 188-195 (1993)
125. Sotak, C. H., P. S. Hees, H. N. Huang, M. H. Hung, C. G. Krespan & S. Reynolds: A new perfluorocarbon for use in fluorine-19 MRI and MRS. *Magn. Reson. Med.*, 29, 188-95 (1993)
126. Berkowitz, B. A., C. A. Wilson, D. L. Hatchell & R. E. London: Quantitative determination of the partial oxygen pressure in the vitrectomized rabbit eye *in vivo* using <sup>19</sup>F NMR. *Magn Reson Med*, 21, 233-41 (1991)
127. Wilson, C., B. Berkowitz, B. McCuen & C. Charles: Measurement of preretinal pO<sub>2</sub> in the vitrectomized human eye using <sup>19</sup>F NMR. *Arch. Ophthalmol*, 110, 1098-100 (1992)
128. Noth, U., S. P. Morrissey, R. Deichmann, H. Adolf, C. Schwarzbauer, J. Lutz & A. Haase: *In vivo* measurement of partial oxygen pressure in large vessels and in the reticuloendothelial system using fast <sup>19</sup>F-MRI. *Magn Reson Med*, 34, 738-45 (1995)
129. Noth, U., P. Grohn, A. Jork, U. Zimmermann, A. Haase & J. Lutz: <sup>19</sup>F-MRI *in vivo* determination of the partial oxygen pressure in perfluorocarbon-loaded alginate capsules implanted into the peritoneal cavity and different tissues. *Magn Reson Med*, 42, 1039-47 (1999)
130. Mattrey, R. F., D. J. Schumacher, H. T. Tran, Q. Guo & R. B. Buxton: The use of Imagent BP in diagnostic imaging research and <sup>19</sup>F magnetic resonance for PO<sub>2</sub>

measurements. *Biomaterials, Artificial Cells, & Immobilization Biotechnology*, 20, 917-20 (1992)

131. McIntyre, D. J. O., C. L. McCoy & J. R. Griffiths: Tumour oxygenation measurements by <sup>19</sup>F MRI of perfluorocarbons. *Curr. Sci.*, 76, 753-762 (1999)

132. Bellemann, M. E., J. Bruckner, P. Peschke, G. Brix & R. P. Mason: [Quantification and visualization of oxygen partial pressure *in vivo* by <sup>19</sup>F NMR imaging of perfluorocarbons]. *Biomed Tech (Berl)*, 47 Suppl 1 Pt 1, 451-4 (2002)

133. Lutz, J., U. Noth, S. P. Morrissey, H. Adolf, R. Deichmann & A. Haase: Measurement of oxygen tensions in the abdominal cavity and in the skeletal muscle using <sup>19</sup>F-MRI of neat PFC droplets. *Adv Exp Med Biol*, 428, 569-72 (1997)

134. Zimmermann, U., U. Noth, P. Grohn, A. Jork, K. Ulrichs, J. Lutz & A. Haase: Non-invasive evaluation of the location, the functional integrity and the oxygen supply of implants: <sup>19</sup>F nuclear magnetic resonance imaging of perfluorocarbon-loaded Ba<sup>2+</sup>-alginate beads. *Artif Cells Blood Substit Immobil Biotechnol*, 28, 129-46 (2000)

135. Lutz, J., U. Noth, S. P. Morrissey, H. Adolf, R. Deichmann & A. Haase: *In vivo* measurement of oxygen pressure using <sup>19</sup>F-NMR imaging. *Adv Exp Med Biol*, 388, 53-7 (1996)

136. Jager, L. J., U. Noth, A. Haase & J. Lutz: Half-life of perfluorooctylbromide in inner organs determined by fast <sup>19</sup>F-NMR imaging. *Adv Exp Med Biol*, 361, 129-34 (1994)

137. Nunnally, R., P. Antich, P. Nguyen, E. Babcock, G. McDonald & R. Mason: Fluosol adjuvant therapy in human cancer: examinations *in vivo* of perfluorocarbons by F-19 NM. *Proc. SMRM 7th Meeting San Francisco* 342 (1988)

138. Gewiese, B., W. Noske, A. Schilling, D. Stiller, K. Wolf & M. Foerster: Human eye: visualization of perfluorodecalin with F-19 MR imaging. *Radiology*, 185, 131-3 (1992)

139. Tadamura, E., H. Hatabu, W. Li, P. V. Prasad & R. R. Edelman: Effect of oxygen inhalation on relaxation times in various tissues. *J Magn Reson Imaging*, 7, 220-5 (1997)

140. Berkowitz, B. A., Y. Ito, T. S. Kern, C. McDonald & R. Hawkins: Correction of early subnormal superior hemiretinal DeltaPO (2) predicts therapeutic efficacy in experimental diabetic retinopathy. *Invest Ophthalmol Vis Sci*, 42, 2964-9 (2001)

141. Berkowitz, B. A., C. McDonald, Y. Ito, P. S. Tofts, Z. Latif & J. Gross: Measuring the human retinal oxygenation response to a hyperoxic challenge using MRI: eliminating blinking artifacts and demonstrating proof of concept. *Magn Reson Med*, 46, 412-6 (2001)

142. Zaharchuk, G., A. J. Martin, G. Rosenthal, G. T. Manley & W. P. Dillon: Measurement of cerebrospinal fluid oxygen partial pressure in humans using MRI. *Magnetic Resonance in Medicine*, 54, 113-121 (2005)

143. Zaharchuk, G., R. F. Busse, G. Rosenthal, G. T. Manley, O. A. Glenn & W. P. Dillon: Noninvasive oxygen partial pressure measurement of human body fluids *in vivo* using magnetic resonance imaging. *Academic Radiology*, 13, 1016-1024 (2006)

144. Kodibagkar, V. D. & R. P. Mason: Proton Imaging of Silanes to map Tissue Oxygenation Levels (PISTOL): a new tool for quantitative tissue oximetry. *Proc Intl Soc Magn Reson Med*, 14, 928 (2006)

145. Cassidy, S. L., A. Dotti, G. B. Kolesar, L. W. Dochterman, R. G. Meeks & H. J. Chevalier: Hexamethyldisiloxane: A 13-week subchronic whole-body vapor inhalation toxicity study in Fischer 344 rats. *Int J Toxicol*, 20, 391-9 (2001)

146. Dobrev, I. D., M. B. Reddy, K. P. Plotzke, S. Varaprath, D. A. McNett, J. Durham & M. E. Andersen: Closed-chamber inhalation pharmacokinetic studies with hexamethyldisiloxane in the rat. *Inhal Toxicol*, 15, 589-617 (2003)

147. Riess, J. G.: Overview of progress in the fluorocarbon approach to *in vivo* oxygen delivery. *Biomater Artif Cells Immobilization Biotechnol*, 20, 183-202 (1992)

148. Haase, A., J. Frahm, W. Hanicke & D. Matthaei: <sup>1</sup>H NMR chemical shift selective (CHESS) imaging. *Phys Med Biol*, 30, 341-4 (1985)

149. Zhao, D., L. Jiang, E. W. Hahn & R. P. Mason: Tumor physiologic response to combretastatin A4 phosphate assessed by MRI. *Int J Radiat Oncol Biol Phys*, 62, 872-80 (2005)

150. Wickline, S. A., A. M. Neubauer, P. M. Winter, S. D. Caruthers & G. M. Lanza: Molecular imaging and therapy of atherosclerosis with targeted nanoparticles. *J Magn Reson Imaging*, 25, 667-80 (2007)

**Key Words:** Oximetry, hypoxia, perfluorocarbons, MRI, <sup>19</sup>F, hexamethyldisiloxane, Review

**Send correspondence to:** Vikram Kodibagkar, Ph.D., Assistant Professor of Radiology, UT Southwestern Medical Center at Dallas, 5323 Harry Hines Blvd., Dallas, TX 75390-9058, Tel: 214-648-7612, Fax: 214-648-4538, E-mail: vikram.kodibagkar@utsouthwestern.edu

<http://www.bioscience.org/current/vol13.htm>

# Proton imaging of siloxanes to map tissue oxygenation levels (PISTOL): a tool for quantitative tissue oximetry<sup>†</sup>

Vikram D. Kodibagkar,<sup>1</sup> Xianghui Wang,<sup>1</sup> Jesús Pacheco-Torres,<sup>1,2</sup> Praveen Gulaka<sup>1</sup> and Ralph P. Mason<sup>1\*</sup>

<sup>1</sup>Cancer Imaging Program, Department of Radiology, University of Texas Southwestern Medical Center, Dallas, TX, USA

<sup>2</sup>Instituto de Investigaciones Biomédicas 'Alberto Sols', CSIC, Madrid, Spain

Received 29 January 2008; Revised 14 March 2008; Accepted 17 March 2008

**ABSTRACT:** Hexamethyldisiloxane (HMDSO) has been identified as a sensitive proton NMR indicator of tissue oxygenation (pO<sub>2</sub>) based on spectroscopic spin-lattice relaxometry. A rapid MRI approach has now been designed, implemented, and tested. The technique, proton imaging of siloxanes to map tissue oxygenation levels (PISTOL), utilizes frequency-selective excitation of the HMDSO resonance and chemical-shift selective suppression of residual water signal to effectively eliminate water and fat signals and pulse-burst saturation recovery <sup>1</sup>H echo planar imaging to map T<sub>1</sub> of HMDSO and hence pO<sub>2</sub>. PISTOL was used here to obtain maps of pO<sub>2</sub> in rat thigh muscle and Dunning prostate R3327 MAT-Lu tumor-implanted rats. Measurements were repeated to assess baseline stability and response to breathing of hyperoxic gas. Each pO<sub>2</sub> map was obtained in 3½ min, facilitating dynamic measurements of response to oxygen intervention. Altering the inhaled gas to oxygen produced a significant increase in mean pO<sub>2</sub> from 55 Torr to 238 Torr in thigh muscle and a smaller, but significant, increase in mean pO<sub>2</sub> from 17 Torr to 78 Torr in MAT-Lu tumors. Thus, PISTOL enabled mapping of tissue pO<sub>2</sub> at multiple locations and dynamic changes in pO<sub>2</sub> in response to intervention. This new method offers a potentially valuable new tool to image pO<sub>2</sub> *in vivo* for any healthy or diseased state by <sup>1</sup>H MRI. Copyright © 2008 John Wiley & Sons, Ltd.

**KEYWORDS:** oximetry; oxygen tension; muscle; prostate tumor; echo planar imaging (EPI); water and fat suppression; hexamethyldisiloxane

## INTRODUCTION

There is increasing evidence that hypoxia stimulates angiogenesis and metastasis and that hypoxic tumors are more aggressive (1). Furthermore, extensive hypoxia has been associated with poor clinical prognosis for several tumor types, notably cervical and head and neck, based on electrode measurements (2–4). Extensive hypoxia has also been identified in prostate, breast, and brain tumors (5–7). It is expected from definitive observations in cell culture (8) and preclinical investigations in rats and mice (1,9–11) that hypoxic tumors resist radiotherapy.

Measurement of tumor hypoxia is becoming increasingly pertinent, as therapy can now be tailored to the characteristics of individual tumors, i.e. personalized medicine. An adjuvant intervention may be applied to patients with hypoxic tumors, e.g. hyperoxic gas breathing to reduce hypoxic fraction. Alternatively, for tumors that resist modulation, a radiation boost may be applied using intensity modulated radiation therapy, or a hypoxic-cell-selective cytotoxin, such as tirapazamine, may be administered.

The ability to measure tissue oxygen tension (pO<sub>2</sub>) non-invasively may be important in understanding the physiology, pathophysiology, and, potentially, clinical prognosis of diseases such as cancer and stroke. To date, many assays have examined hypoxia, rather than pO<sub>2</sub> itself. Radionuclide approaches using fluoromisonidazole and copper diacetyl-bis(N<sup>4</sup>-methylthiosemicarbazone) can identify hypoxia and have shown predictive value in clinical studies (1). Likewise, immunohistochemistry of biopsy samples after pimonidazole or EF5 (a fluorinated derivative of etanidazole) administration and trapping in tumor tissues have been correlated with outcome (7,12). MRI is particularly suitable for multiple repeat measurements for observing dynamic changes in tissue oxygenation in response to intervention, and blood-oxygen-level-dependent (BOLD) contrast gives an indication of vascular oxygenation, albeit usually

\*Correspondence to: R. P. Mason, Department of Radiology, University of Texas Southwestern Medical Center, 5323 Harry Hines Boulevard, Dallas, TX 75390-9058, USA.

E-mail: ralph.mason@utsouthwestern.edu.

<sup>†</sup>Presented in part at the 14th Annual Meeting of the International Society of Magnetic Resonance in Medicine, Seattle, 2006

Contract/grant sponsor: DAMD; contract/grant number: W81XWH-06-1-0149.

Contract/grant sponsor: NIH; contract/grant number: P41RR02584.

Contract/grant sponsor: NIH; contract/grant number: U24 CA126608.

**Abbreviations used:** ARDVARC, alternating relaxation delays with variable acquisitions for reduction of clearance effects data acquisition protocol; BOLD, blood oxygen level dependent; CHESS, chemical-shift selective; EPI, echo planar imaging; FREEDOM, fluorocarbon relaxometry using echo planar imaging for dynamic oxygen mapping; HFB, hexafluorobenzene; HMDSO, hexamethyldisiloxane; MAT-Lu, Dunning prostate R3327-AT tumor subline metastatic to lungs; PBSR, pulse-burst saturation recovery; pO<sub>2</sub>, oxygen tension; PISTOL, proton imaging of siloxanes to map tissue oxygenation levels.

qualitative (13–15).  $^{19}\text{F}$  NMR can provide quantitative oximetry based on spin-lattice relaxation of perfluorocarbons (16), although it is currently limited to preclinical studies, as reviewed in detail (17,18). The technique has been used to evaluate the ability to manipulate tumor  $\text{pO}_2$  based on hyperoxic gas breathing. Most significantly, correlations have been shown between  $\text{pO}_2$  at the time of irradiation and growth delay in Dunning prostate R3327-HI and R3327-AT1 rat tumors (10,11) using hexafluorobenzene (HFB) as a reporter molecule.

Although  $^{19}\text{F}$ -MR oximetry is well established and continues to make important contributions to basic research, its clinical translation is hampered by the continuing lack of  $^{19}\text{F}$  capability on most clinical MRI scanners. Recently, hexamethyldisiloxane (HMDSO) was identified as a  $^1\text{H}$ -NMR probe of  $\text{pO}_2$ , and the feasibility of tissue oximetry was presented using  $^1\text{H}$ -NMR spectroscopic relaxometry of HMDSO, after direct intra-tissue injection (19). With the use of the spectroscopic approach, localization was achieved by virtue of a discrete injection site. The present study demonstrates the implementation of an imaging-based method: proton imaging of siloxanes to map tissue oxygenation levels (PISTOL). As proof of principle, phantom studies are presented and this  $\text{pO}_2$  reporter molecule is used to investigate dynamic changes in  $\text{pO}_2$  in rat thigh muscle and syngeneic Dunning prostate R3327-MAT-Lu tumors in response to respiratory challenge with oxygen. A comparative  $^{19}\text{F}$ -MR oximetry study was also carried out in rat thigh muscle using HFB.

## METHODS

### Pulse sequence for measuring $\text{pO}_2$

NMR experiments were performed using a Varian Inova<sup>®</sup> 4.7 T horizontal-bore system equipped with actively shielded gradients. A chemical-shift selective (CHESS) spin-echo sequence was used to identify the location of HMDSO. A spin-echo echo planar imaging (EPI)-based pulse sequence (Fig. 1) was then used for measuring  $T_1$  values for this slice location. The sequence consisted of an initial pulse-burst saturation recovery (PBSR) preparation sequence with 20 non-selective saturation pulses (inter-pulse delay = 50 ms) followed by a variable delay,  $\tau$ , for magnetization recovery. Three CHESS (20) pulses can be included at the end of  $\tau$  for optional frequency-selective saturation of water and fat. A spin-echo EPI acquisition, consisting of a frequency-selective  $\pi/2$  pulse (on-resonance for HMDSO), a slice-selective  $\pi$  pulse, and an EPI readout, follows  $\tau$ . A long echo time ( $\sim 50$  ms) was used, which aided suppression of the fat resonance. This combination of PBSR with frequency-selective excitation EPI (HMDSO) and suppression (water, fat) allowed  $T_1$  mapping of HMDSO in  $3\frac{1}{2}$  min. For  $^{19}\text{F}$ -MR oximetry

experiments, FREEDOM (fluorocarbon relaxometry using echo planar imaging for dynamic oxygen mapping) was applied using a standard EPI sequence with PBSR (17). The location of HFB was easily determined by using a standard spin-echo sequence, because of the lack of  $^{19}\text{F}$  background signal. In both cases ( $^1\text{H}$  and  $^{19}\text{F}$ ),  $T_1$  values were obtained using the corresponding sequence with the ARDVARC (alternating relaxation delays with variable acquisitions for reduction of clearance effects) protocol (21). Varying  $\tau$  in the range 0.1–55 s, gave a total acquisition time of  $3\frac{1}{2}$  min per  $T_1$  measurement for PISTOL.  $T_1$ ,  $R_1$  ( $=1/T_1$ ) and  $\text{pO}_2$  maps were computed on a voxel-by-voxel basis using a home-built program written in Matlab (Mathworks Inc., Natick, MA, USA). For a given voxel, the  $T_1$  value was obtained by a three-parameter least-squares curve fit of the signal intensities corresponding to 16  $\tau$  values using the Levenberg–Marquardt algorithm. The  $R_1$  maps were converted into  $\text{pO}_2$  maps using previously published calibration curves (19).

**Phantom experiments.** A phantom consisting of tubes containing water, mineral oil (to simulate fat), and HMDSO was used to optimize the pulse sequence and test water and fat suppression. To measure the  $\text{pO}_2$  vs  $R_1$  calibration curve by imaging, a second phantom consisting of four gas-tight John Young NMR tubes (Wilmad Labglass, Buena, NJ, USA) containing 1 mL HMDSO each bubbled with different concentrations of  $\text{O}_2$  (0%, 5%, 10%, and 21% calibrated gases; Airgas Southwest, Dallas, TX, USA) was used. Temperature was kept constant with a  $\text{D}_2\text{O}$ -filled circulating water pad and monitored using a fiber-optic temperature probe (FISO Technologies Inc., Quebec City, Quebec, Canada). Mean intensities of each region of interest corresponding to each tube were obtained from the  $T_1$  maps and converted into  $R_1$  values. Measurements were repeated six times to provide mean  $R_1$  values to obtain a calibration curve.

### *In vivo* experiments

The animal investigations were approved by the Institutional Animal Care and Use Committee. Ten healthy Copenhagen-2331 rats (Harlan, Indianapolis, IN, USA) were used to obtain  $\text{pO}_2$  data in the thigh muscle (six rats for HMDSO studies and four separate rats for HFB studies). A further six male Copenhagen rats were implanted with Dunning prostate R3327 MAT-Lu tumors subcutaneously on the thigh, to obtain  $\text{pO}_2$  data in tumors. Tumors were allowed to grow to a range of sizes from 1.2 to  $10.6\text{ cm}^3$  (five were  $> 3\text{ cm}^3$ ). For MRI, rats were maintained under general gaseous anesthesia (air and 1.5% isoflurane; Baxter International Inc, Deerfield, IL, USA). For  $\text{pO}_2$  measurements *in vivo*, 50  $\mu\text{L}$  HMDSO (99.7%; Alfa Aesar, Ward Hill, MA, USA) was administered along two or three tracks in the thigh

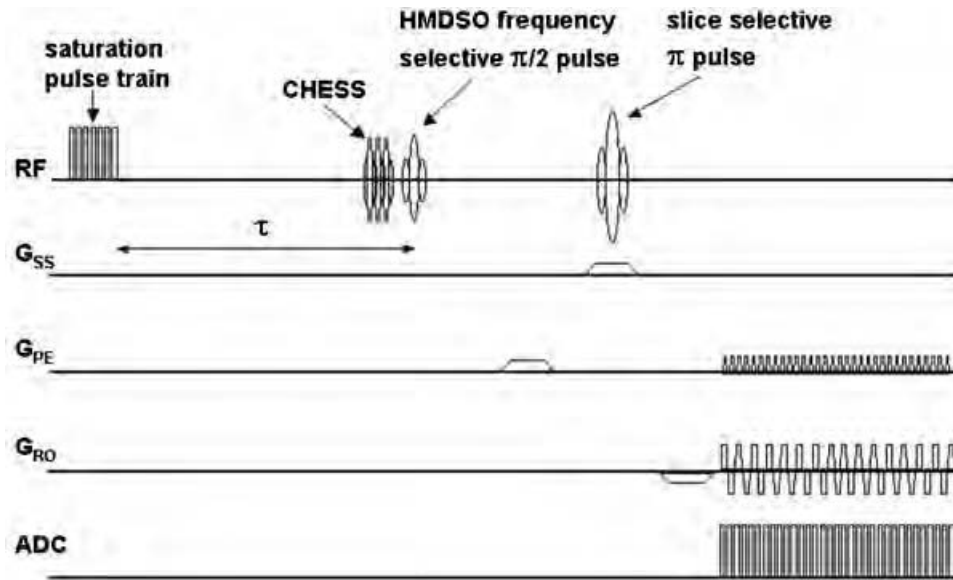


**Figure 1.** Pulse sequence for HMDSO relaxometry with optional CHES fat and water suppression (PISTOL). Magnetization preparation consists of 20  $\pi/2$  saturation pulses followed by a variable recovery time  $\tau$ . The  $\pi/2$  pulse is frequency selective for the HMDSO resonance, whereas the  $\pi$  pulse is slice selective. EPI readout enables  $T_1$  mapping in 3½ min.

muscle ( $n=6$ ) or MAT-Lu tumors ( $n=6$ ) in a single plane using a Hamilton syringe with a 32G needle, as described in detail previously for the analogous  $^{19}\text{F}$ -NMR approach (17). For comparative  $^{19}\text{F}$ -MR  $\text{pO}_2$  measurements, 50  $\mu\text{L}$  HFB (99.9%; Lancaster Co., Pelham, NH, USA) was administered in the thigh muscle, in a separate cohort of animals ( $n=4$ ), as above. The rats were placed in the magnet in the prone position, and body temperature was maintained using a warm water blanket. The thigh or tumor was placed inside a size-matched single-turn  $^1\text{H}/^{19}\text{F}$  tunable volume coil. A cross-section through the thigh or tumor was imaged after HMDSO or HFB was located, as described above. In order to modulate tissue oxygenation, the rats were subjected to respiratory challenge in the sequence, air (20 min) – oxygen (30 min) – air (30 min), and  $T_1$  datasets were acquired every 5 min.  $\text{pO}_2$  values were obtained from the  $R_1$  values. Typically, 16  $\text{pO}_2$  maps were obtained over a period of 80 min. The statistical significance of changes in  $\text{pO}_2$  was assessed by using analysis of variance on the basis of Fisher's protected least-squares difference test at 95% confidence level (Statview, SAS Institute, Carey, NC, USA).

## RESULTS

### Phantom studies

Suppression of water and mineral oil signals using the spectrally selective spin-echo EPI sequence (Fig. 1) was successful in a water-filled phantom containing smaller tubes of HMDSO and mineral oil (Fig. 2a,b).

$T_1$  measurements from the phantom comprising sealed HMDSO tubes with different oxygen concentrations (at 36.5°C) yielded  $T_1$  values essentially identical with those reported previously by spectroscopy (19) (Fig. 2c,d,e). A linear fit to the data yielded a calibration curve  $R_1 = (0.108 \pm 0.001) + (0.00130 \pm 0.00001) \times \text{pO}_2$  at 36.5°C.

### Tissue oxygenation

HMDSO was readily observed in thigh muscle and tumors by PISTOL with complete suppression of fat and water signals. Discrete distribution of HMDSO was seen in thigh muscle (Fig. 3a,b) and a MAT-Lu tumor (Fig. 3f,g) using the CHES spin-echo sequence. These appear spatially similar to the images of HMDSO and the corresponding  $\text{pO}_2$  maps acquired using PISTOL (Fig. 3c–e and 3h–j). The imaging data revealed the  $\text{pO}_2$  distribution, showing the effect of breathing oxygen. Baseline  $\text{pO}_2$  values were obtained by averaging four baseline  $\text{pO}_2$  measurements while the rats breathed air. In rat thigh muscle ( $n=6$ ), mean baseline  $\text{pO}_2$  ranged from 27 to 71 Torr (mean =  $55 \pm 17$  Torr), but was stable in any given muscle (mean variation =  $\pm 4$  Torr over 20 min). On alteration of inhaled gas to oxygen, mean  $\text{pO}_2$  increased significantly (Fig. 4a) and continued to increase over 20 min. For the group of thigh muscles, mean  $\text{pO}_2$  was significantly elevated ( $P < 0.05$ ) compared with baseline by the first measurement (5 min) after the switch of inhaled gas to oxygen and reached values of 163–290 Torr (mean  $\text{pO}_2 = 238 \pm 59$  Torr) after 30 min of breathing oxygen. On return to air breathing, mean  $\text{pO}_2$  had decreased significantly by the first measurement

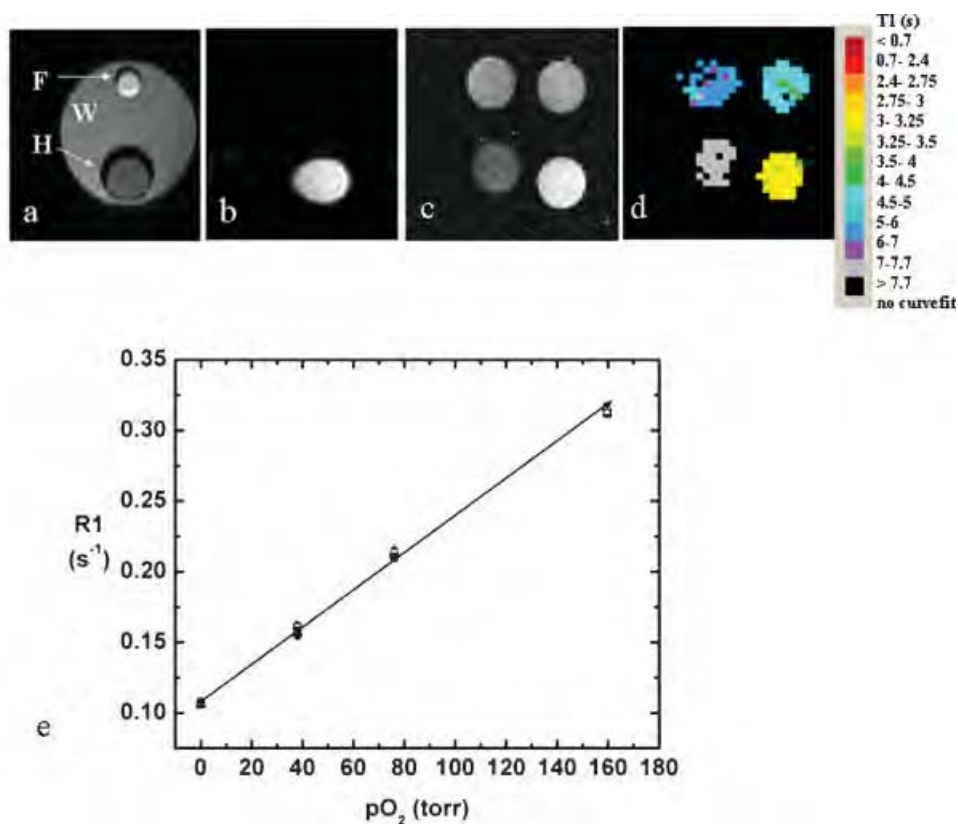


**Figure 2.** Water and fat suppression. (a)  $T_1$ -weighted spin-echo image of phantom with smaller tubes containing mineral oil (F) and HMDSO (H) inside a tube containing water (W), and (b) EPI image of the same phantom with fat and water suppression. (c)  $T_1$ -weighted spin-echo image and (d)  $T_1$  maps of a phantom comprising HMDSO saturated with gases at different concentrations of oxygen (clockwise from bottom left: 0%, 5%, 10% and 21%) obtained using PISTOL. (e) A linear fit to the data (mean region of interest intensities, six measurements) yields the calibration curve:  $R_1 = (0.108 \pm 0.001) + (0.00130 \pm 0.001) \times pO_2$  at 36.5°C.

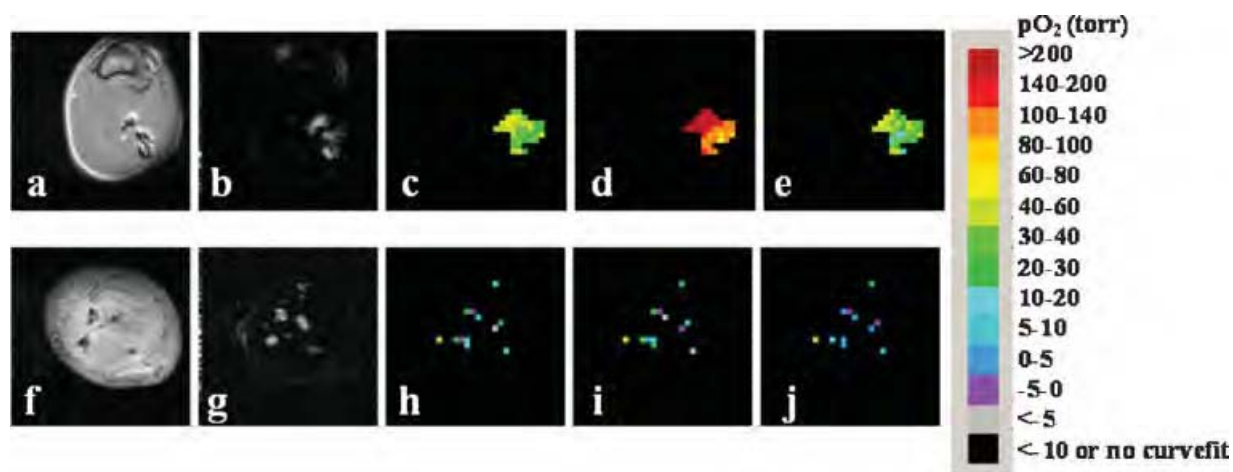


**Figure 3.** Monitoring changes in oxygenation of rat thigh muscle and Dunning prostate R3327 prostate MAT-Lu tumors implanted in Copenhagen rat thigh *in vivo* with respect to oxygen challenge. Spin-echo images of a representative rat thigh muscle (a) and MAT-Lu tumor (f). CHESS spin-echo images of silane injected into thigh muscle (b) and tumor (g) showing the distribution of the injected HMDSO. The corresponding time course PISTOL pO<sub>2</sub> maps (c, h, baseline air breathing; d, i, 30 min oxygen; e, j, 30 min after return to air breathing) showing the response to hyperoxic gas intervention in each case.

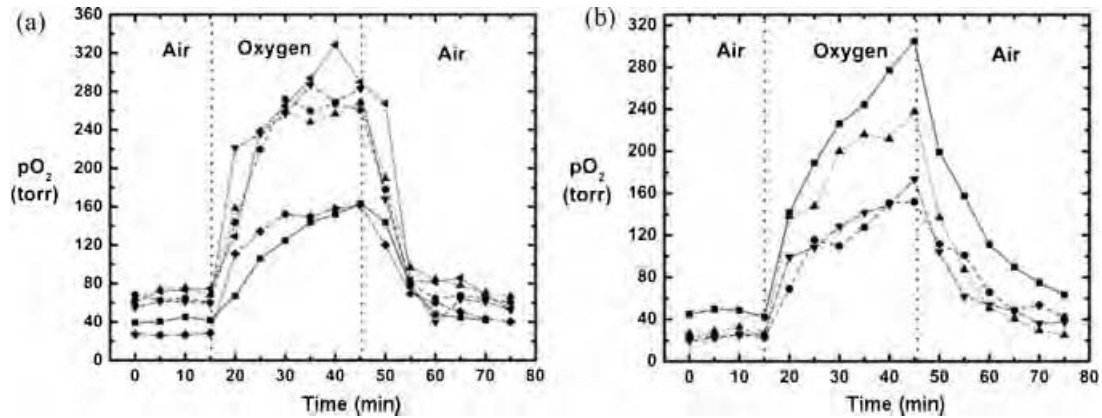


**Figure 4.** Dynamic changes in tissue oxygenation measured *in vivo* in rat thigh muscle. Individual curves are shown for mean pO<sub>2</sub> values using (a) HMDSO ( $n = 6$ ) and (b) HFB ( $n = 4$ ).

(5 min) and had returned to a value not significantly different from baseline by the second measurement (10 min). Measurements of pO<sub>2</sub> in thigh muscle using HFB yielded similar results (Fig. 4b). For this group ( $n = 4$ ), mean baseline pO<sub>2</sub> ranged from 23 to 51 Torr (mean =  $35 \pm 11$  Torr), and was stable in any given muscle (mean variation =  $\pm 3$  Torr over 20 min). In response to oxygen breathing, mean pO<sub>2</sub> was significantly elevated ( $P < 0.05$ ) compared with baseline by the first measurement (5 min) after the switch of inhaled gas to oxygen and had reached values of 152–305 Torr (mean pO<sub>2</sub> =  $211 \pm 79$  Torr) after 30 min of breathing oxygen. On return to air breathing, mean pO<sub>2</sub> had decreased significantly by the third measurement (15 min) and had returned to a value not significantly different from baseline by the fourth measurement (20 min).

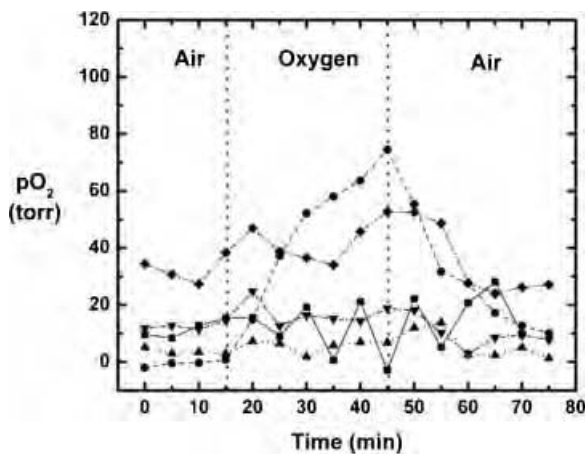


**Figure 5.** Dynamic changes in mean tissue oxygenation measured *in vivo* in MAT-Lu tumors (five out of total six) with respect to oxygen challenge. Tumor 6 showed HMDSO only in the tumor periphery and displayed uncharacteristically large response to oxygen challenge. It was excluded from the figure for better visualization of the rest of the data.

In rat prostate MAT-Lu tumors ( $n = 6$ ), mean baseline pO<sub>2</sub> ranged from  $-0.5$  to 41 Torr (mean =  $17 \pm 16$  Torr), but was stable in each tumor (mean variation =  $\pm 2$  Torr over 20 min). Tumors 1–5 showed a mean baseline pO<sub>2</sub> =  $12 \pm 12$  Torr with a mean variation of  $\pm 2$  Torr. For these five tumors, mean pO<sub>2</sub> was significantly elevated ( $P < 0.05$ ) compared with baseline by the fifth measurement (25 min) after the switch of inhaled gas to oxygen (Fig. 5). When oxygen was breathed for 30 min, mean pO<sub>2</sub> reached  $30 \pm 27$  Torr (range 7–69). On switching back to air from oxygen, mean pO<sub>2</sub> had returned to a value not significantly different from baseline by the second measurement (10 min). Tumor 6 exhibited particularly high pO<sub>2</sub> response to breathing oxygen (mean pO<sub>2</sub> =  $323 \pm 44$  Torr after 30 min of oxygen breathing), which was very different from the other tumors. Comparing the <sup>1</sup>H anatomical (H<sub>2</sub>O) and selective HMDSO images showed that the HMDSO was deposited in the tumor periphery and was probably not representative of the tumor bulk. Hence, it has been excluded from Fig. 5. Figure 6 shows histograms of pO<sub>2</sub> distributions for pooled voxels from rat thigh muscle (Fig. 6a) and MAT-Lu tumors (Fig. 6b) and changes in the distribution after 30 min of oxygen breathing. Figure 7 shows the changes in representative voxels (five each) from a representative muscle (Fig. 7a) and tumor (Fig. 7b, same tumor as shown in Fig. 3). Data for individual tumors are summarized in Table 1.

## DISCUSSION

HMDSO has previously been shown to be a promising <sup>1</sup>H-MR-based pO<sub>2</sub> reporter molecule for spectroscopic *in vivo* studies based on the linear dependence of its spin-lattice relaxation rate  $R_1$  on pO<sub>2</sub> at a given temperature in the range 26–46°C (19). The present study demonstrates the feasibility of imaging dynamic

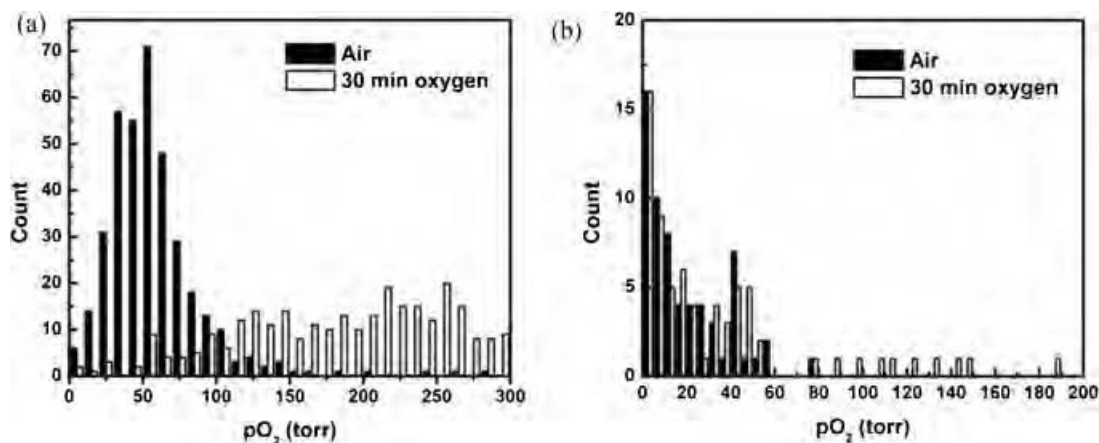


**Figure 6.** Distribution of tissue oxygenation measured *in vivo* by PISTOL. Histograms of  $pO_2$  distributions for pooled voxels from (a) rat thigh muscle ( $n = 6$ ) and (b) MAT-Lu tumors ( $n = 6$ ) with respect to oxygen challenge.

changes in tissue oxygenation using frequency-selective EPI of HMDSO, after direct injection into tissue.

In seeking a proton NMR  $pO_2$  reporter molecule, HMDSO was selected for its similarity to traditional  $^{19}F$ -NMR perfluorocarbon agents. HMDSO is hydrophobic and is essentially immiscible with aqueous solutions. Thus, gas exchange with the surrounding tissue occurs without exchange of ions, which might influence the spin lattice relaxation; thus, the validity of *in vitro* calibrations is maintained for *in vivo* determinations. HMDSO is readily available, inexpensive, and easy to store. Although HMDSO was used here, other symmetric, hydrophobic siloxanes may also be effective  $pO_2$  reporter molecules, and this new concept is open to development and optimization. In the perfluorocarbon field, many different molecules have been exploited for *in vivo* oximetry over the years (22,23). Initially, perfluorocarbon blood substitute emulsions were favored for their biocompatibility, but multi-resonance molecules, such as perfluorotributylamine and perflubron (perfluoro-octylbromide) were suboptimal for oximetry,

because of relatively low  $R_1$  dependence on  $pO_2$  and high dependence on temperature (22). Moreover, the multi-resonance spectra caused considerable signal loss for imaging (24). Ultimately, HFB and perfluoro-15-crown-5 ether were identified as superior because of their single resonances (18,25,26), and HFB is particularly attractive because of its low temperature dependence and ready commercial availability. Just as the perfluorocarbon oximetry field has evolved, other siloxanes may be identified or developed that may be superior to HMDSO.

Mapping  $pO_2$  was demonstrated using frequency-selective excitation of the HMDSO resonance with efficient frequency-selective fat and water suppression *in vitro* and *in vivo*. The calibration curve obtained here with imaging compares well with the calibration curve obtained previously by spectroscopy (19). Clearance of HMDSO from tissues (half-life  $\sim 35$  h) is relatively slow compared with clearance of HFB used in the analogous  $^{19}F$ -MR oximetry (FREEDOM) (17,27), so that there is minimal clearance during a typical investigation of oxygen dynamics in response to acute interventions (19).

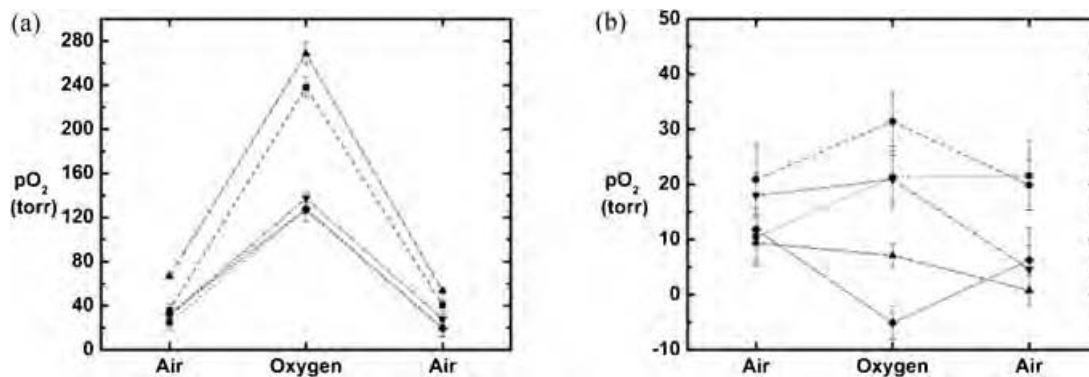


**Figure 7.** Dynamic changes in  $pO_2$  values of representative voxels from (a) thigh muscle and (b) rat prostate MAT-Lu tumor. Five voxels were selected from each tissue in Fig. 3 and examined with respect to oxygen challenge. The values are shown during air breathing, 30 min after switching to oxygen, and 30 min after switching back to air. Error bars represent the standard error of curve fit.

**Table 1. Mean + SD pO<sub>2</sub> and hypoxic fraction (HF<sub>5</sub>, percentage voxels with pO<sub>2</sub> < 5 Torr) for individual tumors with respect to hyperoxic gas challenge in the sequence: air–oxygen–air**

Tumor number and size (cm <sup>3</sup> )	Intervention					
	Air (baseline)		Oxygen		Air (return)	
	pO <sub>2</sub> (Torr)	HF <sub>5</sub> (%)	pO <sub>2</sub> (Torr)	HF <sub>5</sub> (%)	pO <sub>2</sub> (Torr)	HF <sub>5</sub> (%)
1 (1.2)	11.5 ± 3.2	50	9.1 ± 16.9	72	9.8 ± 11.2	33
2 (10.3)	−0.5 ± 1.2	70	69 ± 7.6*	2**	11.4 ± 1.8*	42**
3 (10.8)	3.6 ± 1.0	71	6.9 ± 0.1*	45*	3.2 ± 2.7	58
4 (3.7)	12.7 ± 1.4	38	16.6 ± 3.2	54	8.6 ± 1.1	57
5 (9.1)	32.7 ± 4.7	56	49.2 ± 4.9**	60	26.6 ± 0.6	58
6 <sup>a</sup> (5.6)	40.5 ± 2.7	0	318 ± 6**	0	39.7 ± 2.0	0
Mean ± SD (n = 6)	17 ± 16	48 ± 26	78 ± 120*	39 ± 31	17 ± 14*	41 ± 23
Mean ± SD (n = 5, Nos 1–5)	12 ± 12	57 ± 14	30 ± 27**	47 ± 27	12 ± 19*	50 ± 12

For individual tumors, mean pO<sub>2</sub> or HF<sub>5</sub> was compared between baseline air breathing and the last two measurements with oxygen breathing or return to air.

\**P* < 0.05.

\*\**P* < 0.01.

<sup>a</sup>Tumor 6 showed unusually high pO<sub>2</sub> and response, and comparison of the <sup>1</sup>H anatomical (H<sub>2</sub>O) and selective HMDSO MR images showed that HMDSO had been deposited in the tumor periphery.

Thus, although FREDOM provides sensitive assessment of acute changes in response to respiratory challenge or vascular targeting agents, the slower clearance of HMDSO may facilitate studies of chronic changes in tumor oxygenation accompanying tumor growth or long-term chemotherapy. Application of HMDSO to breast studies could be difficult in the presence of silicone implants because of the similar chemical shifts.

In rat thigh muscle, the range of baseline pO<sub>2</sub> values measured by PISTOL and pO<sub>2</sub> response to oxygen challenge were similar to those measured here by the well-established <sup>19</sup>F-MR oximetry technique and those reported previously using <sup>1</sup>H spectroscopy of HMDSO (19) or <sup>19</sup>F MRI of HFB (28), needle electrodes, fiber optical probes (29,30), or electron paramagnetic resonance (31,32). The response of individual voxels and muscles in separate rats to oxygen breathing depends on voxel location (Figs. 3, 4, 6, and 7), but the baseline values and response are generally higher than seen in tumors. As also reported by Yeh *et al.* (33), based on measurements using oxygen electrodes, the pO<sub>2</sub> of Dunning prostate tumors tends to be lower than in skeletal muscle. The baseline pO<sub>2</sub> values and pO<sub>2</sub> response to oxygen challenge are quite similar to those reported previously for large MAT-Lu tumors using <sup>19</sup>F-MR oximetry (34). Different rat prostate and breast tumor types are reported to exhibit a range of baseline oxygenations, and the response to interventions is highly variable. In some cases, hypoxic fractions resist modulation with hyperoxic gas breathing [e.g. Dunning prostate R3327-AT1 tumors (10,35)]. In other tumors, notably with a well-developed and highly perfused vasculature, hyperoxic gas essentially eliminated hypoxia [large Dunning prostate R3327-HI tumors (11)].

Direct intratumoral injection of the reporter molecule has benefits and drawbacks. It allows immediate

measurement of any region of interest after minimally invasive administration. By contrast, reporter molecules administered systemically initially report vascular oxygenation (36) and even after clearance tend to sequester in well-perfused regions biasing measurements (37). Of course, direct injection does limit measurements to accessible tissues. It would be preferable to exploit endogenous molecules as used in BOLD contrast, but this reveals vascular oxygenation and is subject to variations in vascular volume, hematocrit, and flow (13,14). Direct measurements of tissue water *T*<sub>1</sub> are attractive (38,39), but they may be influenced by many factors in addition to pO<sub>2</sub>. Like perfluorocarbons, HMDSO is lipophilic and is essentially immiscible in aqueous solutions. It could be emulsified for systemic delivery to help circumvent the need for direct intra-tissue injections, and such an attempt is currently underway. Some silanes are highly reactive, whereas HMDSO is quite inert, and is reported to exhibit minimal toxicity (40,41). In a 13-week subchronic inhalation toxicity study in Fischer 344 rats exposed to 5000 ppm of HMDSO, no treatment-related signs of toxicity or mortality, or other significant histological changes were found (40). After oral (300 mg/kg) or intravenous administration (80 mg/kg, as emulsion) of HMDSO, various polar metabolites were found in the urine as a result of the oxidation of the Si–CH<sub>3</sub> bond (42). Another study reported no irritation in Draize tests of skin or eye irritancy and no acute toxicity in rats (LD<sub>50</sub> > 3.8 g/kg) (43). In our studies, we saw no overt signs of inflammation or discomfort, although no microscopic analyses were performed. For future routine use as an intra-tissue-injected pO<sub>2</sub> reporter molecule, further investigation of possible local inflammatory response after direct injection of siloxanes is warranted.

In summary, PISTOL is a sensitive, quantitative <sup>1</sup>H-MR method for imaging oxygen tension and dynamic

changes in response to interventions. This new technique opens up further opportunities to evaluate  $pO_2$  *in vivo*. Rapid translation of this method to the clinical setting is feasible with current state-of-the-art MR hardware, as clinical instruments can routinely generate effective water and fat suppression as used in detection of metabolites such as choline, lactate, and citrate. A further advantage of PISTOL is that it will now be possible to add quantitative oximetry to a protocol consisting of other  $^1H$ -MR-based functional techniques routinely used for research as well as clinical diagnosis, such as dynamic contrast enhancement, diffusion measurements, and MRS.

### Acknowledgements

We are grateful to Jennifer McAnally for assistance in tumor implantation and to Drs Dawen Zhao, Weina Cui, and Mark Conradi for constructive suggestions. We appreciate the help of Glenn Katz in preparing the figures. We also thank Dr Maj Hedeus (Varian Inc., Palo Alto, CA, USA) for helpful tips in pulse sequence programming. J.P.T. gratefully acknowledges a fellowship from the Comunidad de Madrid. This work was supported in part by the DOD Prostate Cancer Initiative (W81XWH-06-1-0149). The MR investigations were performed at the Advanced Imaging Research Center, an NIH BRTP facility (P41RR02584) in conjunction with the Small Animal Imaging Research Program (NCI U24 CA126608).

### REFERENCES

- Tatum JL, Kelloff GJ, Gillies RJ, Arbeit JM, Brown JM, Chao KS, Chapman JD, Eckelman WC, Fyles AW, Giaccia AJ, Hill RP, Koch CJ, Krishna MC, Krohn KA, Lewis JS, Mason RP, Melillo G, Padhani AR, Powis G, Rajendran JG, Reba R, Robinson SP, Semenza GL, Swartz HM, Vaupel P, Yang D, Croft B, Hoffman J, Liu G, Stone H, Sullivan D. Hypoxia: importance in tumor biology, noninvasive measurement by imaging, and value of its measurement in the management of cancer therapy. *Int. J. Radiat. Biol.* 2006; **82**: 699–757.
- Fyles A, Milosevic M, Hedley D, Pintilie M, Levin W, Manchul L, Hill RP. Tumor hypoxia has independent predictor impact only in patients with node-negative cervix cancer. *J. Clin. Oncol.* 2002; **20**: 680–687.
- Fyles A, Milosevic M, Pintilie M, Syed A, Levin W, Manchul L, Hill RP. Long-term performance of interstitial fluid pressure and hypoxia as prognostic factors in cervix cancer. *Radiother. Oncol.* 2006; **80**: 132–137.
- Brizel DM, Sibly GS, Prosmitt LR, Scher RL, Dewhirst MW. Tumor hypoxia adversely affects the prognosis of carcinoma of the head and neck. *Int. J. Radiat. Oncol. Biol. Phys.* 1997; **38**: 285–289.
- Movsas B, Chapman JD, Hanlon AL, Horwitz EM, Greenberg RE, Stobbe C, Hanks GE, Pollack A. Hypoxic prostate/muscle  $pO_2$  ratio predicts for biochemical failure in patients with prostate cancer: preliminary findings. *Urology*, 2002; **60**: 634–639.
- Vaupel PW, Schlenger K, Knoop C, Höckel M. Oxygenation of human tumors: evaluation of tissue oxygen distribution in breast cancers by computerized  $O_2$  tension measurements. *Cancer Res.* 1991; **51**: 3316–3322.
- Evans SM, Judy KD, Dunphy I, Jenkins WT, Nelson PT, Collins R, Wileyto EP, Jenkins K, Hahn SM, Stevens CW, Judkins AR, Phillips P, Georger B, Koch CJ. Comparative measurements of hypoxia in human brain tumors using needle electrodes and EF5 binding. *Cancer Res.* 2004; **64**: 1886–1892.
- Gray L, Conger A, Ebert M, Hornsey S, Scott O. The concentration of oxygen dissolved in tissues at time of irradiation as a factor in radiotherapy. *Br. J. Radiol.* 1953; **26**: 638–648.
- O'Hara JA, Goda F, Demidenko E, Swartz HM. Effect on regrowth delay in a murine tumor of scheduling split-dose irradiation based on direct  $pO_2$  measurements by electron paramagnetic resonance oximetry. *Radiat. Res.* 1998; **150**: 549–556.
- Bourke VA, Zhao D, Gilio J, Chang C-H, Jiang L, Hahn EW, Mason RP. Correlation of radiation response with tumor oxygenation in the Dunning prostate R3327-AT1 tumor. *Int. J. Radiat. Oncol. Biol. Phys.* 2007; **67**: 1179–1186.
- Zhao D, Constantinescu A, Chang C-H, Hahn EW, Mason RP. Correlation of tumor oxygen dynamics with radiation response of the Dunning prostate R3327-HI tumor. *Radiat. Res.* 2003; **159**: 621–631.
- Kaanders JHAM, Wijffels KIEM, Marres HAM, Ljungkvist ASE, Pop LAM, van den Hoogen FJA, de Wilde PCM, Bussink J, Raleigh JA, van der Kogel AJ. Pimonidazole binding and tumor vascularity predict for treatment outcome in head and neck cancer. *Cancer Res* 2002; **62**: 7066–7074.
- Howe FA, Robinson SP, McIntyre DJ, Stubbs M, Griffiths JR. Issues in flow and oxygenation dependent contrast (FLOOD) imaging of tumours. *NMR Biomed.* 2001; **14**: 497–506.
- Baudelet C, Gallez B. Current issues in the utility of blood oxygen level dependent MRI for the assessment of modulations in tumor oxygenation. *Current Medical Imaging Reviews* 2005; **1**: 229–243.
- Dunn JF, O'Hara JA, Zaim-Wadghiri Y, Lei H, Meyerand ME, Grinberg OY, Hou H, Hoopes PJ, Demidenko E, Swartz HM. Changes in oxygenation of intracranial tumors with carbogen: a BOLD MRI and EPR oximetry study. *J. Magn Reson Imaging* 2002; **16**: 511–521.
- Kodibagkar VD, Wang X, Mason RP. Physical principles of quantitative nuclear magnetic resonance oximetry. *Front Biosci.* 2008; **13**: 1371–1384.
- Zhao D, Jiang L, Mason RP. Measuring changes in tumor oxygenation. *Methods Enzymol* 2004; **386**: 378–418.
- Robinson SP, Griffiths JR. Current issues in the utility of  $^{19}F$  nuclear magnetic resonance methodologies for the assessment of tumour hypoxia. *Philos. Trans. R. Soc. London B Biol. Sci.* 2004; **359**: 987–996.
- Kodibagkar VD, Cui W, Merritt ME, Mason RP. A novel  $^1H$  NMR approach to quantitative tissue oximetry using hexamethyldisiloxane. *Magn. Reson. Med.* 2006; **55**: 743–748.
- Haase A, Frahm J, Hancicke W, Matthaei D. H-1-Nmr chemical-shift selective (Chess) imaging. *Phys. Med. Biol.* 1985; **30**: 341–344.
- Hunjan S, Zhao D, Constantinescu A, Hahn EW, Antich PP, Mason RP. Tumor Oximetry: demonstration of an enhanced dynamic mapping procedure using fluorine-19 echo planar magnetic resonance imaging in the Dunning prostate R3327-AT1 rat tumor. *Int. J. Radiat. Oncol. Biol. Phys.* 2001; **49**: 1097–1108.
- Yu JX, Kodibagkar V, Cui W, Mason RP.  $^{19}F$ : a versatile reporter for non-invasive physiology and pharmacology using magnetic resonance. *Curr. Med. Chem.* 2005; **12**: 818–848.
- Mason RP. Non-invasive physiology:  $^{19}F$  NMR of perfluorocarbon. *Artif. Cells Blood Substit Immobil Biotechnol* 1994; **22**: 1141–1153.
- Barker BR, Mason RP, Bansal N, Peshock RM. Oxygen tension mapping by  $^{19}F$  echo planar NMR imaging of sequestered perfluorocarbon. *J. Magn Reson Imaging* 1994; **4**: 595–602.
- Mason RP, Rodbumrung W, Antich PP. Hexafluorobenzene: a sensitive  $^{19}F$  NMR indicator of tumor oxygenation. *NMR Biomed.* 1996; **9**: 125–134.
- Dardzinski BJ, Sotak CH. Rapid tissue oxygen tension mapping using  $^{19}F$  inversion-recovery echo-planar imaging of perfluoro-15-crown-5-ether. *Magn. Reson. Med.* 1994; **32**: 88–97.
- Hunjan S, Mason RP, Constantinescu A, Peschke P, Hahn EW, Antich PP. Regional tumor oximetry:  $^{19}F$  NMR spectroscopy of hexafluorobenzene. *Int. J. Radiat. Oncol. Biol. Phys.* 1998; **40**: 161–171.

28. Yu J-X, Cui W, Zhao D, Mason RP. Non-invasive physiology and pharmacology using  $^{19}\text{F}$  magnetic resonance. In *Fluorine and Health*, Tressaud A, Haufe G (eds). Elsevier B.V.: Amsterdam, 2008; 198–276.
29. Seiyama A, Shiga T, Maeda N. Temperature effect on oxygenation and metabolism of perfused rat hindlimb muscle. In *Oxygen Transport to Tissue XII*, Piiper J, Goldstick TK, Meyer M (eds). Plenum Press: New York, 1990; 541–547.
30. McKinley BA, Butler BD. Comparison of skeletal muscle  $\text{P-O}_2$ ,  $\text{P-CO}_2$ , and pH with gastric tonometric  $\text{P-CO}_2$  and pH in hemorrhagic shock. *Crit Care Med* 1999; **27**: 1869–1877.
31. Vahidi N, Clarkson RB, Liu KJ, Norby SW, Wu M, Swartz HM. *In Vivo* and *in vitro* EPR oximetry with fusinite: a new coal-derived, particulate EPR probe. *Magn. Res. Med.* 1994; **31**: 139–146.
32. Sostaric JZ, Pandian RP, Bratasz A, Kuppusamy P. Encapsulation of a highly sensitive EPR active oxygen probe into sonochemically prepared microspheres. *J. Phys. Chem. B* 2007; **111**: 3298–3303.
33. Yeh KA, Biade S, Lanciano RM, Brown DQ, Fenning MC, Babb JS, Hanks GE, Chapman JD. Polarographic needle electrode measurements of oxygen in rat prostate carcinomas: accuracy and reproducibility. *Int. J. Radiat. Oncol. Biol. Phys.* 1995; **33**: 111–118.
34. Zhao D, Constantinescu C, Hahn EW, Mason RP. Differential oxygen dynamics in two diverse Dunning prostate R3327 rat tumor sublines (MAT-Lu and HI) with respect to growth and respiratory challenge. *Int. J. Radiat. Oncol. Biol. Phys.* 2002; **53**: 744–756.
35. Zhao D, Ran S, Constantinescu A, Hahn EW, Mason RP. Tumor oxygen dynamics: correlation of *in vivo* MRI with histological findings. *Neoplasia* 2003; **5**: 308–318.
36. Eidelberg D, Johnson G, Barnes D, Tofts PS, Delpy D, Plummer D, McDonald WI.  $^{19}\text{F}$  NMR imaging of blood oxygenation in the brain. *Magn. Reson. Med.* 1988; **6**: 344–352.
37. Mason RP, Antich PP, Babcock EE, Constantinescu A, Peschke P, Hahn EW. Non-invasive determination of tumor oxygen tension and local variation with growth. *Int. J. Radiat. Oncol. Biol. Phys.* 1994; **29**: 95–103.
38. Matsumoto K, Bernardo M, Subramanian S, Choyke P, Mitchell JB, Krishna MC, Lizak MJ. MR assessment of changes of tumor in response to hyperbaric oxygen treatment. *Magn. Reson. Med.* 2006; **56**: 240–246.
39. Zaharchuk G, Busse RF, Rosenthal G, Manley GT, Glenn OA, Dillon WP. Noninvasive oxygen partial pressure measurement of human body fluids *in vivo* using magnetic resonance imaging. *Acad Radiol* 2006; **13**: 1016–1024.
40. Cassidy SL, Dotti A, Kolesar GB, Dochterman LW, Meeks RG, Chevalier HJ. Hexamethyldisiloxane: a 13-week subchronic whole-body vapor inhalation toxicity study in Fischer 344 rats. *Int. J. Toxicol.* 2001; **20**: 391–399.
41. Dobrev ID, Reddy MB, Plotzke KP, Varaparth S, McNett DA, Durham J, Andersen ME. Closed-chamber inhalation pharmacokinetic studies with hexamethyldisiloxane in the rat. *Inhal. Toxicol.* 2003; **15**: 589–617.
42. Varaparth S, McMahon JM, Plotzke KP. Metabolites of hexamethyldisiloxane and decamethylcyclopentasiloxane in Fischer 344 rat urine: a comparison of a linear and a cyclic siloxane. *Drug Metab Dispos* 2003; **31**: 206–214.
43. Parent RA. Acute toxicity data submissions. *Int. J. Toxicol.* 2000; **19**: 331–373.

## Vascular Imaging of Solid Tumors in Rats with a Radioactive Arsenic-Labeled Antibody that Binds Exposed Phosphatidylserine

Marc Jennewein,<sup>1,2</sup> Matthew A. Lewis,<sup>2,3</sup> Dawen Zhao,<sup>2</sup> Edward Tsyganov,<sup>2</sup> Nikolai Slavine,<sup>2</sup> Jin He,<sup>3,4</sup> Linda Watkins,<sup>3,4</sup> Vikram D. Kodibagkar,<sup>2</sup> Sean O'Kelly,<sup>6</sup> Padmakar Kulkarni,<sup>2</sup> Peter P. Antich,<sup>2</sup> Alex Hermanne,<sup>5</sup> Frank Rösch,<sup>1</sup> Ralph P. Mason,<sup>2,3</sup> and Philip E. Thorpe<sup>3,4</sup>

**Abstract Purpose:** We recently reported that anionic phospholipids, principally phosphatidylserine, become exposed on the external surface of vascular endothelial cells in tumors, probably in response to oxidative stresses present in the tumor microenvironment. In the present study, we tested the hypothesis that a chimeric monoclonal antibody that binds phosphatidylserine could be labeled with radioactive arsenic isotopes and used for molecular imaging of solid tumors in rats.

**Experimental Design:** Bavixumab was labeled with <sup>74</sup>As ( $\beta^+$ ,  $T_{1/2}$  17.8 days) or <sup>77</sup>As ( $\beta^-$ ,  $T_{1/2}$  1.6 days) using a novel procedure. The radionuclides of arsenic were selected because their long half-lives are consistent with the long biological half lives of antibodies *in vivo* and because their chemistry permits stable attachment to antibodies. The radiolabeled antibodies were tested for the ability to image subcutaneous Dunning prostate R3227-AT1 tumors in rats.

**Results:** Clear images of the tumors were obtained using planar  $\gamma$ -scintigraphy and positron emission tomography. Biodistribution studies confirmed the specific localization of bavixumab to the tumors. The tumor-to-liver ratio 72 h after injection was 22 for bavixumab compared with 1.5 for an isotope-matched control chimeric antibody of irrelevant specificity. Immunohistochemical studies showed that the bavixumab was labeling the tumor vascular endothelium.

**Conclusions:** These results show that radioarsenic-labeled bavixumab has potential as a new tool for imaging the vasculature of solid tumors.

Imaging offers noninvasive perspective on tumor development and therapy, providing information on receptor expression, targeting, and drug pharmacokinetics. Imaging technologies include positron emission tomography (PET), single-photon

emission computed tomography, MRI, ultrasound, and optical imaging, as reviewed extensively elsewhere (1, 2). Nuclear medicine approaches are particularly relevant because extremely low concentrations of tracer/reporter are permissible. Several radionuclides are in clinical use, and many more are under development (3–5). However, many isotopes decay rapidly, limiting shelf life and preventing investigation of long-term biological phenomena. A particular problem arises with antibodies, which usually have a long biological half life and do not reach optimal target to background selectivity for several days. For PET, common radionuclides, such as <sup>64</sup>Cu (18%  $\beta^+$  positron branching,  $T_{1/2}$  12.7 h) or <sup>86</sup>Y (32%  $\beta^+$ ,  $T_{1/2}$  17.8 h) have too-short half-lives for following antibody localization, whereas <sup>124</sup>I (24%  $\beta^+$ ,  $T_{1/2}$  4.18 days) has a suitable  $T_{1/2}$  but undergoes metabolic dehalogenation and release of iodine.

Arsenic radioisotopes include long-lived positron emitters having favorable characteristics for PET: <sup>71</sup>As ( $T_{1/2}$  64 h, 30%  $\beta^+$ , 104 keV average kinetic energy of the positrons), <sup>72</sup>As ( $T_{1/2}$  26 h, 88%  $\beta^+$ , 1.024 keV), and <sup>74</sup>As ( $T_{1/2}$  17.8 days, 29%  $\beta^+$ , 128 keV). Other arsenic isotopes are high-energy  $\beta^-$  emitters that could potentially be used for tumor therapy: <sup>77</sup>As ( $T_{1/2}$  38.8 h,  $\bar{E}_{\beta^-}$  226 keV) and <sup>76</sup>As ( $T_{1/2}$  26.3 h,  $\bar{E}_{\beta^-}$  1.068 keV). The decay characteristics of the arsenic isotopes that are most relevant for imaging or therapy are presented in Supplementary Table S1. <sup>74</sup>As was used in some of the earliest radionuclide imaging studies for the development of PET, at that time, called positrocephalography (6). However, inefficient isotope production, difficulty in isolating pure nuclides, and lack of

**Authors' Affiliations:** <sup>1</sup>Institute of Nuclear Chemistry, Johannes Gutenberg-University of Mainz, Mainz, Germany; <sup>2</sup>Cancer Imaging Program, Department of Radiology, <sup>3</sup>Simmons Cancer Center, and <sup>4</sup>Department of Pharmacology and Hamon Cancer Center, University of Texas Southwestern Medical Center at Dallas, Dallas, Texas; <sup>5</sup>VUB Cyclotron, University of Brussels, Brussels, Belgium; and <sup>6</sup>Department of Nuclear Engineering, University of Texas at Austin, Pickle Research Campus, Austin, Texas

Received 6/19/07; revised 10/25/07; accepted 11/13/07.

**Grant support:** Gillson Longenbaugh Foundation, National Cancer Institute Specialized Programs of Research Excellence lung cancer research grant CA70907, sponsored research agreement with Peregrine Pharmaceuticals, Inc., Boehringer Ingelheim Fonds for Basic Research in Biomedicine, Deutsche Forschungsgemeinschaft grant Ro 985/17, NoE 'European Molecular Imaging Laboratories', DOD Prostate IDEA awards PC050766 (W81XWH-06-1-0149) and PC050301 (W81XWH-06-1-0050), and National Cancer Institute Pre-ICMIC P20 CA086334 and SAIRP U24 CA126608.

The costs of publication of this article were defrayed in part by the payment of page charges. This article must therefore be hereby marked *advertisement* in accordance with 18 U.S.C. Section 1734 solely to indicate this fact.

**Note:** MRI was done at the Advanced Imaging Research Center, an NIH BTRP facility P41-RR02584.

**Requests for reprints:** Philip E. Thorpe, Department of Pharmacology and Simmons and Hamon Cancer Centers, University of Texas Southwestern Medical Center at Dallas, 2201 Inwood Road NC7.304, Dallas, Texas 75390-8794. Phone: 214-648-1499; Fax: 214-648-1613; E-mail: Philip.Thorpe@utsouthwestern.edu.

© 2008 American Association for Cancer Research.

doi:10.1158/1078-0432.CCR-07-1516

effective derivatization processes handicapped the exploitation of arsenic isotopes. Radiochemistry has now evolved, and several isolation procedures for arsenic isotopes have been reported. Most recently, Jennewein and Rösch developed efficient methods for isolating pure radionuclides from irradiated GeO<sub>2</sub> targets on the basis of a solid phase extraction system (7, 8). Moreover, Jennewein and Rösch proposed chemistry for the effective labeling of biologically relevant molecules, as we have now exploited.

Bavituximab, a chimeric antibody targeting exposed vascular phosphatidylserine, was chosen to develop the labeling procedure and show the first *in vivo* use of arsenic isotopes for PET imaging of solid tumors. Bavituximab binds to phosphatidylserine by stabilizing a complex of two  $\beta$ -glycoprotein I molecules attached to phosphatidylserine on the cell surface (9–12). Phosphatidylserine is normally tightly segregated to the internal surface of the plasma membrane in most cell types, including the vascular endothelium (10, 11, 13, 14). Phosphatidylserine asymmetry is maintained by ATP-dependent aminophospholipid translocases (Mg<sup>2+</sup>-ATPase) that catalyze the transport of aminophospholipids from the external to the internal leaflet of the plasma membrane (15). Loss of phosphatidylserine asymmetry occurs during apoptosis (16), necrosis (17), cell activation (18), and transformation (19), resulting in the exposure of phosphatidylserine on the external surface of the cells. Phosphatidylserine exposure occurs when the aminophospholipid translocases become inhibited (20) or when transporters, such as scramblase (21) and floppases (22), become activated by Ca<sup>2+</sup> fluxes into the cytosol (23, 24).

We previously showed that anionic phospholipids become exposed on the vascular endothelium of blood vessels in mice bearing various types of solid tumors probably in response to oxidizing stresses in the tumor (10, 11). There was no detectable exposure on vascular endothelium in normal tissues, including the ovary, a site of physiologic angiogenesis, and the pancreas, a site of high vascular permeability. Phosphatidylserine is one of the most specific markers of tumor vasculature yet discovered. The murine version of bavituximab, 3G4, retards tumor growth in multiple rodent models by stimulating host cells to bind to and destroy tumor blood vessels. Bavituximab is currently in phase I clinical trials in patients with various solid tumors.<sup>7</sup> Despite its proven ability to target tumor endothelium, bavituximab has not yet been explored as an imaging agent. The vascular location of phosphatidylserine ensures ready access by radiolabeled antibody in the blood. Imaging techniques could not only enable the detection of tumors and their metastases, but also verify the presence of antigen before bavituximab therapy.

In the present study, we tested the hypothesis that bavituximab can be labeled with radioactive arsenic isotopes and used for vascular targeting and molecular imaging of solid tumors in rats. Doses of bavituximab that are 10-fold below the doses that have significant vascular damaging activity were used (14) to prevent occlusion of tumor vasculature from impeding effective imaging. Clear tumor imaging was obtained by planar  $\gamma$ -scintigraphy and PET.

## Materials and Methods

**Antibodies.** Bavituximab was provided by Peregrine Pharmaceuticals, Inc. Bavituximab is a chimeric antibody composed of the Fv regions of the mouse antibody 3G4 (14) and the constant regions of human IgG1. Bavituximab binds to phosphatidylserine through a cofactor protein,  $\beta$ 2-glycoprotein I. Bavituximab recognizes rat  $\beta$ 2-glycoprotein I as strongly as it does human  $\beta$ 2-glycoprotein I, avoiding the need for supplementation with exogenous human  $\beta$ 2-glycoprotein I, which is necessary in the mouse (14). Bavituximab binds to human  $\beta$ 2-glycoprotein I with an affinity of  $1.7 \times 10^{-8}$  mol/L (monovalent interaction) and an avidity of  $\sim 10^{10}$  mol/L (divalent interaction) in Biacore experiments.

Hamster anti-mouse CD31 monoclonal antibody was from BD PharMingen. Secondary antibodies were from Jackson ImmunoResearch Lab. Rituximab (monoclonal antibody Thera, CD20) was purchased from Roche.

**Isotopes.** <sup>74</sup>As for PET imaging was produced by <sup>nat</sup>Ge(*p,xn*)<sup>74</sup>As reaction ( $E_p = 20$  MeV, 3 h irradiation at 15  $\mu$ A), giving a yield of  $\sim 370$  MBq. <sup>77</sup>As for scintigraphy was produced in a no-carrier-added (nca) state via the <sup>76</sup>Ge(*n, $\gamma$* )<sup>77</sup>Ge,  $T_{1/2}$  11.30 h  $h \rightarrow \beta^- \rightarrow$  <sup>77</sup>As processes in a TRIGA reactor ( $\Phi = 4.0 \times 10^{13}$  n/cm<sup>2</sup>·s).

**Radiochemical separations.** Nuclear reactions were typically done on 100 mg of <sup>nat</sup>GeO<sub>2</sub> (99.9999% grade, PURA TREM, Strem Chemicals, Inc.). Irradiated germanium oxide targets were dissolved in 5 mL HF<sub>conc.</sub> and extracted as described in detail previously (7), providing nca [<sup>\*</sup>As]AsI<sub>3</sub> fixed to the solid phase of the extraction cartridge (Varian BOND ELUT ENV solid phase extraction cartridges with a sorbent mass of 50 mg and a volume of 1 mL). Excess HF<sub>conc.</sub> was removed with a high-pressure nitrogen flow over the cartridge for 5 min. When required for labeling, nca [<sup>\*</sup>As]AsI<sub>3</sub> was eluted with 500  $\mu$ L ethanol and concentrated to 50  $\mu$ L under a gentle N<sub>2</sub> flow. The radioarsenic separation yield and efficacy of nca [<sup>\*</sup>As]AsI<sub>3</sub> was >90%.

**Antibody conjugation and testing.** Antibodies were SATA-modified according to the protocol of Pierce Endogen (25). Deprotection of the sulfhydryl groups of the monoclonal antibody derivative using hydroxylamine was done directly before the labeling. The number of free thiol groups per antibody molecule was measured using Ellman's reagent and by comparison with cysteine-based standards. Thiolated antibody (100  $\mu$ g) in PBS (3 mL, pH 7.5) was combined with the nca [<sup>\*</sup>As]AsI<sub>3</sub> solution at 37°C for 30 min. [<sup>\*</sup>As]AsI<sub>3</sub> couples to one SH functionality with elimination of HI as illustrated in Fig. 1. Quality control of the antibody labeling was done by HPLC, using an Agilent 1100 Series HPLC system, with an LDC/Milton Roy UV monitor III at 254 nm and a 'Gabi' NaI radiation monitor from Raytest. The HPLC column was a Bio-Silect Sec 250-5, 300  $\times$  7.8 mm and PBS + 0.01 mol/L NaN<sub>3</sub> was used as solvent at a flow of 0.8 mL/min. Retention time of the [<sup>\*</sup>As]SATA labeled antibodies was  $11.5 \pm 0.5$  min. To keep the thiols from forming disulfide bridges, all solutions were kept out of contact with air and contained 1 mmol/L EDTA.

**In vitro stability.** The radioarsenic-labeled bavituximab was tested for possible transfer of radioarsenic to proteins present in blood plasma. This was done by incubating the labeled antibody in fetal bovine serum and examining the mixture by HPLC at various time points up to 72 h. Radioarsenic-labeled bavituximab (10  $\mu$ g) in PBS (50  $\mu$ L) was added to undiluted fetal bovine serum (500  $\mu$ L) and incubated at 37°C. Samples (50  $\mu$ L) were taken at 30 min, 24 h, 48 h, and 72 h, diluted with 200  $\mu$ L water, and examined by HPLC.

**Binding of bavituximab antibody to plastic-immobilized phospholipids.** Phospholipids were dissolved in *n*-hexane to a concentration of 50  $\mu$ g/mL. One hundred microliters of this solution were added to wells of 96-well microtiter plates. After evaporation of the solvent in air, the plates were blocked for 2 h with 1% bovine serum albumin diluted in PBS (binding buffer). Bavituximab was diluted in the binding buffer containing 10% fetal bovine serum at an initial concentration of 33 nmol/L. Serial 2-fold dilutions were prepared in the plates

<sup>7</sup> Peregrine Pharmaceuticals, Inc; see <http://www.clinicaltrials.gov/ct/show/nct00129337>.

(100  $\mu\text{L}/\text{well}$ ). The plates were then incubated for 1 h at room temperature. After washing with PBS, horseradish peroxidase goat anti-human IgG (diluted 1:2,000) was used to detect bavituximab. Secondary reagents were detected by using chromogenic substrate *O*-phenyldiamine followed by reading plates at 490 nm using a microplate reader (Molecular Devices). Binding of [ $^{77}\text{As}$ ]bavituximab to phosphatidylserine-coated plates was determined using unmodified bavituximab as the positive control and [ $^{77}\text{As}$ ]rituximab as the negative control. The concentrations of [ $^{77}\text{As}$ ]bavituximab and unmodified bavituximab that gave half-maximal binding were determined. Because the association rate of bavituximab with phosphatidylserine on the plate is rapid and its dissociation is negligible over the time course of the experiment, the half-maximal binding concentrations allow the antigen-binding capacities of the labeled and unmodified antibodies to be compared under conditions that approximate equilibrium.

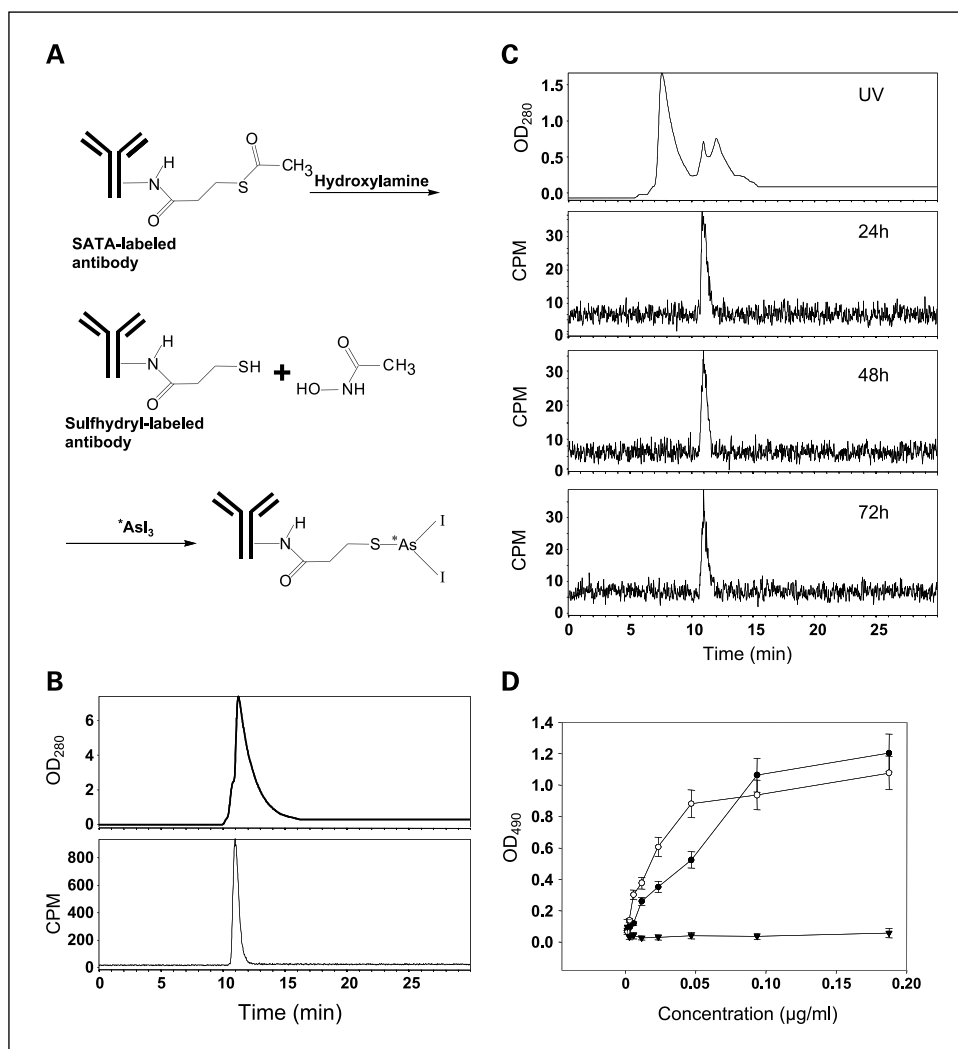
**Growth of tumors.** All experiments were conducted in accordance with recommendations of The University of Texas System Institutional Animal Care and Use Committee. A Dunning prostate R3327-AT1 tumor (originally provided by Dr. Peter Peschke, German Cancer Center) was excised from a donor animal (26, 27). Small pieces were implanted s.c. into the left thigh of male Copenhagen rats (Charles River) and allowed to grow to a size of 15 to 25 mm diameter.

**Biodistribution and planar imaging studies.** Three animals each were injected with [ $^{74}\text{As}$ ]bavituximab or with [ $^{74}\text{As}$ ]rituximab in PBS (5 MBq in 500  $\mu\text{L}$ ) into a tail vein. The animals were sedated using

isoflurane (Baxter Healthcare) and imaged on a  $25.2 \times 30.3$  cm phosphor imaging plate (Fuji CR ST-VN, Fuji Photo Film). The photostimulable plates were read on a Molecular Dynamics Storm (Amersham Biosciences) scanner and regions of interest drawn around the tumors and upper body for quantification. In a second study, four animals injected with 3 MBq of [ $^{77}\text{As}$ ]bavituximab or [ $^{77}\text{As}$ ]rituximab were imaged at 48 and 72 h using a 30-min exposure time. Prior studies have established that [ $^{74}\text{As}$ ]bavituximab and [ $^{77}\text{As}$ ]bavituximab have identical pharmacologic variables, i.e., independent of the isotope of arsenic. In a further study, rats were injected with 3 MBq of [ $^{77}\text{As}$ ]bavituximab or [ $^{77}\text{As}$ ]rituximab and were sacrificed without exsanguination 48 or 72 h later. Tumors were excised and frozen, and 1-mm sections were cut. Tumor sections were autoradiographed with exposure times of 12 h for [ $^{77}\text{As}$ ]bavituximab and 48 h for [ $^{77}\text{As}$ ]rituximab to visualize the distribution of radioactivity within the tumors.

**PET studies.** Four animals each were injected with 10 MBq of [ $^{74}\text{As}$ ]bavituximab or [ $^{74}\text{As}$ ]rituximab in 500  $\mu\text{L}$  of PBS (pH 7.4, 1 mmol/L EDTA) via a tail vein. The animals were anesthetized with isoflurane and imaged over 2 h after 24, 48, and 72 h using a small animal PET system built at University of Texas Southwestern (28, 29). The images were reconstructed using the maximum likelihood - expectation maximization (ML - EM) algorithm for three-dimensional reconstruction (28) After 72 h, the animals were sacrificed by exsanguination and perfusion via cardiac puncture under general

**Fig. 1.** *A*, reaction scheme for the labeling of SATA-modified antibody with radioactive arsenic isotopes. *B*, quality control of bavituximab labeling with radioactive arsenic. After a labeling time of 30 min, a sample of [ $^{74}\text{As}$ ]bavituximab (20  $\mu\text{L}$ ) was resolved on a size-exclusion column for radio-HPLC. The UV spectrum (*top*) and corresponding radioactivity progression (*bottom*) confirm the absence of aggregates and of free  $^{74}\text{As}$ . Labeling yield is  $>99.9\%$ . *C*, *in vitro* stability of [ $^{74}\text{As}$ ]bavituximab. [ $^{74}\text{As}$ ]bavituximab was incubated in undiluted fetal bovine serum for 24, 48, and 72 h. Size exclusion radio-HPLC was done. The UV spectrum (*top*) shows a typical fetal bovine serum profile because the amount of [ $^{74}\text{As}$ ]bavituximab is too small to detect. *Bottom*, graphs show the corresponding radioactivity peak. Aggregates and breakdown products were not observed, indicating that the product is stable in serum. *D*, immunoreactivity. ELISA was used to analyze the immunoreactivity of [ $^{77}\text{As}$ ]bavituximab ( $\bullet$ ). Unlabeled and unmodified bavituximab was used as the positive control ( $\circ$ ) and [ $^{77}\text{As}$ ]rituximab as the negative control ( $\blacktriangledown$ ). Little or no reduction of immunoreactivity was detected after SATA modification and radioarsenic labeling.



anesthesia, and major organs and tumors were collected and their radioactivity measured in a Gamma counter.

**MRI.** T1-weighted spin-echo MR images were obtained from rats with size-matched tumors for anatomic comparison. The images were acquired with TR/TE of 450 ms:14 ms. The acquisition matrix was 128 × 256 zero-filled to 512 × 1,024 with field of view 10 × 20 cm and a slice thickness of 1 mm.

**Detection of localized bavituximab in tumor-bearing rats in vivo.** Groups of two male Copenhagen rats (200 g weight) bearing AT1 tumors (s.c., 15 mm diameter) were injected i.v. with 1 mg bavituximab or control antibody (rituximab). Twenty four hours later, rats were anesthetized and their blood circulation was perfused with heparinized saline to clear it of free antibody, as described above. Organs and tumors were removed and snap-frozen for preparation of cryosections. Sections were fixed with 4% paraformaldehyde in PBS and blocked with PBS containing 1% bovine serum albumin. To prevent loss of phospholipids during slide processing, detergents and organic solvents were omitted from blocking and washing buffers. Chimeric IgG was detected using biotinylated goat anti-human IgG followed by Cy2-streptavidin. Vascular endothelium was detected by mouse anti-rat CD31 antibody followed by Cy3-goat anti-mouse antibody (minimally reactive with rat serum). Tumor sections derived from rats injected with rituximab served as negative controls. Single images, taken with appropriate filters for Cy2 (green) and Cy3 (red) fluorescence, respectively, were captured by digital camera and transferred to a computer. Images of 10 random fields (0.317 mm<sup>2</sup>/field) were merged with the aid of Metaview software. When bavituximab was bound to tumor endothelium, the green and red fluorescence often merged to give a yellow color. The percentage of vessels with localized bavituximab was calculated.

## Results

<sup>74</sup>As and <sup>77</sup>As were produced, radiochemically separated, and transformed into the labeling synthon \*AsI<sub>3</sub>. Isotopes were chosen depending on the goal of each study, so that <sup>74</sup>As was used for *ex vivo* organ distribution, whole-body planar imaging (*in vivo* and *ex vivo*), and *in vivo* PET imaging. <sup>77</sup>As was used to develop the radiochemistry and labeling procedures and used to label bavituximab for whole-body planar imaging *in vivo* and biodistribution.

Bavituximab was modified with SATA to introduce an average of 3.5 free thiol groups per molecule of antibody (Fig. 1A). Arsenic has a high affinity for sulfur, and AsI<sub>3</sub> is able to bind covalently to sulfhydryl groups (7). \*AsI<sub>3</sub> conjugation to the SATA-modified antibodies was achieved quantitatively (Fig. 1B). The specific activity of the [\*As]labeled antibodies was >100 GBq/μmol. Incubation in serum for up to 72 h did not cause release of radioarsenic from the labeled monoclonal antibody or formation of antibody fragments (Fig. 1C). Complexes of bavituximab and β2-glycoprotein I were not observed, probably because the complex is not stable in the absence of an anionic phospholipid surface upon which to dimerize. Immunoreactivity of the labeled bavituximab was verified by ELISA. Little or no loss of phosphatidylserine-binding activity was observed after SATA-modification and subsequent labeling with nca [<sup>77</sup>As] AsI<sub>3</sub> (Fig. 1D). The concentration of [<sup>77</sup>As]bavituximab giving half-maximal binding was less than twice that for unmodified bavituximab, indicating that the labeling procedure had caused less than a 2-fold reduction in the antigen-binding capacity of the antibody.

Rats bearing Dunning R3227-AT1 prostate tumors of ~15 mm in diameter were injected i.v. with [<sup>74</sup>As]bavituximab or

with the isotype-matched control antibody, [<sup>74</sup>As]rituximab. The radioactivity present in various organs was measured 48 and 72 h after injection. These time points were selected because they gave good tumor localization in the imaging studies below. Tumor to normal tissue ratios were highest for bavituximab at 72 h after injection, consistent with the imaging results. Tumor-to-liver and tumor-to-muscle ratios at 72 h were 22 and 470, respectively (Fig. 2A and B). Bavituximab localized to tumors to a greater extent than did the control antibody rituximab. The ratios of bavituximab to rituximab were 28 and 52 at 48 and 72 h, respectively (Fig. 2C). The percentage of

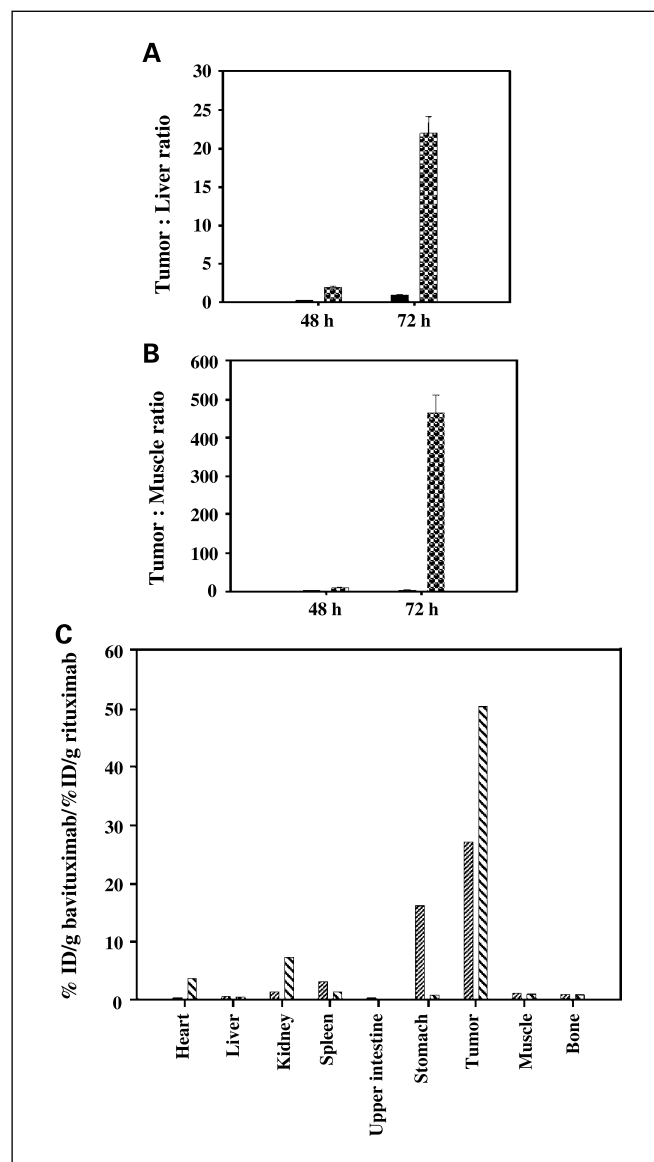


**Fig. 2.** Biodistribution. Dunning prostate R3227-AT1 tumor-bearing rats were injected with 185 kBq of [<sup>74</sup>As]bavituximab or [<sup>74</sup>As]rituximab i.v. Groups of four animals were sacrificed by exsanguination and perfusion 48 or 72 h after injection. **A**, tumor-to-liver ratios for rats sacrificed after 48 and 72 h after injection with [<sup>74</sup>As]rituximab (black) or [<sup>74</sup>As]bavituximab (dots). **B**, corresponding tumor to muscle ratios. **C**, specific localization of bavituximab/rituximab in major organs after 48 h (narrow hatched) and 72 h (broad hatched). Specific localization is calculated as the ratio of the % ID/gram for [<sup>74</sup>As]bavituximab to the % ID/gram for [<sup>74</sup>As]rituximab in tumor and normal tissues. At 72 h, the uptake of bavituximab was significantly higher in tumor than liver or muscle ( $P < 0.001$ ).

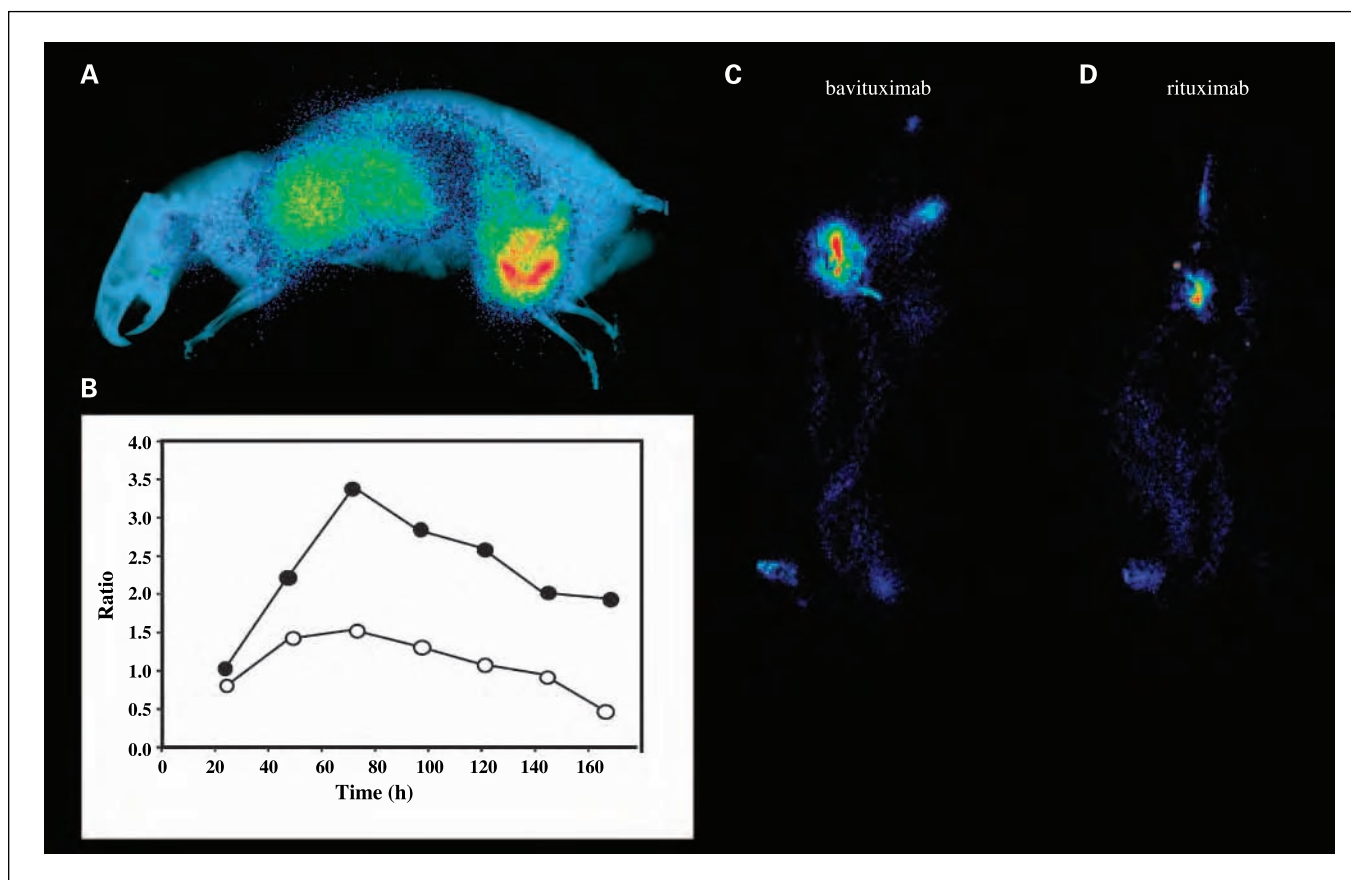


**Fig. 3.** Whole-body planar scintigraphy of Dunning prostate R3227-AT1 tumor-bearing rats. *A*, rats bearing ~20 mm diameter tumors were injected i.v. with 5 MBq of [<sup>74</sup>As]bavituximab. The rats were imaged on a phosphor plate at various time points after injection. Representative image 72 h after injection. The image is overlaid on an X-ray picture to provide anatomic correlation. *B*, ratio of uptake of [<sup>74</sup>As]bavituximab in tumor versus upper organs (liver, lung, heart) at various time points after injection. ●, outer tumor regions; ○, entire tumor. At 24 h after injection, no obvious contrast was observed, but at 48 h, the tumor became clearly visible and by 72 h, the tumor-to-organ ratio was the highest. *C-D*, scintigraphy of rats injected with 3 MBq [<sup>77</sup>As]bavituximab or [<sup>77</sup>As]rituximab (negative control). Images acquired with 30 min of exposure time at 72 h. Eight-fold higher uptake of bavituximab than of the control antibody was observed in the tumor.

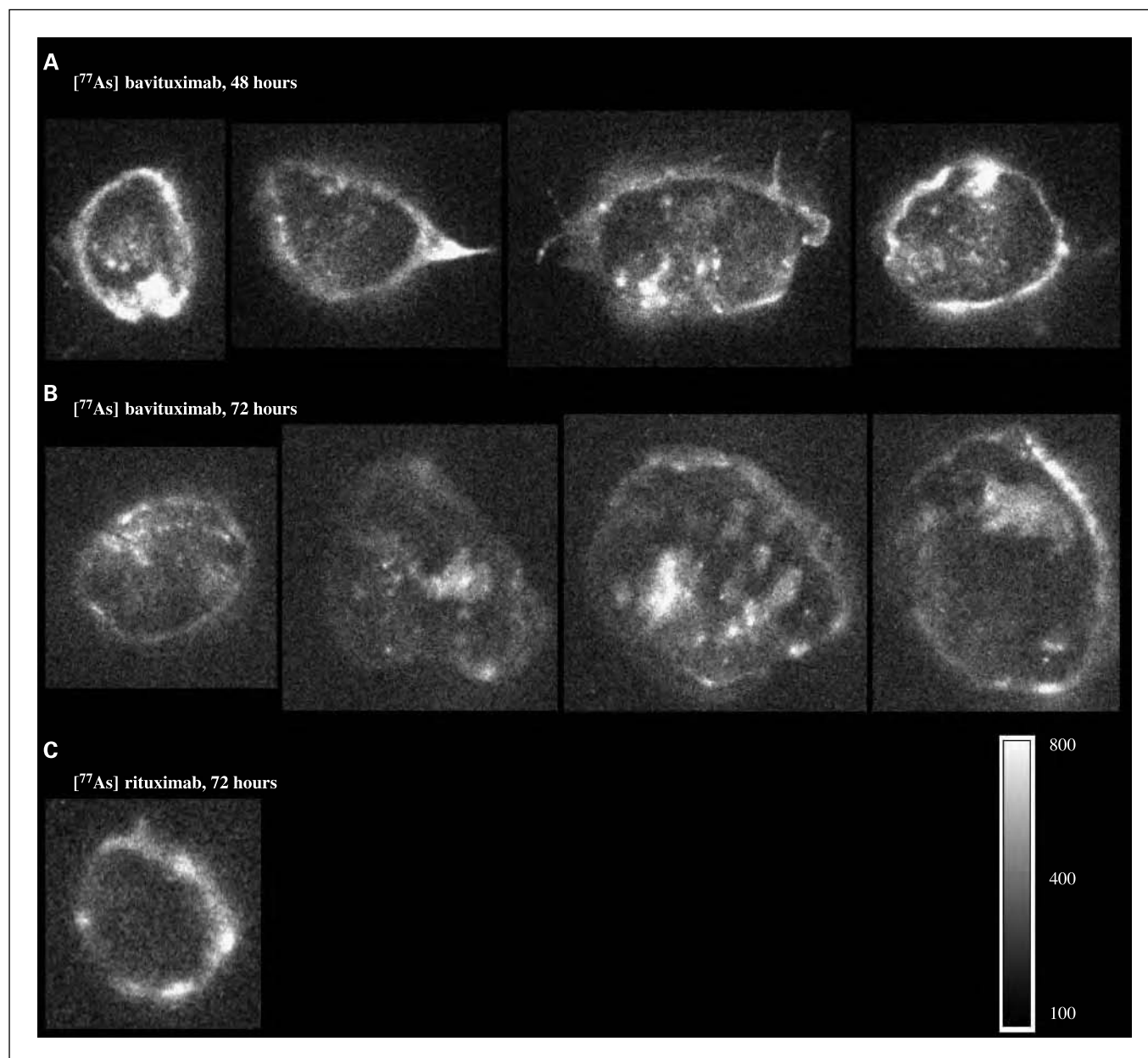
the injected dose per gram of tumor was 0.25 and 0.65 for [<sup>74</sup>As]bavituximab at 48 and 72 h, respectively. This level of localization is respectable given the inverse relationship between animal weight and % ID/gram in different species. Significant uptake of radioactivity was observed in the stomach 48 h after injection of [<sup>74</sup>As]bavituximab but had decreased by 72 h. In most organs (heart, liver, kidney, muscle, bone), the two antibodies showed similar low uptake. Uptake of [<sup>74</sup>As]labeled bavituximab and rituximab was observed in the spleen.

Figure 3A shows the whole-body scintigraphy of a representative rat imaged at 72 h after injection with [<sup>74</sup>As]bavituximab. Figure 3B compares the radioactivity in the tumor to that in the upper organs (liver, lung, heart) at various time points after injection of [<sup>74</sup>As]bavituximab. At 24 h, the tumor was barely distinguishable because of the high body background. At 48 h, the tumor was clearly localized, but some signal attributable to blood pool was observed in the upper organs. At 72 h, labeled bavituximab had substantially cleared from the blood and antibody localization to the tumor was most visible. Thereafter, tumor to background ratios declined. Images are also shown for rats injected with [<sup>77</sup>As]bavituximab or [<sup>77</sup>As]rituximab (Fig. 3C and D) and imaged 72 h after injection. Relatively little [<sup>77</sup>As]rituximab (about one-eighth as much) localized to the

tumor compared with [<sup>77</sup>As]bavituximab, showing that the localization of [<sup>77</sup>As]bavituximab was antigen-specific.

Distribution of radioactivity within the tumor was heterogeneous. Slices of tumors were examined by autoradiography (Fig. 4). Extensive localization of [<sup>77</sup>As]bavituximab was observed in the tumor periphery and throughout the central regions, although quite heterogeneously. For rituximab, activity was limited to the tumor periphery. PET images from a three-dimensional data set of a tumor-bearing rat obtained 48 h after injection of [<sup>74</sup>As]bavituximab again showed strong localization to the tumor periphery with similar heterogeneity of activity in central regions (Fig. 5).

Frozen sections of tumor and normal tissues were stained for the presence of human immunoglobulin to identify the cells to which the bavituximab had localized. Sections were counterstained with anti-rat CD31 to detect vascular endothelium (Fig. 6). The images were merged. Coincidence of staining between localized bavituximab and CD31 indicated specific localization of bavituximab to tumor endothelium (Fig. 6). Coincident staining was yellow, unless dominated by a particularly intense green or red fluorescence in that region. Labeled vessels were visible in all regions of the tumors with an average of  $40 \pm 10\%$  labeled vessels. Labeled vessels were particularly abundant in and around regions of necrosis. Larger



**Fig. 4.** Autoradiography of excised tumor sections. *A* and *B*, autoradiographs of 1-mm sections of Dunning prostate R3227-AT1 tumors from rats 48 or 72 h after injection with [<sup>77</sup>As] bavituximab. Localization of bavituximab was observed in the tumor periphery and heterogeneously throughout the tumor core. *C*, [<sup>77</sup>As] rituximab showed relatively little accumulation in the tumor, particularly in the central regions. The autoradiograph was exposed four times longer with [<sup>77</sup>As] rituximab to visualize the distribution. Scale shows arbitrary storage phosphor units.

vessels sometimes had regions where the vascular endothelium was positive for localized bavituximab and other regions where it was not, showing heterogeneity of phosphatidylserine exposure within a single vessel. Regions where bavituximab had leaked into the tumor interstitium were also visible around the endothelium of some vessels. Nonvascular staining of dead and dying tumor cells in and around necrotic tumor regions was only occasionally observed. The antigen specificity of bavituximab localization to vessels was confirmed by the lack of endothelial cell staining in tumors from rats injected with rituximab. Localization of bavituximab to vascular endothelium in normal tissues was not detectable in rat heart, lung, liver, pancreas, kidney, spleen, brain, and testis.

## Discussion

This study shows the feasibility of using arsenic radioisotopes to label a monoclonal antibody directed against anionic phospholipids on the surface of tumor vascular endothelium. Tumor selective targeting was observed *in vivo* and confirmed by biodistribution analysis and histology.

The two isotopes we selected for the present studies were <sup>74</sup>As, a potential clinical PET imaging isotope, and <sup>77</sup>As, a potential therapeutic isotope. <sup>74</sup>As ( $\beta^+$ ,  $T_{1/2}$  17.8 days) has a long half life that allows imaging several days after administration of labeled antibody. Optimal tumor imaging in humans is often achieved 3 days or more after administration of a

labeled antibody, when the levels of free antibody have declined relative to those specifically bound or retained by the tumor (30, 31).  $^{77}\text{As}$  ( $\beta^-$ ,  $T_{1/2}$  38.8) has a high energy  $\beta^-$  emission suitable for antitumor therapy. Both isotopes, like other isotopes of arsenic, can be attached through stable covalent linkages to antibodies. In addition, arsenic does not accumulate in the thyroid or undergo transchelation to metal-binding blood and tissue proteins.

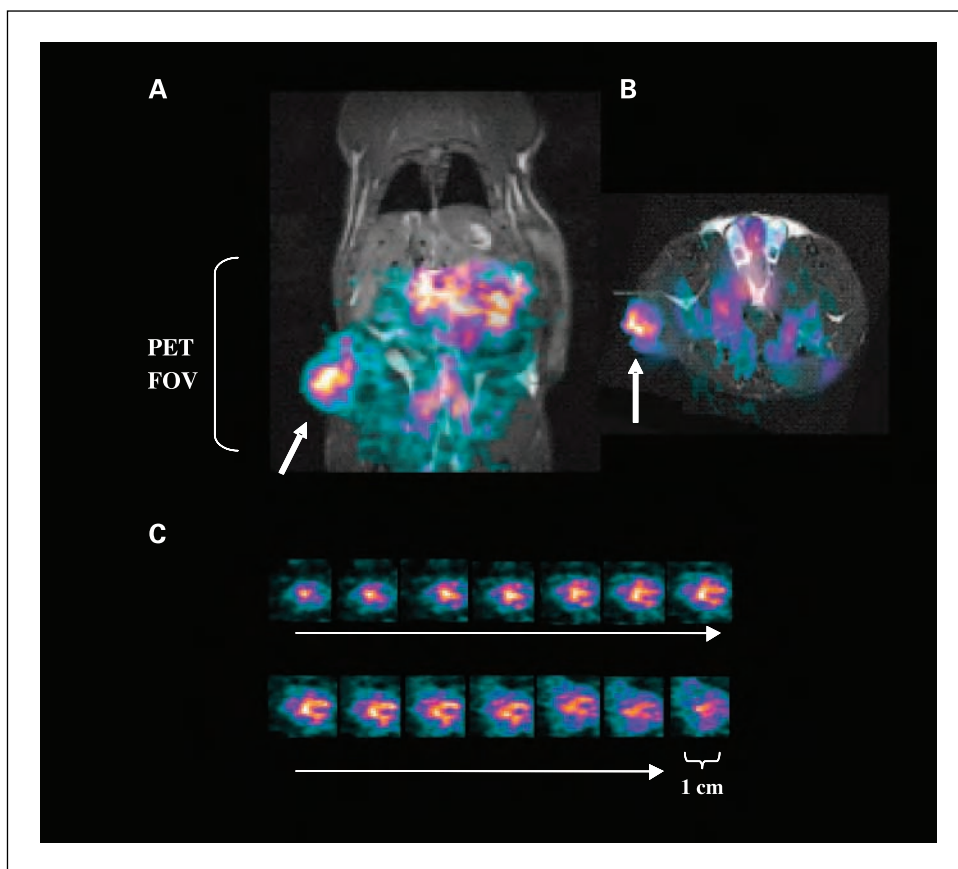
Jennewein and Rösch have developed efficient methods for isolating arsenic from irradiated germanium oxide targets to provide arsenic in a form that is useful for labeling sensitive biomolecules (7, 8). They have also developed novel methods for linking arsenic to biomolecules. Here, we show that monoclonal antibodies can be labeled efficiently with  $^{74}\text{As}$  or  $^{77}\text{As}$  to produce radioimmunoconjugates having full antigen-binding activity and high *in vitro* and *in vivo* stability. [ $^{74}\text{As}$ ]bavituximab was stable for several days when incubated in serum. Very little nonspecific uptake of radioactivity by the liver was seen in rats injected with [ $^{74}\text{As}$ ]bavituximab or [ $^{74}\text{As}$ ]rituximab, indicating that the labeled antibodies have high *in vivo* stability and that transfer of  $^{74}\text{As}$  to serum proteins and uptake by the liver is minimal. This contrasts with the use of radioiodine for antibody labeling, where dehalogenation and high thyroid uptake are considerable. Instability is less of a problem for antibodies labeled with metal ions (e.g.,  $^{64}\text{Cu}$ ) since the advent of improved chelating agents.

Biodistribution studies showed high selectivity of bavituximab toward tumor tissue. Within 48 h, the tumor to muscle ratio approached 10 and reached almost 500 by 72 h (Fig. 2).

The tumor to liver ratio exceeded 20 by 72 h. [ $^{74}\text{As}$ ]bavituximab showed 30-fold to 50-fold higher absolute uptake in tumor than did the control antibody [ $^{74}\text{As}$ ]rituximab. The *ex vivo* biodistribution matches the tumor uptake observed by imaging, with higher localization of bavituximab being seen in the tumor than in any normal tissues. Both  $^{74}\text{As}$ -labeled bavituximab and rituximab accumulated in the spleen, possibly due to nonspecific capture of immunoglobulin or metabolites by the reticuloendothelial system. We did not observe preferential accumulation of [ $^{74}\text{As}$ ]bavituximab in the liver or spleen, which would be expected if bavituximab bound to phosphatidylserine-expressing blood cells being cleared by these organs.

The PET and planar scintigraphy studies showed pronounced localization of bavituximab to solid Dunning prostate R3227-AT1 tumors. Localization was seen in the periphery of the tumor and in various central regions, in agreement with prior PET studies with FDG or perfusion MRI (32–34). We have previously observed that phosphatidylserine-positive vessels are present in both the periphery and the core of tumors. It is likely that the peripheral location of the radioactivity seen with [ $^{74}\text{As}$ ]bavituximab in the present study is because this is the region of tumors that typically has the most abundant and functional blood supply. Some of the bavituximab was probably free in the blood of peripheral vessels or had diffused into peripheral tumor regions because a similar peripheral distribution was seen with the nonbinding rituximab control antibody. Heterogeneous localization of bavituximab was also observed throughout the central regions of the tumor. This central localization was antigen-specific because relatively little

**Fig. 5.** Small animal PET. *A* and *B*, small animal PET images obtained from a Dunning prostate R3227-AT1 tumor-bearing rat 48 h after injection of 10 MBq of [ $^{74}\text{As}$ ]bavituximab coronal (*A*) and transaxial (*B*). PET intensity is overlaid on slices obtained by three-dimensional MRI. [ $^{74}\text{As}$ ]bavituximab localized to the tumor (*arrows*) and was also visible in the blood pool of normal organs. The PET field of view (*FOV*) is indicated by the bracket. *C*, images of 1-mm sequential tumor slices from the three-dimensional data sets.



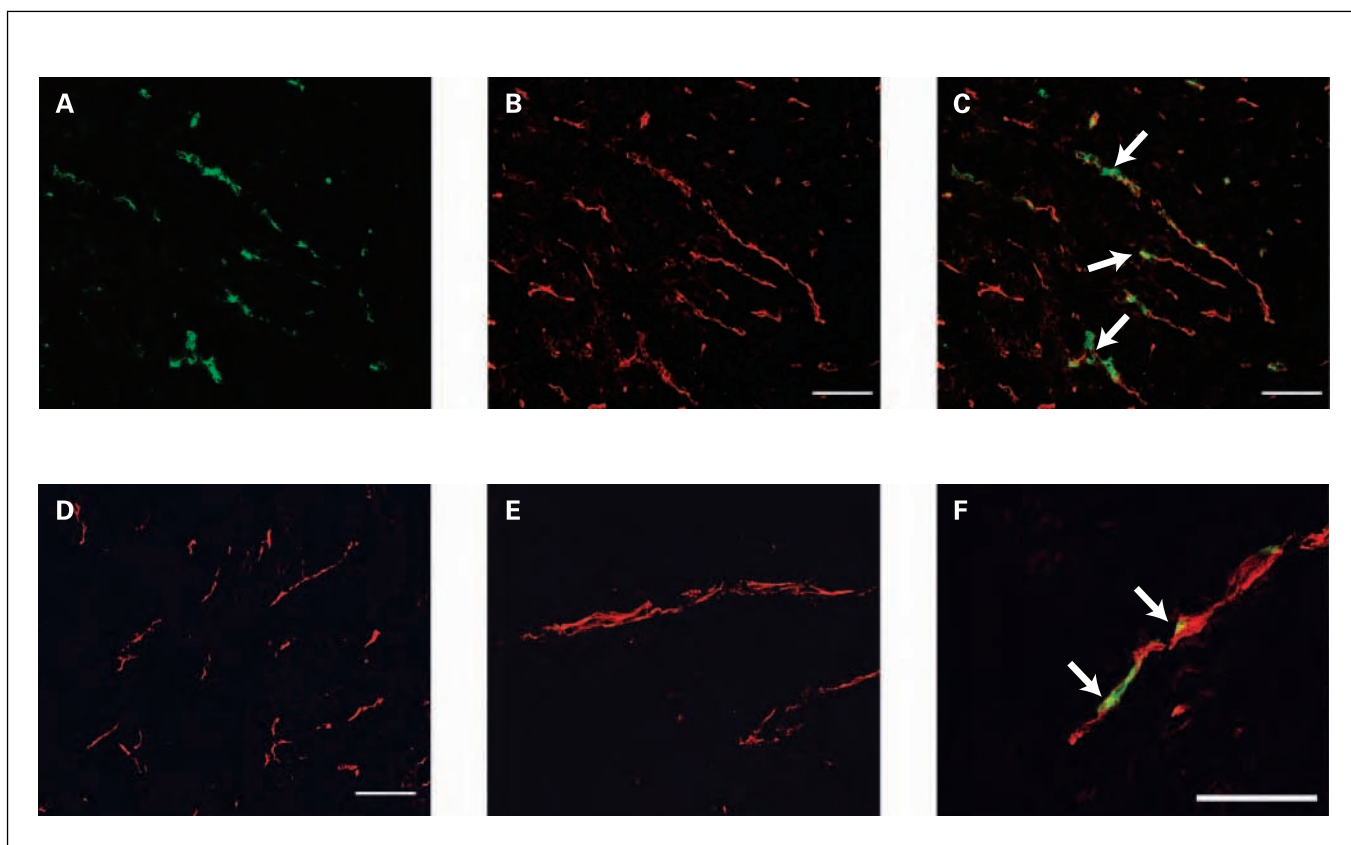


**Fig. 6.** Localization of bavituximab to tumor vessels after injection into rats bearing syngeneic Dunning R3227-AT1 prostate tumors. Rats were injected i.v. with bavituximab or rituximab. After 24 h, the rats were exsanguinated and their tumors were removed. *A-C* show blood vessels in a frozen section of tumor at low magnification. *A*, stained with biotinylated goat anti-human IgG followed by Cy2-streptavidin (green) to detect localized bavituximab; *B*, stained with mouse anti-rat CD31 followed by Cy3-labeled goat anti-mouse IgG (red) to detect vascular endothelium; *C*, a merged image of bavituximab localized on CD31-positive endothelium (thick). *D*, a merged image of blood vessels in the tumor of a rat injected with rituximab. No binding of rituximab was detected. *E-F*, higher magnification merged images of blood vessels in tumors from rats injected with rituximab (*E*) or bavituximab (*F*). Bars, 100  $\mu$ m.

localization was seen in central tumor regions with the rituximab control antibody. Immunohistochemical examination confirmed that the bavituximab was bound to the endothelium of the central tumor regions with little staining of necrotic regions being visible. The heterogeneous staining with bavituximab is probably because some tumor regions have more hypoxia, acidity, or inflammatory cytokines than others, leading to variable levels of phosphatidylserine exposure on the tumor endothelium. We have previously examined multiple different types of mouse and human tumors growing in mice, and all have phosphatidylserine-expressing tumor vascular endothelium (10, 14, 35, 36). The percentage of phosphatidylserine-positive vessels ranged from 16% to 41%. Thus, we anticipate that vascular imaging observed with bavituximab in the present studies will extend to other tumor types. The Dunning prostate R3227-AT1 tumor has small areas of focal necrosis scattered throughout the tumor (37). The lack of strong localization of bavituximab to these necrotic regions could be related to difficulties of access associated with high interstitial pressure and inadequate lymphatic drainage. However, in a previous study using a different anti-phosphatidylserine antibody (9D2) and different tumors, staining of necrotic tumor tissue was observed in addition to the endothelium at later time points (10). The apparent difference in the ability of the two antibodies to localize to necrotic regions may relate

to idiosyncrasies of the tumor models or to differences in the ability of the two antibodies to resist proteolysis after binding. It is also possible that the cofactor protein  $\beta$ 2-glycoprotein I, which is needed for phosphatidylserine binding by bavituximab but not 9D2, does not efficiently penetrate into extravascular tissues or is degraded rapidly by proteolytic enzymes within the tumor interstitium.

The present labeling chemistry can also be applied to other radioarsenic isotopes.  $^{72}\text{As}$  has a half life of 26 h, suitable for imaging with antibody Fab' and F(ab')<sub>2</sub> fragments and other biomolecules having intermediate half lives. The abundance of positrons for  $^{72}\text{As}$  is 88%, which is higher than in other commonly used positron emitters, such as  $^{64}\text{Cu}$  (18.0%  $\beta^+$ ,  $T_{1/2}$  12.7 h) or  $^{124}\text{I}$  (23.0%  $\beta^+$ ,  $T_{1/2}$  4.2 days). Arsenic provides two potentially therapeutic isotopes:  $^{77}\text{As}$  ( $T_{1/2}$  38.8 h,  $\bar{E}_{\beta}$  226 keV), as used in the present study, and  $^{76}\text{As}$  ( $T_{1/2}$  26.3 h,  $\bar{E}_{\beta}$  1.068 keV; see Supplementary Table S1). The multiple isotopes of arsenic potentially offer additional applications, such as combined imaging/dosimetry and radioimmunotherapy. Another advantage of arsenic is that, unlike iodine, it does not subject the thyroid to high irradiation. The doses of arsenic used for imaging with [ $^{74}\text{As}$ ]bavituximab are also several orders of magnitude below toxic levels, so that even if  $^{74}\text{As}$  were released from the antibody, no toxicity would be expected. However, the arsenic isotopes do not include  $\alpha$  emitters, which,

because of their short path length, could be advantageous for vascular targeted therapies.

In conclusion, we have exploited the unique properties of arsenic radioisotopes to achieve clear imaging of tumors with

an antibody, bavituximab, directed against a tumor vessel marker. Radioarsenic-labeled bavituximab shows promise as a vascular imaging agent for tumor detection and dosimetry in man.

## References

- Rudin M, Weissleder R. Molecular imaging in drug discovery and development. *Nat Rev Drug Discov* 2003;2:123–31.
- Massoud TF, Gambhir SS. Molecular imaging in living subjects: seeing fundamental biological processes in a new light. *Genes Dev* 2003;17:545–80.
- Kumar R, Jana S. Positron emission tomography: an advanced nuclear medicine imaging technique from research to clinical practice. *Methods Enzymol* 2004;385:3–19.
- McQuade P, Rowland DJ, Lewis JS, Welch MJ. Positron-emitting isotopes produced on biomedical cyclotrons. *Curr Med Chem* 2005;12:807–18.
- Boerman OC, Kopp MJ, Postema EJ, Corstens FH, Oyen WJ. Radionuclide therapy of cancer with radio-labeled antibodies. *Curr Med Chem Anti-Canc Agents* 2007;7:335–43.
- Burnham CA, Aronow S, Brownell GL. A hybrid positron scanner. *Phys Med Biol* 1970;15:517–28.
- Jennewein M, Qaim SM, Hermanne A, et al. A new method for the radiochemical separation of arsenic from reactor and cyclotron irradiated germanium oxide. *Appl Rad Isoto* 2005;63:343–51.
- Jennewein M, Schmidt A, Novgorodov AF, Qaim SM, Roesch F. A no-carrier-added  $^{72}\text{Se}/^{72}\text{As}$  radionuclide generator based on distillation. *Radiochim Acta* 2004;92:245–9.
- Huang X, Bennett M, Thorpe PE. A monoclonal antibody that binds anionic phospholipids on tumor blood vessels enhances the antitumor effect of docetaxel on human breast tumors in mice. *Cancer Res* 2005;65:4408–16.
- Ran S, Downes A, Thorpe PE. Increased exposure of anionic phospholipids on the surface of tumor blood vessels. *Cancer Res* 2002;62:6132–40.
- Ran S, Thorpe PE. Phosphatidylserine is a marker of tumor vasculature and a potential target for cancer imaging and therapy. *Int J Radiat Oncol Biol Phys* 2002;54:1479–84.
- Luster TA, He J, Huang X, et al. Plasma protein  $\beta$ -2-glycoprotein 1 mediates interaction between the anti-tumor monoclonal antibody 3G4 and anionic phospholipids on endothelial cells. *J Biol Chem* 2006;281:29863–71.
- Ran S, Gao B, Duffy S, Watkins L, Rote N, Thorpe PE. Infarction of solid Hodgkin's tumors in mice by antibody-directed targeting of tissue factor to tumor vasculature. *Cancer Res* 1998;58:4646–53.
- Ran S, He J, Huang X, Soares M, Scothorn D, Thorpe PE. Anti-tumor effects of a monoclonal antibody directed against anionic phospholipids on the surface of tumor blood vessels in mice. *Clin Cancer Res* 2005;11:1551–62.
- Seigneuret M, Devaux PF. ATP-dependent asymmetric distribution of spin-labeled phospholipids in the erythrocyte membrane: relation to shape changes. *Proc Natl Acad Sci U S A* 1984;81:3751–5.
- Bombeli T, Karsan A, Tait JF, Harlan JM. Apoptotic vascular endothelial cells become procoagulant. *Blood* 1997;89:2429–42.
- Boyle EM, Jr., Pohlman TH, Cornejo CJ, Verrier ED. Endothelial cell injury in cardiovascular surgery: ischemia-reperfusion. *Ann Thorac Surg* 1996;62:1868–75.
- Bevers EM, Comfurios P, Zwaal RF. Changes in membrane phospholipid distribution during platelet activation. *Biochim Biophys Acta* 1983;736:57–66.
- Rote NS, Ng AK, Dostal-Johnson DA, Nicholson SL, Siekman R. Immunologic detection of phosphatidylserine externalization during thrombin-induced platelet activation. *Clin Immunol Immunopathol* 1993;66:193–200.
- Bitbol M, Fellmann P, Zachowski A, Devaux PF. Ion regulation of phosphatidylserine and phosphatidylethanolamine outside-inside translocation in human erythrocytes. *Biochim Biophys Acta* 1987;904:268–82.
- Zhao J, Zhou Q, Wiedmer T, Sims PJ. Level of expression of phospholipid scramblase regulates induced movement of phosphatidylserine to the cell surface. *J Biol Chem* 1998;273:6603–6.
- Hamon Y, Broccardo C, Chambenoit O, et al. ABC1 promotes engulfment of apoptotic cells and transbilayer redistribution of phosphatidylserine. *Nat Cell Biol* 2000;2:399–406.
- Pradhan D, Williamson P, Schlegel RA. Phosphatidylserine vesicles inhibit phagocytosis of erythrocytes with a symmetric transbilayer distribution of phospholipids. *Mol Membr Biol* 1994;11:181–7.
- Balasubramanian K, Schroit AJ. Aminophospholipid asymmetry: a matter of life and death. *Annu Rev Physiol* 2003;65:701–34.
- Duncan RJ, Weston PD, Wrigglesworth R. A new reagent which may be used to introduce sulfhydryl groups into proteins, and its use in the preparation of conjugates for immunoassay. *Anal Biochem* 1983;132:68–73.
- Henke K, Hartmann GH, Peschke P, Hahn EW. Stereotactic radiosurgery of the rat Dunning R3327-1 prostate tumor. *Int J Radiat Oncol Biol Phys* 1996;36:385–91.
- Zhao D, Ran S, Constantinescu A, Hahn EW, Mason RP. Tumor oxygen dynamics: correlation of *in vivo* MRI with histological findings. *Neoplasia* 2003;5:308–18.
- Modestou M, Puig-Antich V, Korgaonkar C, Eapen A, Quelle DE. The alternative reading frame tumor suppressor inhibits growth through p21-dependent and p21-independent pathways. *Cancer Res* 2001;61:3145–50.
- Tsyganov EN, Anderson J, Arbiq G, et al. UTSM small animal positron emission imager. *IEEE Trans Nucl Inst* 2006;53:2591–600.
- Bischof Delaloye A, Delaloye B. Tumor imaging with monoclonal antibodies. *Semin Nucl Med* 1995;25:144–64.
- Von Kleist S. Ten years of tumor imaging with labeled antibodies. *In vivo* 1993;7:581–4.
- Karam JA, Mason RP, Koeneman KS, Antich PP, Benaim EA, Hsieh JT. Molecular imaging in prostate cancer. *J Cell Biochem* 2003;90:473–83.
- Jiang L, Zhao D, Constantinescu A, Mason RP. Comparison of BOLD contrast and Gd-DTPA dynamic contrast enhanced imaging in rat prostate tumor. *Magn Reson Med* 2004;51:953–60.
- Zhao D, Jiang L, Hahn EW, Mason RP. Continuous low-dose (Metronomic) chemotherapy on rat prostate tumors evaluated using MRI *in vivo* and comparison with histology. *Neoplasia* 2005;7:678–87.
- Beck AW, Luster TA, Miller AF, et al. Combination of a monoclonal anti-phosphatidylserine antibody with gemcitabine strongly inhibits the growth and metastasis of orthotopic pancreatic tumors. *Int J Cancer* 2006;118:2639–43.
- He J, Luster TA, Thorpe PE. Radiation-enhanced vascular targeting of human lung cancers in mice with a monoclonal antibody that binds anionic phospholipids. *Clin Cancer Res* 2007;207:5211–8.
- Hahn EW, Peschke P, Mason RP, Babcock EE, Antich PP. Isolated tumor growth in a surgically formed skin pedicle in the rat: a new tumor model for NMR studies. *Magn Reson Imaging* 1993;11:1007–17.